MECHANISMS OF IONIZING RADIATION RESPONSE IN SILICON PIEZORESISTIVE MICROMACHINED CANTILEVERS

by

Charles Nathan Arutt

Dissertation

Submitted to the Faculty of the

Graduate School of Vanderbilt University

in partial fulfillment of the requirements

for the degree of

DOCTOR OF PHILOSOPHY

in

Electrical Engineering

June 30, 2018

Nashville, Tennessee

Approved:

Ronald D. Schrimpf, Ph.D.

Michael L. Alles, Ph.D.

Jim L. Davidson, Ph.D.

Daniel M. Fleetwood, Ph.D.

Robert A. Reed, Ph.D.

Bridget R. Rogers, Ph.D.

To my parents, Paul and Karen

ACKNOWLEDGEMENTS

I would like to thank all of the people who made this research possible. Thank you to my advisor and committee chair Prof. Ronald Schrimpf for his guidance during both my undergraduate and graduate careers. Your support and encouragement from conversations ranging from music to radiation effects have been invaluable. Thank you to my committee, Prof. Michael Alles, Prof. Jim Davidson, Prof. Daniel Fleetwood, Prof. Robert Reed, and Prof. Bridget R. Rogers. Thank you to Prof. Robert Weller for all of the stimulating conversations we've had.

Thank you to the University of Louisville for providing the devices used in this work. Support and lively conversations about MEMS from Prof. Bruce Alphenaar, Prof. Shamus McNamara, Prof. Kevin Walsh, Ji-Tzouh Lin, and Pranoy Deb Shuvra have been illuminating and helpful. The foundation of work done by Huiqi Gong and Wenjun Liao was very beneficial. I would also like to acknowledge the Defense Threat Reduction Agency for their funding of this work through Grant HDTRA1-15-1-0027.

Thank you to Alan Tipton and Michael King for your mentorship. For all of your help and time you spent listening to me talk about my work, your friendship, and your support, thank you to Isaak Samsel, Jeff Maharrey, Rachel Harrington, James Trippe, Zac Diggins, Rebekah Austin, Francis Afzal and Kaitlyn Ryder. Thank you to all of the students, faculty, and staff in the Radiation Effects and Reliability group.

Thank you for my parents, Paul and Karen, for their guidance, love, and support throughout my entire education. I would not be where I am today without you. Thank you to my wife, Alexandria for all of your support throughout my journey.

TABLE OF CONTENTS

Page

LIST OF TABLES

LIST OF FIGURES

CHAPTER I

INTRODUCTION

Microelectromechanical systems (MEMS) are attractive for implementing key functions in electromechanical applications such as logic, sensing, actuation, and potentially oscillators in both earth and space applications due to reductions in size, weight, and power [1, 2]. MEMS have been used in a variety of applications including logic [3], global positioning systems [4], accelerometers [5], chemical, environmental, and biological sensors [6], pressure sensors [7], and atomic force microscopy [8].

MEMS logic has been of particular interest due to the possibility of having high isolation, minimal leakage current, and high resistance when a device is in its "off" or "0" state [9]. Beyond being a simple switch, MEMS can be designed to perform Boolean algebra functions like AND, OR, XOR, NAND, etc. or be one-time-programmable memory [3, 10, 11]. These devices operate with turn-on voltages ranging up to 1.5 V.

Even with recent advances, the reliability of MEMS is lagging compared to traditional CMOS circuits [11]. For example, a common issue with MEMS based logic is stiction. When a device is in an on-state, two parts must physically touch to make an electrical connection. After a relatively low number of cycles (~10^6), the physical devices can stick together to create a permanent short circuit. Alternatively, if the external force actuating the devices is too great, the two pieces can be fused together to create a short circuit. Solutions and improvements of these failure mechanisms are a focus of continuing research [11].

Stiction has been leveraged to design non-volatile memory with both silicon and silicon carbide. Soon *et al.* designed a device fabricated with traditional CMOS techniques that uses van der Waals

force to create a permanent connection. The device is fabricated in an open position and connects to one of two terminals, similar to a relay. When multiple devices are fabricated together, a variety of logic circuits can be created [12]. He *et al.* used SiC to create MEMS anti-fuse devices as part of a one-time-programmable memory. A cantilever is anchored to a source electrode and suspended over a gate. Once programmed with a gate voltage, the cantilever is permanently attached to a drain contact on the other side of the gate [3].

The promise of minimal leakage current is highly attractive for use in harsh environments, like space, and a motivating factor to research the effects of radiation on MEMS logic. While devices like these show great potential in radiation environments for applications like non-volatile memories, their static nature limits their use as a test vehicle for researching basic material properties. Measuring changes in Young's modulus is difficult for a device which only has two states compared with a resonator where changes in resonance frequency depend on Young's modulus as a function of total dose. Additionally, the mechanical failure mechanisms make direct research on MEMS logic difficult. In order to understand the effects of radiation on MEMS logic, this work uses resonating piezoresistive T-shaped cantilevers to focus on silicon properties that are relevant to MEMS logic such as elasticity and piezoresistivity.

Experimental Devices

This work uses resonating piezoresistive micromachined cantilevers with an asymmetric base to investigate the effects of 10-keV X-rays on the piezoresistive and elastic properties of uniformly doped silicon. A top down view of two T-shaped cantilevers is presented in Figure 1.1 with dimensions in Table 1.1, after [13]. A cantilever beam is attached at one end to the center of a base beam and free at the other. The base beam is anchored to the substrate by an electrode at each end

and is asymmetric such that the left side is wider than the right. When no force is applied to the free end of the cantilever, it is at rest in the center as in the solid outline in Figure 1.1. When an external force is applied to the free end, the beam deflects in the direction of the force as in the dotted outlines in Figure 1.1 [13].

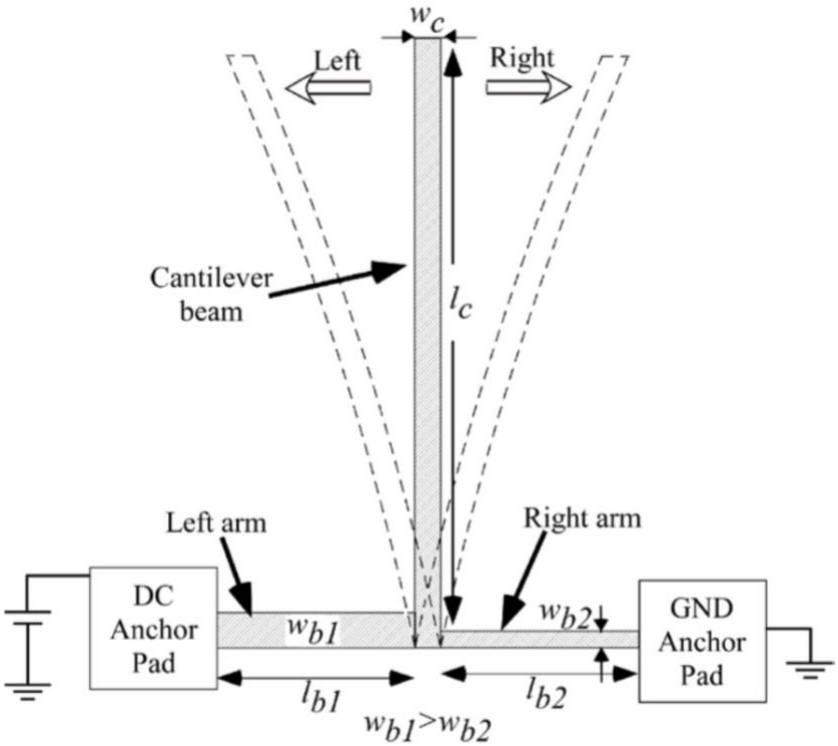

Figure 1.1: A MEMS cantilever with an asymmetric base beam with labels for dimensions shown in Table 1.1. Anchor pads show how voltage is applied, after [13].

Table 1.1: Silicon Cantilever Dimensions, after [13]

Parameter	Symbol	Value (μm)
Cantilever length	l_c	655
Cantilever width	w_c	8
Left arm width	w_{b1}	11
Right arm width	w_{b2}	5
Left arm length	l_{b1}	51
Right arm length	l_{b2}	51

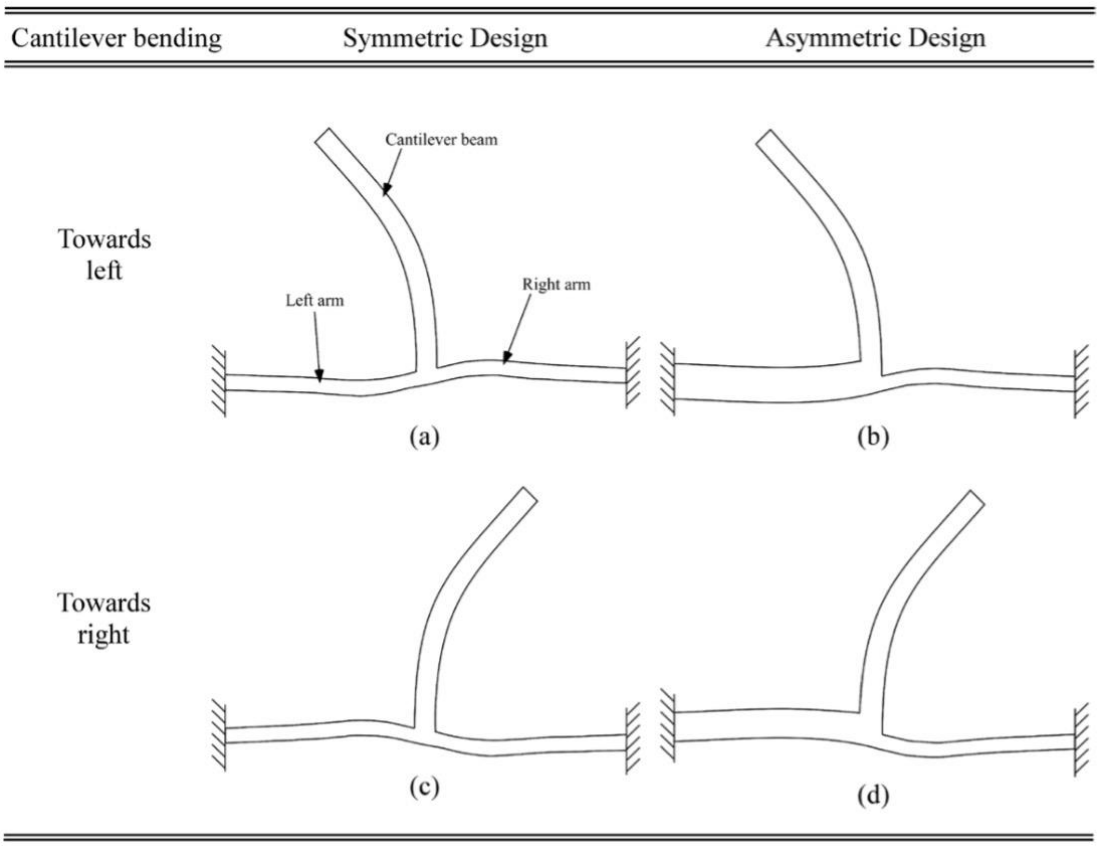

Figure 1.2: A schematic illustration of (a and c) symmetric and (b and d) asymmetric base beam bending when the cantilever bends to the left and right, after [13].

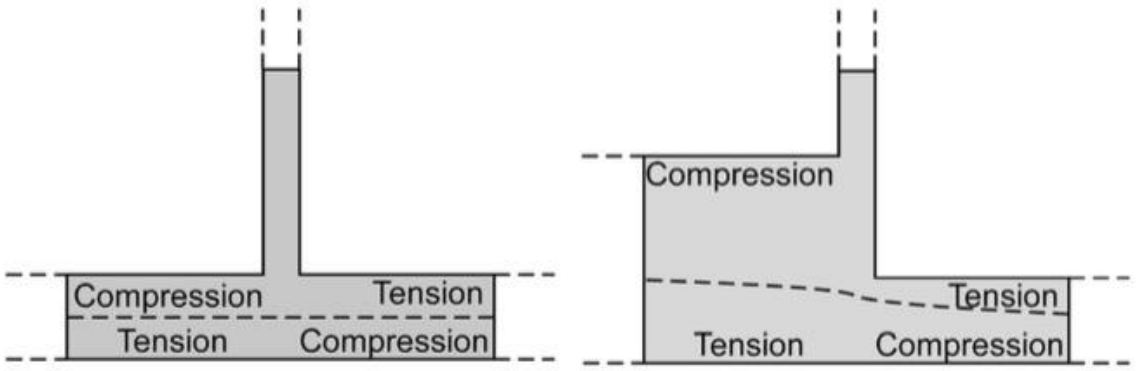

(a) (b)

Figure 1.3: A schematic illustration of the neutral axis (dotted line) dividing areas in compression and tension in (a) symmetric and (b) asymmetric base beams, after [13].

When the cantilever beam is loaded, the base beam also bends. Figure 1.2 demonstrates how both symmetric and asymmetric base beams bend when the cantilever is deflected to the left and right. When the base beam bends, the different sections are under either compression or tension, causing changes in resistivity. The changes in resistivity are opposite for compression and tension and depend on dopant type [14]. Figure 1.3 shows the neutral axis dividing the portions of the anchor beam in tension or compression when the cantilever is deflected to the left in both (a) symmetric and (b) asymmetric base beams. With a symmetric base, the net resistance change is close to zero and difficult to detect because the resistance change on either side is the same. An asymmetric base creates an increase in the net resistance change when the beam is deflected because a larger portion is in compression than in tension or vice versa. With an asymmetric base, the wider side of the base has greater stiffness and is displaced less than the narrow side when the beam is deflected. Shuvra, *et al.* optimized the geometry to achieve a 481x increase in sensitivity to the net resistance change with an asymmetric base [13].

To actuate the device, an AC voltage is applied at the free end of the cantilever to one of the two gate electrodes while the other end is grounded and causes the cantilever to oscillate. The voltage applied to the gate electrode induces an electric field that acts as an external force, displacing the free end of the cantilever. A DC voltage applied across the two anchored electrodes allows the resistance to be monitored. Figure 1.4(a) shows the orientation of the cantilever on a wafer and to its associated electrodes. Figure 1.4(b) depicts the material stack of the devices including the thickness of each layer. Figure 1.4(c) is a scanning electron microscope (SEM) image of a sample device. Figure 1.4(d) demonstrates the cantilever orientation with respect to the wafer indicating that the cantilever bends in the [1 1 0] direction to take advantage of the piezoresistive sensitivity in that direction [13, 15].

The devices are fabricated at the University of Louisville Micro/Nano Technology Center. A flowchart of the major fabrication steps is in Figure 1.5. Aluminum or gold is deposited and patterned using optical lithography to form the contacts. Dry reactive-ion etching (DRIE) is done on the top side to define the cantilever, removing all the silicon except for the devices. DRIE is also done through the backside to create the cavity under the device all the way to the buried oxide layer. Finally, a dry etch is used from the backside to release the cantilever [13].

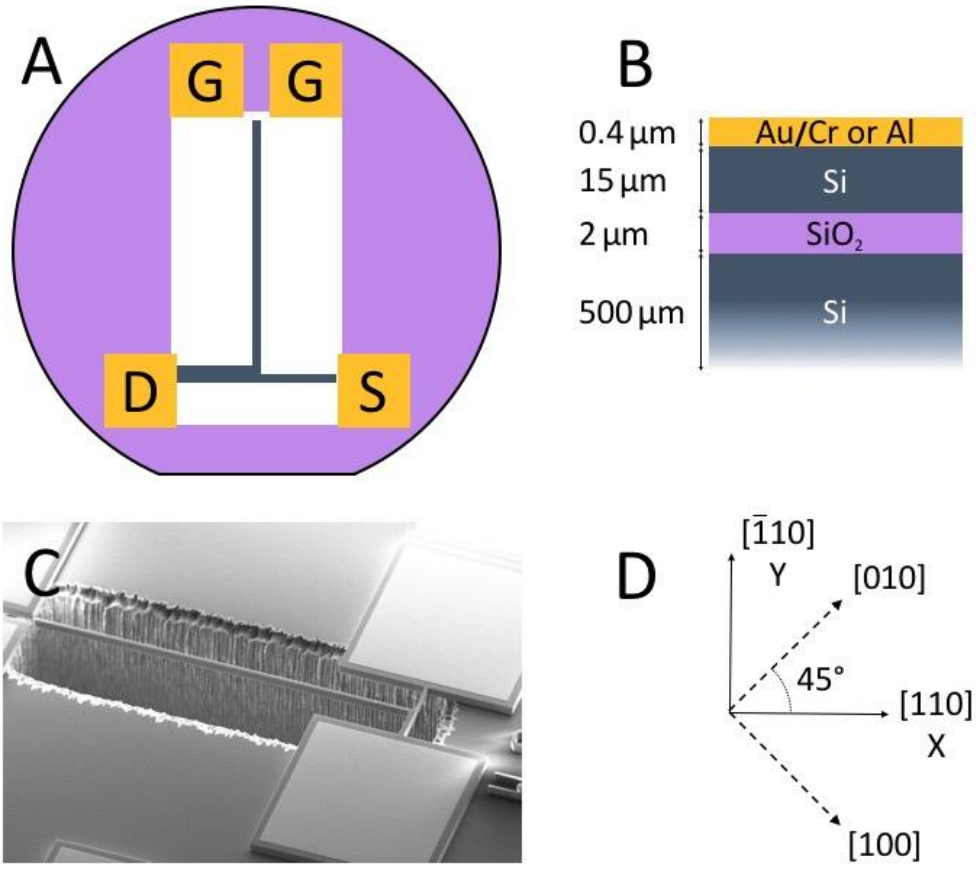

Figure 1.4: Device structure: (a) top view of cantilever with electrodes; (b) cross-sectional view of materials with measurements; (c) SEM image of the cantilever; and (d) cantilever orientation with respect to wafer orientations. The beam bends in the [1 1 0] direction, after [42].

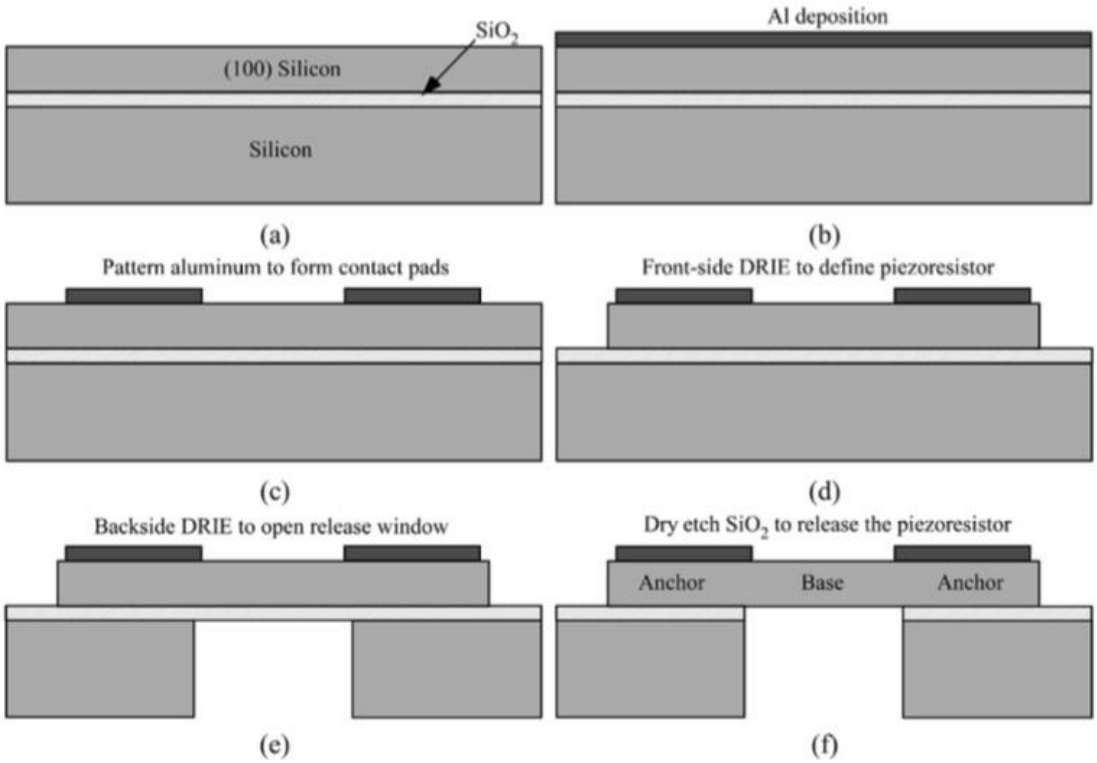

Figure 1.5: A flowchart depicting the main steps in the fabrication process of the cantilevers and resistors used in these experiments, after [13].

Introduction to Piezoresistivity and Elasticity

Piezoresistivity originates from increases and decreases in resistivity due to tensile and compressive stress changing the dimensions of the material [14, 15]. Strain shifts energy levels without changing other electrical properties of the material [16]. This affects the mobility of carriers and changes the resistivity. The greater the deformation in the material, the higher the resistivity change is. When the cantilever is driven at its resonance frequency, the beam deflection increases and causes greater displacement in the base. Therefore, the highest net resistance is at the resonance frequency.

The amount of deflection that can occur in the cantilever depends on the elasticity of the silicon, or the amount the silicon can be non-permanently deformed. For an isotropic, homogenous material, the relationship between stress (σ) and strain (ε) is defined by Hooke's Law:

$$\sigma = C\varepsilon \tag{1.1}$$

where *C* is a fourth-order tensor that describes elasticity and is a property of a material. *C* can be represented a constant value of tensile elasticity, Young's modulus (*Y*) [17]. Stress and strain are each represented by a 3 × 3 matrix in a Cartesian coordinate system where the linear mapping of the two tensors leads to the 81 value fourth-order tensor that describes elasticity. Silicon's cubic symmetry, however, allows this to be condensed to three independent components: longitudinal (c_{11}), transverse (c_{12}), and shear elasticity (c_{44}) [14, 18, 19, 20]. Traditionally, these have been split into three "principal elasticities" by Lord Kelvin [20, 21]: bulk modulus,

$$\kappa = \frac{(c_{11}+2c_{12})}{3} \tag{1.2}$$

and two shear moduli, rectangular and diagonal,

$$\mu' = \frac{(c_{11}-c_{12})}{2} \tag{1.3}$$

$$u'' = c_{44}\ . \tag{1.4}$$

The combining of two second-rank tensors gives four subscripts which are combined using collapsed notation [22]. The first subscript denotes the direction of strain while the second subscript denotes the direction of the stress [14].

In silicon, elasticity is directionally dependent because it is anisotropic. The value of Young's modulus is different for each of the ⟨1 0 0⟩, ⟨1 1 0⟩, and ⟨1 1 1⟩ directions [19]. The devices used in this work have force applied in the [1 1 0] direction, allowing Young's modulus to be simplified to [23]:

$$Y_{110} = \frac{4(c_{11}+2c_{12})(c_{11}-c_{12})c_{44}}{2c_{11}c_{44}+(c_{11}+2c_{12})(c_{11}-c_{12})}. \quad (1.5)$$

Young's modulus in the ⟨1 1 0⟩ directions has been measured to be 169 GPa for Si [19, 24]. Given the orientation of the silicon devices used in these experiments, the elastic components of interest are shear elasticities, (1.3) and (1.4) [13, 25, 26]. The value of the resonance frequency depends on Young's modulus. For cantilevers, the resonance frequency is calculated via:

$$f_n = \frac{\beta_n^2}{2\pi L^2}\sqrt{\frac{YI}{\rho hb}} \quad (1.6)$$

where β_n is an eigenvalue associated with the resonance mode of a singly attached cantilever (β_0 = 1.875, in this case), L is the length of the cantilever, b is beam thickness, h is beam height, ρ is beam mass density, and I is the cross-sectional moment of inertia ($hb^3/12$) [27].

Radiation Effects in Silicon MEMS

While there has been considerable research focused on developing MEMS for sensors, actuators, logic, oscillators, and other applications, only limited results have been reported that focus on the effects of radiation on these functions. Furthermore, studies of radiation on MEMS have focused on finding device tolerance over understanding the mechanisms causing failure [2, 28]. When failure mechanisms are considered, the focus is typically placed on traditional radiation effects mechanisms like dielectric charging from total ionizing dose or carrier removal from displacement damage [29, 30, 31]. Research where the primary focus is the change in silicon material properties, such as elasticity, is lacking [32].

In 2011, H. R. Shea complied a review paper gathering/collecting/composing published results of radiation effects testing on MEMS [2]. A large range of radiation tolerances have been reported for devices exposed to γ-rays from failure at total doses of 4 krad(Si) [33] to survival after 30

Mrad(SiO_2) [34]. Low dose-rate experiments do not show any change in experimental results compared to high dose rates [33]. Failures at low total doses are typically not due to any mechanisms in the MEMS devices itself, but the failure of supporting CMOS circuitry [33, 35]. Radiation hardness in electrostatic MEMS devices often is limited by dielectric charging in the devices, but shows very strong geometric and bias dependencies [36, 37].

Piezoresistive MEMS accelerometers and pressure sensors exposed to γ-rays exhibit high radiation tolerance [34, 38, 39]. Accelerometers failed after exposure to 20 Mrad(SiO_2) due to trapped charge in the oxides inducing an electric field across the piezoresistor. The voltage output in response to acceleration increased, corresponding to a 4-12% increase in piezoresistive sensitivity after irradiation. Holbert *et al.* proposed that positive trapped charge in the ~50 nm native oxide and the Si/SiO_2 interface induces a depletion region that limits the current flow through the piezoresistor. Increasing device thickness mitigates the effect because the induced depletion region becomes insignificant compared to the device size. Holbert *et al.* also predicted *n*-type piezoresistors would show less sensitivity to radiation [34]. More recent results on piezoresistive pressure sensors showed decreased piezoresistive sensitivity with dose. Pressure sensors showed no change after exposure to γ-rays to 10 Mrad(SiO_2), but showed an 80% drop in output voltage after exposure to 31 Mrad(SiO_2) [39].

Research on the effects of displacement damage on MEMS has been the only work to focus on the effects of radiation on Young's modulus. Gomes and Shea reported Young's modulus increased 0.05% due to low energy protons [31]. Previous work focusing on the devices used in this work found Young's modulus and resonance frequency to increase due to displacement damage. Cantilevers were irradiated with protons, which cause both TID and displacement damage. When the cantilevers were irradiated with 0.8-MeV protons, displacement damage

dominated the response causing the resonance frequency to increase due to carrier removal. When the cantilevers were irradiated with 2-MeV protons, the contributions from TID dominated the resonance response, causing a decrease in resonance frequency due to dopant depassivation [30].

A test of MEMS logic shows the AND and XOR gates discussed above screened devices by exposing them to a nuclear reactor for 120 minutes at 90 kW. After irradiation, the off-state current was still close to zero. The threshold voltage shifted by 2 V after 60 minutes exposure, but was shown to be -2 V lower than pre-rad measurements after 120 minutes of exposure. It is unclear if the shifts in threshold voltage are due to continuous use of the device or are a result of exposure to radiation. A MOSFET tested in the same environment for "a few minutes" showed an order of magnitude increase in drain-source current [11].

As MEMS designs continue into the nanoscale regime and get thinner, the value of Young's modulus decreases [19, 40]. For example, the Young's moduli of cantilevers fabricated with widths from 50 – 1000 nm were measured using electrostatic pull-in stability. Devices with 50 nm cantilever width were measured to have a Young's modulus of ~80 Gpa, which was 54% lower than the devices with 1000 nm cantilever widths that had a measured Young's modulus of 169 GPa [40]. In general, decreases in Young's modulus are only seen for devices with a width less than 100 nm [40, 41]. As nanoelectromechanical systems (NEMS) continue to be more common, this could bring a greater sensitivity to radiation effects.

Summary of this Work

In this work, the total-ionizing-dose (TID) response is evaluated for T-shaped asymmetric piezoresistive micromachined cantilevers as a function of dose rate, dopant concentration, dopant type, and hydrogen contents. Understanding dose-rate effects in MEMS is crucial as these types

of devices are considered for space applications where ionizing dose rates are much lower than those typically used for ground testing (including this work). The effects of dopant concentration and type are useful for providing insights on the mechanisms causing resonance frequency shifts. Additionally, these data points are beneficial for hardness assurance when designing a device for space applications. Hydrogen content is important in determining the nature of the effects on resonance frequency and resistivity.

Chapter 2 discusses the background of silicon material properties including mobility, piezoresistivity, elasticity, and hydrogen in silicon. A brief discussion of radiation effects is included. Chapter 3 presents the experimental setup and results. Two sets of experiments were conducted to measure changes in resonance frequency and resistivity as a function of total ionizing dose (TID) from 10-keV X-rays. Negative resonance frequency shifts are found to depend significantly on the dose-rate, with greater negative shifts at lower dose rates. Further tests with hydrogenated devices show no measurable differences between hydrogenated and untreated devices for nominal operation, but larger shifts are observed at the lower dose rate for hydrogenated devices in radiation testing. Devices with an order of magnitude less doping show similar shifts as the more highly doped devices at the higher dose rate, but exhibit larger shifts in resonance frequency (like the hydrogenated devices) at the lower dose rate.

The resistors are the base beam of the cantilever measured from the drain to the source and connected in a 4-terminal configuration. The resistivity is calculated based on the known dimensions of the base beam. Exposure to 10-keV X-rays caused resistivity to increase. In all cases, the resistivity had a greater increase at the lower dose rate. The resistivity of the hydrogenated devices increased minimally. Devices with lower dopant concentrations, however,

showed much greater increases in resistivity. *N*-type resistors showed the greatest increase in resistivity as a function of irradiation.

In chapter 4, the data are analyzed and mechanisms are presented to explain the results. The differences in resonance frequency response are attributed to differences in the complex interplay among transport and reactions of hydrogen in silicon, leading to dopant de-passivation as well as differences in rates of surface charging at the higher and lower dose rates [23, 41, 42]. Each of these effects is a potential source of increased carrier densities in the cantilevers. These mechanisms are more significant at the lower dose rate than at the higher dose rates because higher densities of hydrogen in Si favor bimolecular recombination reactions over transport and reactions with dopants that lead to enhanced low-dose-rate response [43]. Space charge effects are more significant at the higher dose rates than the lower rate. Carrier concentration affects Young's modulus and therefore the resonance frequency [17, 26, 44].

The differences in resistivity increases are attributed to decreases in mobility caused by the release of hydrogen and other species due to irradiation. The addition of these species to the sample greatly increases the amount of both ionized and neutral impurity scattering [45]. Differences as a result of dose rate are caused by the same mechanisms that cause the resonance frequency decreases. The greater increase in resistivity for lower doping concentrations is the result of a larger influence of lattice scattering [46].

CHAPTER 2

BACKGROUND

This chapter gives an overview of silicon properties and their applications, atomic mechanisms, and radiation effects. Mobility is discussed first, including the contributions of lattice, ionized impurity, and neutral impurity scattering. The discussion of mobility is continued by focusing on its interactions with strain. The directional nature of constant-energy surfaces and the many-valley theory of semiconductor band structure is presented. This is followed by a brief discussion of the concept of deformation potentials and their calculations and measurements. A discussion on the basics of piezoresistivity and Young's modulus and their directionality follows. An overview of the calculation of the shear elastic constant is presented.

The presence of hydrogen in silicon is then discussed. The presence of positive, neutral, and negative charge states in *n*- and *p*-type silicon, including the atomic reactions and the energies required to bind or dissociate hydrogen-dopant and hydrogen-silicon complexes, are presented. The effects of hydrogen on elasticity are also discussed. Finally, there is a brief section on radiation effects relevant to dose-rate effects and MEMS. An overview of enhanced low dose rate sensitivity (ELDRS) is provided along with a comparison of radiation responses in *n*- and *p*-type silicon based on diodes.

Mobility

Crystalline semiconductors are organized into a periodic lattice. Depending on the direction in a lattice, the available energies and momenta of charge carriers differ. In order to describe the movement of the carriers, one quantity that is frequently used is resistivity:

$$\rho = \frac{1}{qN\mu} \tag{2.1}$$

where q is the charge of an electron, N is the carrier concentration, and μ is mobility. Mobility describes a carrier's ability to move in an electric field [46, 47].

Carrier transport in semiconductors is affected by many different scattering processes in semiconductors [48, 49]. At absolute zero, a perfect lattice does not interact with charge carriers; however, above absolute zero, the lattice vibrates and disrupts its periodicity leading to collisions between carriers and lattice atoms. Impurities in a lattice structure also disturb the periodicity of a lattice. In Si, phonon (lattice) and ionized impurity scattering are the dominant scattering mechanisms [46, 47, 50]. Other types of scattering include neutral impurity, carrier-carrier, and piezoelectric scattering [49].

Figure 2.1 shows a plot of the mobility as a function of total impurity concentration for both phosphorus and boron as calculated by empirical data analyzed by Arora *et al.* [46]. The values shown are valid for a temperature range of 250 – 500 K and for dopant and impurity concentrations up to ~10^{20} cm^{-3} within ±13% of the reported experimental values. They also account for carrier-carrier scattering for dopant densities above 2×10^{16} cm^{-3} [50].

Neutral impurity scattering also affects the mobility of a semiconductor. Typically, its contribution is minimal, but it can have a greater contribution in situations with lower temperatures and when there are large numbers of defects in Si. Norton *et al.* found that approximations for neutral impurity scattering broke down around 300 K and noted that theoretical explanations most likely underestimate the contributions at room temperature and above [52, 53, 55]. The overall mobility of *n*-type silicon as a function of donor concentration and contributions from ionized and neutral impurity scattering are shown at 300 K from Norton's measurements in Figure 2.2 [55].

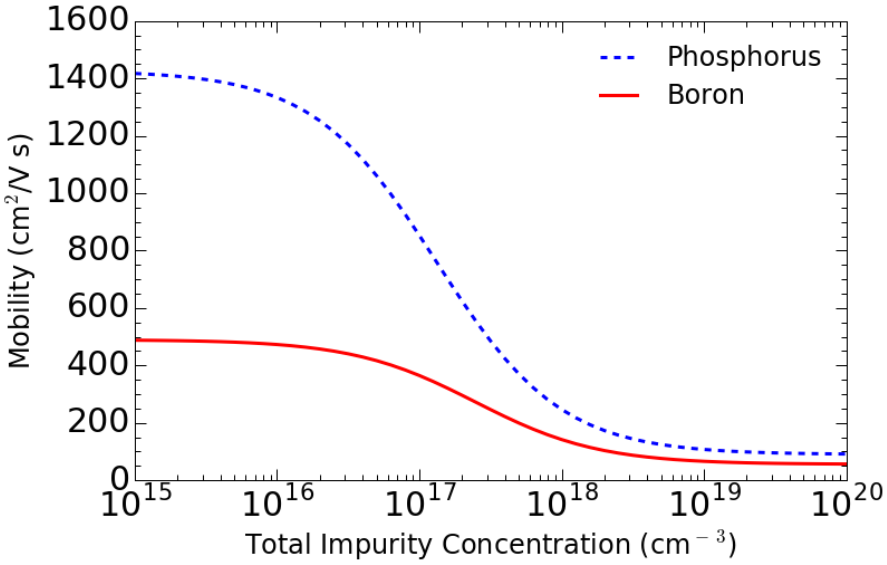

Figure 2.1: Mobility as a function of total impurity concentration as calculated from Arora, et al. [50].

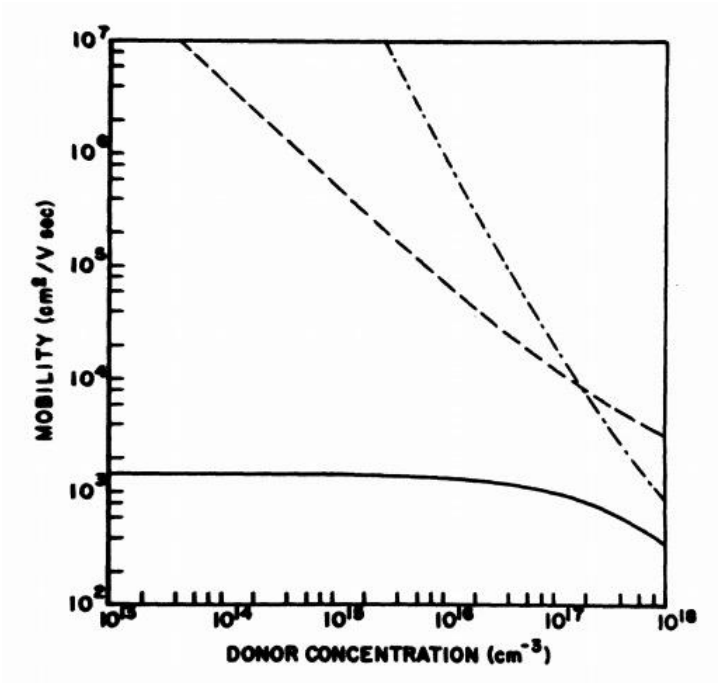

Figure 2.2: Electron mobility in n-type silicon as a function of donor concentration at 300 K. The partial mobilities for ionized impurity (dashed line) and neutral impurity (dotted-dashed line) are also shown, after [55].

Further models account for effects of electron-electron or hole-hole scattering in addition to lattice, ionized impurity, and neutral impurity scattering. Experimental findings match to within ±7% of the theoretical results [54, 56].

The Effects of Strain and Stress on Mobility and Energy Bands

The relationship between the behavior of charge carriers and strain has been thoroughly investigated both experimentally and analytically [14, 18, 44, 51, 57, 58]. The application of force to silicon shifts a band's energy [16]. In order to understand the effect of strain on mobility, the concept of energy bands and constant-energy surfaces must be presented.

Energy and momenta can be presented via *E*-*k* diagrams that characterize band structures of materials. In semiconductors like silicon and germanium, energy band extrema occur in positions that have high symmetry. In silicon, the conduction band minimum occurs in the ⟨1 0 0⟩ directions, while in germanium, the conduction band minimum occurs in the ⟨1 1 1⟩ directions, as shown in Figure 2.3. The valence band maxima always occur at k=0 and are composed of three sub-bands. For silicon the top two sub-bands are indistinguishable. The top band with less curvature is called the "heavy-hole" band while the band with larger curvature is the "light-hole" band. The lowest band with a lower maximum energy is the "split-off band" [49].

Constant-energy surfaces are a 3-dimentional visualization of the allowed *k*-values for a given energy. When the chosen energy is below the valence or above the conduction band energy, the allowed *k*-values form a surface in *k*-space in the shape of an ellipsoid [49]. Figure 2.4(a) shows the constant-energy surfaces for unstrained silicon in the ⟨1 0 0⟩ directions [59].

In n-type materials, studies use effective mass or energy band calculations to understand how lattice strain affects carrier mobility via band bending and non-uniformities in the density of states

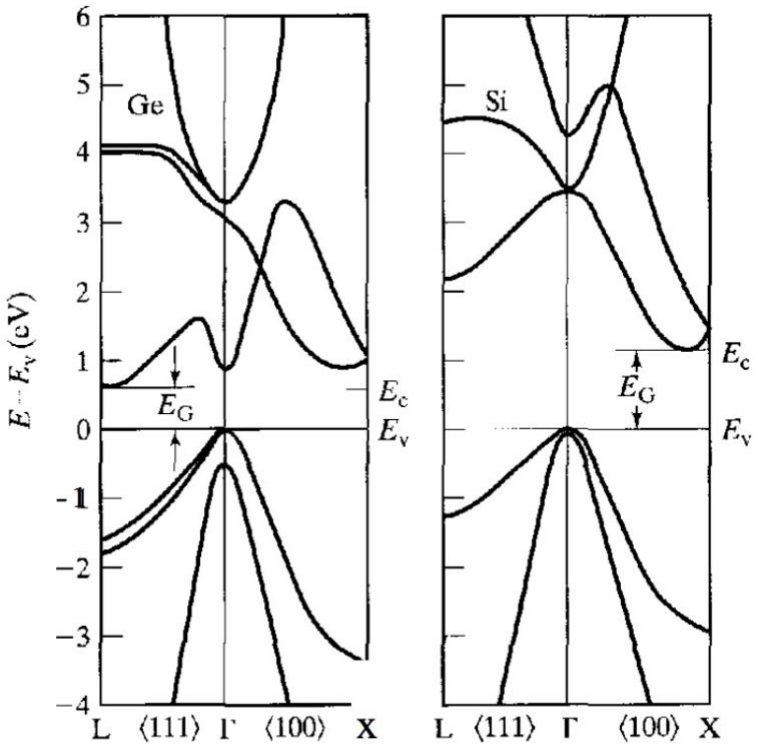

(a) (b)

Figure 2.3: ⟨1 0 0⟩/⟨1 1 1⟩ E-k diagrams showing the conduction and valence bands for (a) germanium and (b) silicon, after [49].

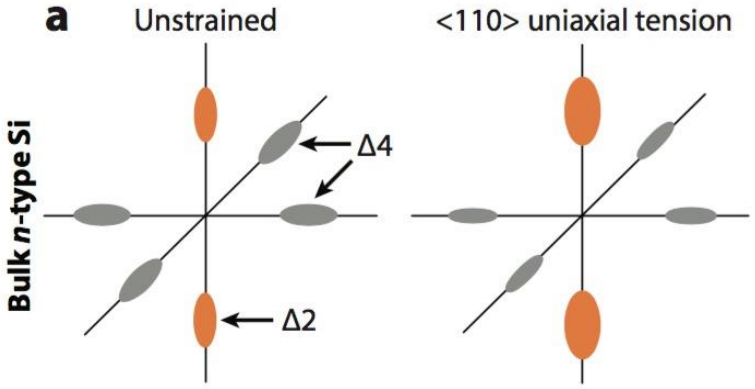

Figure 2.4: The constant energy surfaces in n-type silicon (a) unstrained and with (b) uniaxial tension, after [59].

[57, 60] Herring's "Many-Valley" model proposes the minima of the conduction bands, in the middle of the constant-energy surface, on the axis, is where mobility is highest [60]. Higher energy surfaces surround the points of lowest energy, the "valley", where electrons are found. The addition of strain to a crystal breaks the symmetry of the energy surfaces, shown in Figure 2.4(b), causing electrons to be attracted to the valleys where the energy is lower, increasing mobility. This shape means the mobility of an electron is dependent on the direction of its motion [14, 57, 61].

The shifting of the energy surface indicates a shift in the energy bands. Figure 2.4 shows how the six energy surfaces change when strain is applied in the uniaxial ⟨1 1 0⟩ direction of n-type silicon for two sets of energy surfaces, Δ2 and Δ4. When tension is applied, the energy bands on one axis to shift down (Δ2) and energy bands on two axes to shift up (Δ4). This strain results in the electrons moving from the higher energy bands to the lower. The shift in energy bands also causes a decrease in the Δ2 effective mass meaning that the shift in electrons from Δ4 to Δ2 decreases the mean effective mass and increases the mobility. Band splitting changes the scattering rate due to a decreased density of states, further aiding the increase in mobility [59].

In p-type silicon, 80% of the holes are located in the heavy-hole band, which has a higher effective mass than the light-hole band. Uniaxial compression lifts band degeneracy and causes band warping. At room temperature, band warping reduces effective mass and increases mobility. Figure 2.5 shows how the top two valence bands in silicon shift as a function of both tension and compression and notes the changes in effective mass [62]. In both tension and compression, the top band rises. The top band also warps in the ⟨1 1 0⟩ direction in both cases. Under compressive stress, the difference in energy levels between the first and second valence bands increases. The first energy band has decreased effective mass and increased mobility when strained while the second energy band has increased effective mass and decreased mobility due to strain [46, 62].

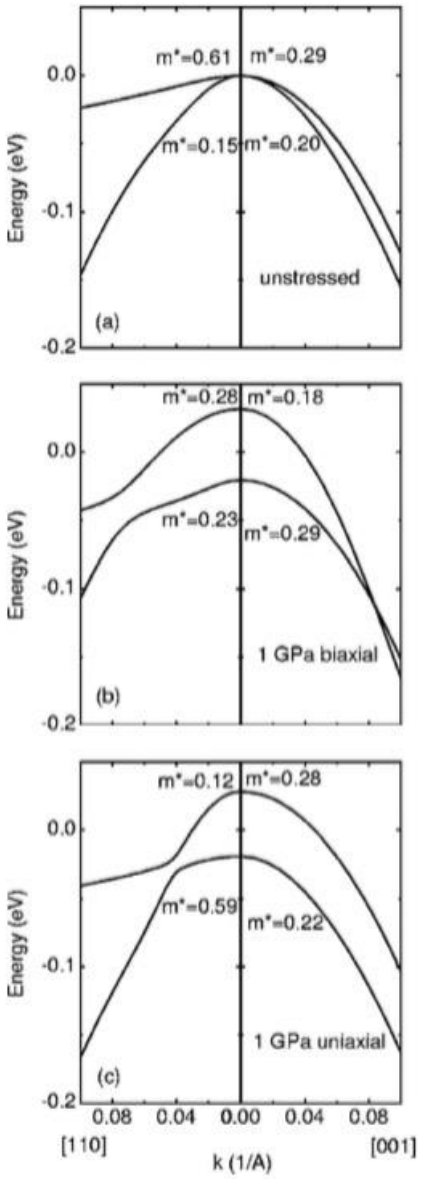

Figure 2.5: Si valence band structures for (a) unstressed, (b) 1 GPa biaxial tensile stressed, and (c) 1 GPa uniaxial compressive stressed Si. Only the top two bands are shown and effective masses are labeled in units of free electron mass, after [62].

The shift of these energy bands is responsible for carrier repopulation and scattering rate variation in Si [59]. The strain-induced band edge shift is proportional to the strain tensor and describes n-type materials well [14, 51, 59]. Strain-enhanced hole mobility depends more on band

warping than electrons and is also affected by band splitting, mass change, and changes in the densities of states [59, 63, 64].

Deformation Potential

Deformation potential theory was developed by Bardeen and Shockley to describe mobility changes from bandgap dilation [51]. The average difference in energy and band structure between the unstrained band and strained band for each of the energy valleys in energy bands from elastic strain is described by a deformation potential [65]. In a crystalline semiconductor like silicon or germanium, deformation potentials are broken into many components [57, 66]. For this work, we will focus on the shear deformation component, Ξ_u. The values of the pure shear deformation potential obtained from experimental literature contain "considerable experimental uncertainty" [65]. Including theoretical and experimental values, Ξ_u can range from 5.8 to 11.8 eV with an average value of 8.8 eV reported for silicon [26, 67, 68]. Results from Csavinszki and Einspruch indicate that deformation potential may rise with increasing dopant concentration [26]. However, the majority of research on the values of deformation potentials neglects to consider the effects of dopant type or concentration.

Piezoresistivity

Piezoresistors are widely used in pressure, force, and inertial sensors that take advantage of the change in resistivity in a material when stress is applied [14]. Piezoresistivity was first discovered in copper and iron by Lord Kelvin [69]. It was predicted by Bardeen and Shockley that single crystal semiconductors would have large mobility changes due to deformation [51]. This was later experimentally demonstrated by C. S. Smith [18]. Piezoresistivity originates from increases and

decreases in resistance due to tensile and compressive stress, respectively, changing the dimensions of the material [14, 15].

Analysis of piezoresistivity starts by defining the resistance (R) of a homogenous material as

$$R = \rho l/a \tag{2.2}$$

where ρ is the resistivity, l is the length, and a is the cross-sectional area. The gauge factor (G) is the ratio of change in resistance to mechanical strain, defined as

$$G = (\Delta R/R)/\varepsilon, \tag{2.3}$$

where $\Delta R/R$ is a fractional resistance change $\varepsilon=\Delta l/l$ is strain. The fractional change in resistivity is defined as

$$\frac{\Delta R}{R} = (1 + 2\nu)\varepsilon + \frac{\Delta \rho}{\rho} \tag{2.4}$$

where v is Poisson's ration and:

$$\varepsilon=\Delta l/l \tag{2.5}$$

is the strain [14]. The piezoresistance coefficient is then defined as the normalized change in resistivity with stress,

$$\pi = \frac{\Delta \rho}{\rho \sigma} \tag{2.6}$$

where ρ is resistivity and σ is stress. It is related to Young's modulus in that,

$$G = Y_i \pi_i \tag{2.7}$$

where i denotes the crystal direction [15, 59].

Piezoresistivity in germanium and silicon is directionally dependent because of the anisotropy of their cubic structures. This directional dependence can be leveraged to create piezoresistors that are sensitive to stress and strain in one direction, but not another. For example, a graphical representation of the room temperature piezoresistive coefficients in the (0 0 1) direction by Kanda

shows the highest piezoresistive coefficient in the ⟨1 1 0⟩ directions, as shown in Figure 2.6 [58]. The devices used in this work are fabricated with the piezoresistive base beam parallel to the [1 1 0] plane to take advantage of the larger piezoresistive coefficient in that direction [13].

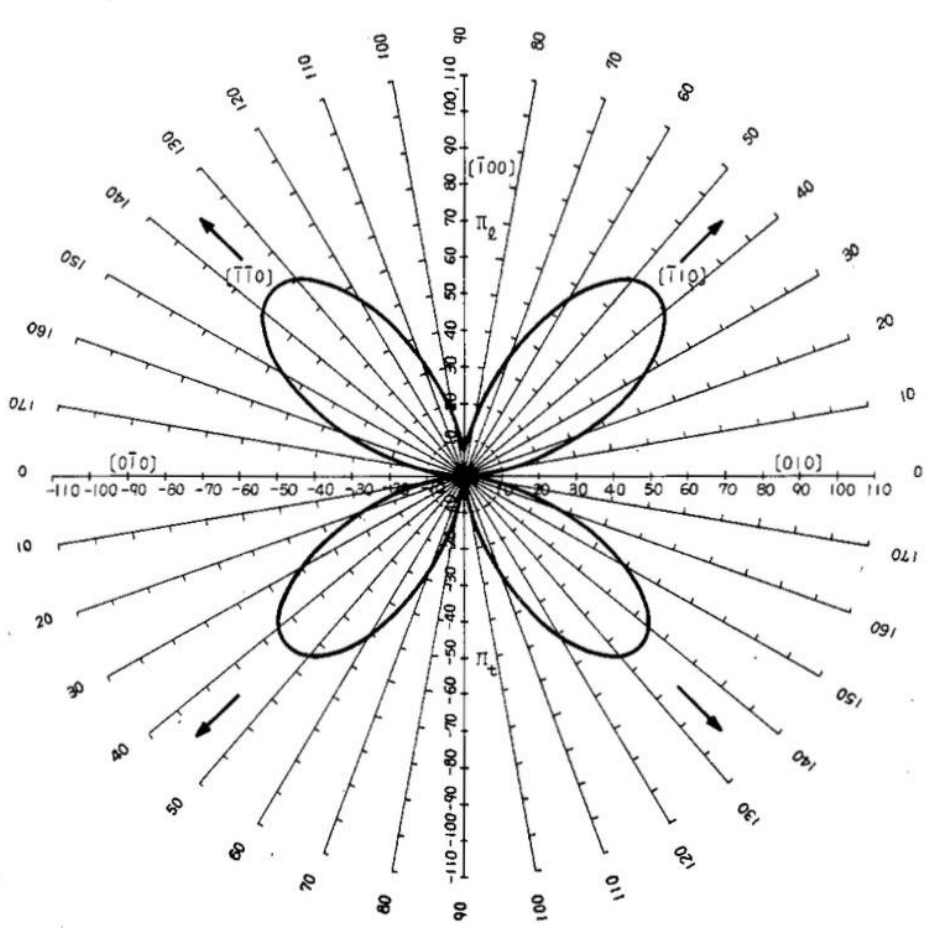

Figure 2.6: Room temperature piezoresistive coefficients in the (0 0 1) plane of p-Si (100 GPa), after [58].

Young's Modulus

The relationship between stress and strain for an isotropic homogeneous material was first conceived by Robert Hooke in 1675, presented in (1.1) as Hooke's Law [17]. As previously discussed, elasticity in silicon is directionally dependent like piezoresistivity. Silicon's cubic

symmetry allows it to be described by three independent components that form the three principle elasticities [20, 21]. The devices used in this work depend on shear elasticity because the external force is applied in the [1 1 0] direction.

In order to calculate the shear elastic constant, the effects of strain on the Fermi level are considered based on Herring's many-valley conduction band model and the deformation potentials that describe the changes in band structures due to strain. In a crystal, strain increases the energy in certain valleys depending on the direction of the force applied, shown in Figure 2.4(b). The electrons in valleys with raised energy with relocate to valleys with lower energy until the system returns to equilibrium. The transfer of electrons lowers the Fermi energy and makes a smaller contribution to the free energy of the system [70].

Elastic constants are calculated from strain derivatives of free energy. Keyes demonstrates this calculation in detail for degenerate germanium, where a sample is considered degenerate if there are more than 2×10^{17} cm^{-3} active electrical carriers [65]. These calculations have also been shown for *p*-type Si and compare to experimental measurements on samples with 3.2×10^{18} cm^{-3} boron doping [26]. The application of pure shear strain to a semiconductor changes the electronic energy in second order terms of the strain, changing the elastic constants. Energy levels for both un-strained and strained silicon are calculated by summing the energy in each of the valleys. The difference in energy levels is compared and separated into the free energy of the electron gas of the unstrained crystal, the linear energy based on energy band dilation, and the quadratic energy in the strain. The quadratic energy of the strain affects the elastic constants. Comparing the elastic strain energy to the quadratic portion of the free energy shows that only the shear elastic constant, c_{44}, is affected by applied strain to the semiconductor crystal [65].

The change in c_{44} can be shown as a function of carrier concentration for *n*-type germanium samples:

$$\Delta c_{44} = -\frac{4}{3}\left(\frac{4\pi}{3}\right)^{2/3}\left(\frac{\mathrm{m}_n^* \Xi^2 n^{1/3}}{h^2}\right) \tag{2.8}$$

where m_n* is the density of states effective mass for electrons and n is the number of electrons [65]. Similar calculations show the change in shear constant for *p*-type germanium samples, however, the more complicated nature of the energy band structure leads to a more approximate calculation where the type of shear is not distinguished:

$$\Delta C = -\frac{1}{5}\left(\frac{8\pi}{3}\right)^{2/3}\left(\frac{\mathrm{m}_p^* \Xi^2 p^{1/3}}{h^2}\right) \tag{2.9}$$

where m_p* is the density of states effective mass for holes and p is the number of holes [65].

In silicon, the orientation of the energy valleys is in the ⟨1 1 0⟩ directions rather than the ⟨1 1 1⟩ directions. This means that c_{44} should be independent of carrier concentration. Instead, the shear elasticity $C' = (c_{11} - c_{12})/2$ is affected [71]. Csavinszky and Einspruch show a comparable derivation of the effect of doping and impurities on C' accounting for separate contributions from the heavy- and light-hole bands:

$$\Delta C' = -\frac{1}{5}\left(\frac{8\pi}{3}\right)^{2/3}\frac{\Xi_s^2}{h^2}\left(\mathrm{m}_{p1}^* p_1^{1/3} + \mathrm{m}_{p2}^* p_2^{1/3}\right) \tag{2.10}$$

where the subscripts *1* and *2* represent the heavy- and light-hole bands, respectively. The addition of the split-off band can also be accounted for, but is only needed for doping above 1×10^{20} cm^{-3} [26]. It is important to note the value Δc_{44} or ΔC is in reference to un-doped silicon. Therefore, when using these equations to calculate the value of c_{44} or C for a doped sample, the shear elasticity must be calculated by:

$$C_{sample} = C_{undoped} + \Delta C. \tag{2.11}$$

While the above equations are shown using electron or hole concentrations, there is no way to differentiate between the effects of electrons or holes and ionized impurities [16].

The effects of carrier concentration of both *n*- and *p*-type materials have been well documented by a variety of studies. In general, these studies have found the comparison of theory to experimental results yields self-consistent results for *C'*. Using un-doped and 2×10^{19} cm^{-3} phosphorus-doped silicon, Hall measured elasticity by applying hydrostatic pressure to his samples. Measured changes in c_{11} and c_{12} matched well with Keyes' calculations; however, the measured values of c_{44} showed a sensitivity to doping, contradicting Keyes'. The addition of 2×10^{19} cm^{-3} phosphorus atoms comprises 0.04% of the total material, but the contribution of impurity atoms to the elastic constant results in a ~1% decrease in both c_{11} and c_{12}. The effect of doping on c_{44} was believed to result from an electronic mechanism different from Keyes' deformation potential theory. Keyes' later suggested the change in c_{44} was a "result of the splitting of the degeneracy of the conduction band at the [0 0 l] Brillouin zone face by strain" [16]. However, a promised paper on this subject was never published.

Mason and Bateman measured the propagation of acoustic waves in *p*-type Si to demonstrate that increased doping decreases c_{44} and is related to an increase in hole scattering time. Changes in c_{11} and c_{12} due to increased hole scattering were 5-10x less than the changes in c_{44}. In order to calculate the change in c_{44}, Mason and Bateman use Keyes' deformation potential model [72]. Further studies have confirmed that an increase in carriers will affect all three elastic constants and can be found in references [72, 73, 74, 75, 76, 77]. While contributions from increased dopants and carriers have been shown to affect the elastic constants, the changes seen typically only amount to a 1%-3% decrease in elasticity for heavy doping levels. In general, if an elastic constant is needed for a specific sample, the best way to obtain the value is to measure the sample itself [19].

Hydrogen in Silicon

Atomic hydrogen is introduced into silicon throughout the wafer and device fabrication processes and has complex behavior dependent on the doping [45, 78, 79, 80, 81, 82, 83]. Hydrogen can also be introduced into silicon by proton implantation, exposure to a hydrogen plasma, exposure to a hydrogen gas at high temperature, or contact with boiling water [84, 85]. The effects of hydrogen in silicon have been widely studied from a material perspective [45, 78, 79, 80, 81, 82, 83, 84, 85, 86] and from a device perspective [43, 87, 88, 89, 90, 91, 92]. The presence of hydrogen causes relaxation of the silicon crystal, which further adds to the complexities of the mechanisms by adding new defect levels [45, 79, 80, 93]. It is also likely that the interaction of hydrogen with the dopant atoms can cause changes in the carrier mobility [45, 46, 47, 94, 95]. A majority of studies on hydrogen in silicon focus on its interaction with defects and dopants such as deep-level passivation, shallow-acceptor neutralization, shallow-donor neutralization, and dissociation of hydrogen-dopant complexes [78].

Hydrogen in Si can have three different states depending on a variety of factors including dopant types: positive (H^+), neutral (H^0), or negative (H^-). When H is released in Si, its charge state is influenced by the Fermi level [79, 80, 96, 97]. Pseudo density functional theory has been used to define a model for hydrogen diffusion and reactions including the most likely locations of H atoms in the lattice, the associated crystal relaxations, and energies required for H to move within the lattice or react with dopants [79]. These calculations reveal that the typical energy for any reaction of hydrogen in silicon is in a range of ~1.5 eV or less, as shown in Figure 2.7, and that the largest change due to crystal relaxation is 0.45 Å.

Figure 2.7 shows first-principle results, based on calculations from [79], for the formation of different hydrogen species from their most likely location in the Si lattice. H^+ is the preferred state

in *p*-type silicon because it requires less energy, while H^- is the preferred state in *n*-type silicon due to a lower formation energy when the Fermi level is closer to the conduction band. H^0 does not have an energy dependence and is equally likely to form in both types of Si [45, 79, 80, 81, 96, 97].

The following sections will cover each of the H charge states and H_2 including some chemical reactions between H atoms and donors and their required energies. The positive and negative charge states are presented with their associated effects on dopants. Additionally, some measurement techniques, physical defects, and the effects of hydrogen on elasticity are presented.

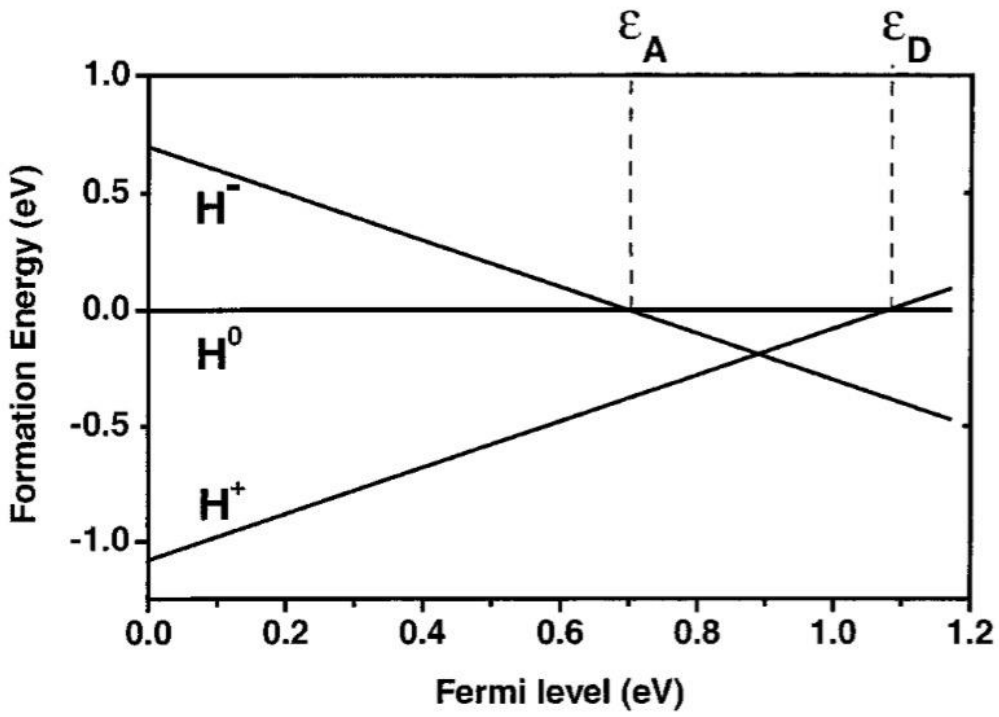

Figure 2.7: First-principles results for relative formation energies for different charge states of hydrogen interstitials in Si, as a function of Fermi level E_F with E_F=0 corresponding to the top of the valence band. The formation energy of H0 is used as a reference, after [97].

Neutral Hydrogen and H_2

Neutral hydrogen is formed in both *n*- and *p*-type Si and is highly mobile with only a 0.2 eV penalty to move through the lattice and minimal effects on lattice relaxation [79]. By gaining a hole or an electron, it can easily become H^+ or H^-, respectively [97, 98]. Two H^0 atoms may also combine, or dimerize, to form H_2 in Si. The binding energy for two H^0 atoms is ~2 eV, or about 1 eV per atom through the reaction [79, 98]:

$$2H^0 \rightarrow H_2. \tag{2.12}$$

The combination of H^0 and H^+ can also form H_2 and release a hole:

$$H^0 + H^+ \rightarrow H_2 + h^+ \tag{2.13}$$

where the binding energy will be up to 1 eV less and may explain why the binding energy of H_2 is lower than the diffusion barrier [79].

Johnson and Herring performed secondary ion mass spectroscopy (SIMS) measurements with deuterium on *p*-*n* diodes to show that reaction (a) could not account for the depth profile of H_2 [99]. Once H_2 is formed, it is highly immobile. In fact, atomic hydrogen has a diffusion coefficient that is 42 orders of magnitude greater than H_2 at 300 K [100]. The presence of H_2 can also slow atomic hydrogen in *n*-type material [93].

H^+ and Boron-Hydrogen Complexes

Denteneer, *et al.* used pseudo density functional theory and first principle calculations similar to Van de Waal, *et al.* to model the addition of a boron dopant to the silicon-hydrogen complex. If hydrogen can be a deep donor, then it can passivate boron by compensation (i.e., the annihilation of free holes from ionized acceptors) and neutralization (i.e., the pairing of a negatively charged acceptor with H^+) [80]. Once H^+ has been formed, it has high mobility and Coulombic attraction

to negatively charged acceptor impurities. Notably, the existence of H^+ does not necessarily mean that it is a proton. The missing electron can be associated with a Si atom as long as the H atom is near [79].

Any time H is near B, it is expected that it will remove the electrically active level from the gap [80]. In B doped Si, neutral hydrogen has an activation energy of ~1.2 eV and ionized hydrogen has an activation energy of ~0.8 eV [79]. H^+ in pure silicon can behave as a donor meaning that it will annihilate a free hole from an ionized boron atom, leading to acceptor-hydrogen pairs [80]:

$$H^+ + B^- \rightarrow (HB)^0 \tag{2.14}$$

or an additional electron and hole can cause acceptor compensation [101, 102]:

$$B^- + H^+ + e^- + h^+ \rightarrow (BH)^0. \tag{2.15}$$

Alternatively, an additional hole can cause acceptor passivation [103, 104]:

$$H^0 + B^- + h^+ \rightarrow (HB)^0. \tag{2.16}$$

Hydrogen causes deep-level passivation in crystalline semiconductors that passivate local defects and remove electronic states from the band gap. These centers can be found when hydrogen is introduced by high-energy ion implantation or when hydrogenated silicon is exposed to electron or gamma irradiation [78, 105, 106, 107]. Tavendale *et al.* showed the neutralization of boron dopants as a function of depletion depth. Reverse-bias Schottky and junction barrier diode capacitance characteristics were used to detect boron acceptor profiles. After exposure to H plasma, Schottky barrier diodes were reverse biased at 5 V for up to 23 h. Acceptor concentrations increased with depletion depth over time, suggesting the possibility the B-H complexes dissociated and H drifted away from the depletion layer. As more un-neutralized boron is exposed, the depletion depth returns closer to the Schottky contact. Comparison to a non-hydrogenated Schottky diode showed similar, yet less exaggerated, results showing H was present before hydrogenation.

Deuterated samples with greater doping showed similar results with depletion regions that were shallower. Their measurements found a H-related defect that neutralizes boron acceptors when exposed to hydrogen drifts like a positively charged species with an applied electric field. This indicates a donor ionization level in the upper half of the band gap [101].

Work on MOS capacitors has also shown that hydrogen can passivate shallow acceptors in boron diffused *n*-type silicon. Avalanche hole injection on devices without diffused boron show no effect on the electron density. Devices with diffused boron show an increase in net electron density as more holes are injected. This shows that a bulk compensating donor, hydrogen, can only be released when holes are already present. Another conclusion proposed from this work is that the rate of silicon-hydrogen bond breaking is as much as two orders of magnitude higher for holes than for electrons. This is because an energetic hole or capture of a thermal hole would have enough energy to break the bond while an electron needs sufficient energy to break the same bond [102].

Shallow-acceptor passivation has also been shown through the use of spreading resistance and infrared absorption measurements. Boron passivation depth varies as a function of the square root of the initial boron concentration [100]. Spreading resistance measurements made on 5×10^{18} cm^{-3} boron-doped silicon before and after deuteration show an increase in resistance over 1 order of magnitude at the surface before declining to its starting value at a depth of 0.6 μm, as shown in Figure 2.8(a). A depth profile measured by SIMS showed that deuterium concentration also plateaued at a depth of 0.6 μm, in agreement with the spreading resistance measurement, shown in Figure 2.8(b). The depth of deuterium is used because it has similar electrical properties to atomic hydrogen, but is more easily detectable by SIMS [104]. Further research by Pankove *et al.* showed hydrogen can passivate up to 99% of boron near the surface after hydrogenation for 1 h at

temperatures from 65 to 300 °C. The passivation of boron causes a large increase in resistivity and a decrease in free-carrier absorption [83, 103].

The energies required to dissociate a hydrogen-boron complex have been studied and calculated. Using total energy calculations, Denteneer, *et al.* calculated the dissociation energy of the reaction

$$(BH)^0 \rightarrow B^- + H^+ \quad (2.17)$$

to be 0.59 eV when the dissociation does not involve the release of a hole. To release a hole, the reaction is:

$$(BH)^0 \rightarrow B^- + H^0 + h^+ \quad (2.18)$$

and the energy required is 1.09 eV $-E_F$ [80]. These values, however, differ from experimental values presented in other research. Zundel and Weber found the required energy for thermal dissociate of B-H complexes to be ~1.3 eV. This was measured by monitoring active acceptor concentration depth over a ~5.5 h isothermal anneal of a reverse-biased hydrogenated Schottky diode. Using this data, calculations were made using first-order kinetics. These calculations also show the dissociation energy varies as a function of the location of the H atom with respect to the B and Si atoms in the lattice [108].

H^- and Phosphorus-Hydrogen Complexes

In *n*-type silicon doped with phosphorus, hydrogen diffusion depends on the donor concentration. When the *n*-type doping is higher, the concentration of H is lower. Hydrogen can cause shallow-donor neutralization in silicon [78]. Combined resistivity and Hall measurements on n^+-type silicon by Johnson *et al.* show a decrease in free electron concentration after hydrogenation and an increase in the effective Hall mobility [45, 109]. This is attributed to reduced ionized impurity scattering due to the neutralization of donor dopants. A depth profile shows the

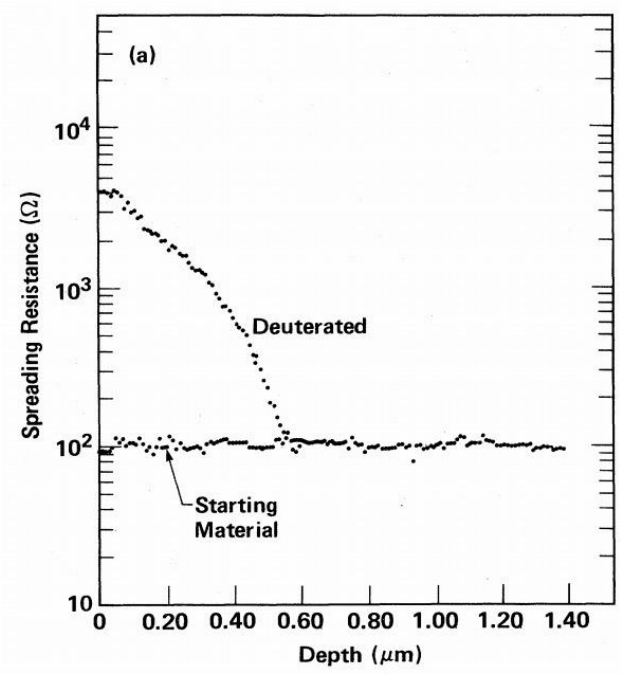

(a)

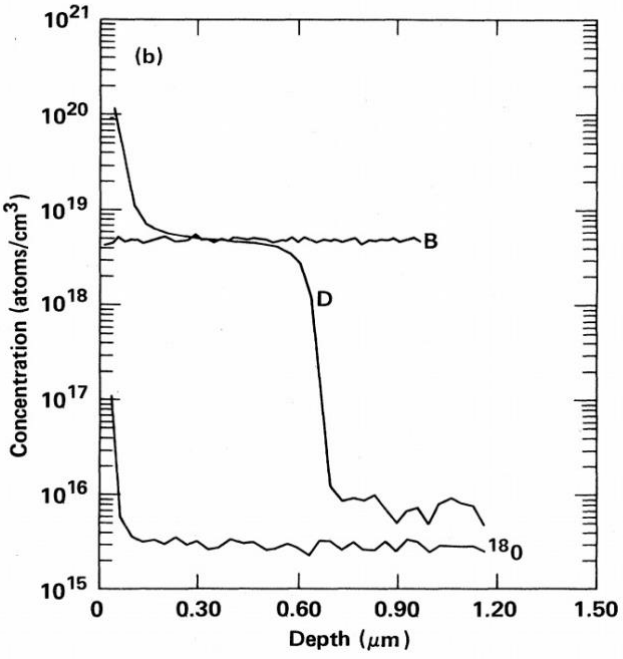

(b)

Figure 2.8: Depth profiles of spreading resistance measured with (a) deuterated hydrogen (b) in a boron doped single-crystal silicon sample after deuteration at 150 °C for 30 min. Depth profiles for boron and ^{18}O are also shown, after [104].

concentration of deuterium in phosphorus-doped silicon is more concentrated at the surface with greater phosphorus doping. At doping of 2×10^{19} cm^{-3} phosphorus, the deuterium is concentrated within the first 0.6 μm of the surface while for doping of 2×10^{14} cm^{-3} phosphorus the deuterium spreads 3 μm into the silicon. The number of shallow donors is less than shallow acceptors, which is proposed to be due to the lower dissociation energy for passivated donors [45].

Further measurements of free electron concentration and mobility in hydrogenated lightly phosphorus-doped *n*-type Si have shown that hydrogenated silicon has smaller changes in electron concentration and mobility when irradiated by electrons or gamma rays than non-hydrogenated Si. Electron mobility and conductivity measurements were taken using the Hall effect and Van der Pauw method at 78 and 293 K on 2-μm thick, phosphorus-doped Si epilayers on *p*-type substrates with Ohmic aluminum contacts. Devices showed decreased active donor concentrations after hydrogenation and slightly increased concentrations after γ-ray irradiation at 78 K. Non-hydrogenated devices showed the greatest decrease in free electron concentration after irradiation while a post-hydrogenation anneal had a negligible effect on the sample's response to irradiation. At 293 K, carrier concentration decreased after irradiation, but changes in mobility after irradiation appear negligible. Post-irradiation anneals at elevated temperatures of 100 and 150 °C for 10 min also show minimal change suggesting the γ-ray induced defects are thermally stable [105]. Electron irradiations produced similar results at 78 K, but did show a small decrease in mobility after irradiation [106].

Thermal dissociation of P-H complexes has been shown by annealing hydrogenated phosphorus-doped silicon at high temperatures. Bergman *et al.* measured the P-H dissociation energy to be 1.32 eV after 30-minute isochronal anneals [110]. Zhu *et al.* performed bias-temperature stressing

of hydrogenated Schottky-barrier diodes that showed that P-H dissociation has an activation energy of 1.18 eV and is most likely represented by the reaction:

$$PH \rightarrow P^{+} + H. \tag{2.19}$$

The binding energy of the P-H complex is then estimated to be 0.35 – 0.65 eV [96].

P-H bonds are 0.41± 0.25 eV less stable than a Si-H bond [45]. However, the addition of another H atom can reduce the energy required to dissociate the H from Si. The reaction energy of:

$$Si\text{-}H + H^{+} \rightarrow D + H_2 \tag{2.20}$$

is calculated to be 0.5 eV, where D is a dangling bond [111]. In this setup, the dissociation energy of the P-H complex is calculated to be 1.3 eV, which agrees with the experimental measurement of 1.18 eV and 1.3 eV from Zhu, *et al*. and Bergman *et al.*, respectively [96, 110, 111].

A silicon hydrogen bond can be broken without interaction from another species. However, the energy required for this reaction is high enough compared to previously mentioned reactions to suggest that it is unlikely. Work by Tsetseris, *et al*. has calculated energy of the reaction:

$$SiH \rightarrow D + H \tag{2.21}$$

as 2.4 eV, which is in agreement with the 2.6 eV found experimentally by Stathis [111, 112]. When holes are present, the dissociation energy is lowered by 0.4 eV to 1.6 eV, suggesting this reaction is still less likely.

Multiple Trapping Hydrogen

In addition to B-H and P-H complexes, research has also shown that each complex can facilitate multiple trapping of hydrogen. Korpás, *et al.* calculated two different energetically favorable configurations of a B-H pair capturing another hydrogen and five different configurations of a P-H pair capturing another hydrogen and shows that each are strong traps for H. B-H-H and P-H-H

may be traps for additional H atoms, but do not result in H_2 as the original H atom remains attached to the dopant. For B-H-H, there is only one energetically favorable arrangement, while there are six favorable arrangements for P-H-H complexes [85]. Borenstein, *et al.* created a kinetic model that similarly predicts B-H and P-H complexes trapping excess hydrogen in chains of up to 8 or 12 hydrogen atoms. The models aligned well with existing data of SIMS measurements on B-doped Si [113].

Spectroscopy and Absorbance Measurements

The presence of boron-hydrogen complexes creates new local vibrational modes that are detectable with Fourier transform infrared absorption spectroscopy (FTIR) [78]. By comparing measurements of non-hydrogenated and hydrogenated samples, FTIR shows direct evidence of boron-hydrogen complexes at wavenumbers ranging from 1870 to 1880 cm^{-1} [80, 84, 94, 104, 114]. Raman spectroscopy measurements on hydrogenated boron-doped silicon by Stutzmann similarly exhibit a peak at 1880 cm^{-1} due to the presence of the B-H complex [115]. Figure 2.9 shows both FTIR (a) and Raman (b) measurements for non-hydrogenated and hydrogenated samples. Additionally, the Raman measurement shows the peak disappears after a 200 °C anneal for 30 minutes [115].

Yong-Chang *et al.* hydrogenated a boron-diffused silicon sample with hydrogen plasma and showed using FTIR that hydrogenation had created B-H pairs due to the presence of an absorption peak at 1873 cm^{-1}. The carrier concentration and effective hole mobility were then measured as a function of thermal annealing. From temperatures of 50 to 180 °C, there was little change in either value. As the temperature increases to 200 °C, the carrier concentration starts to increase and the hole mobility starts to decrease, shown in Figure 2.10. This is attributed to the "dissolution" of the

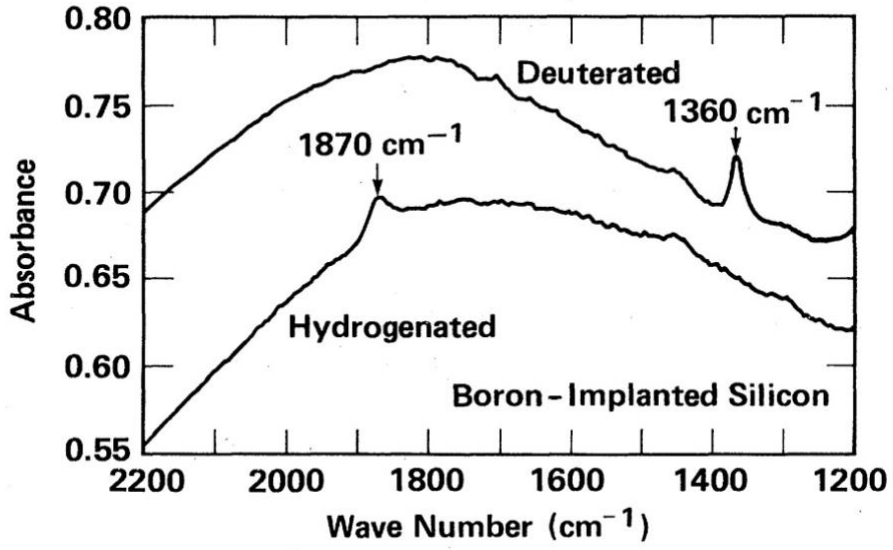

(a)

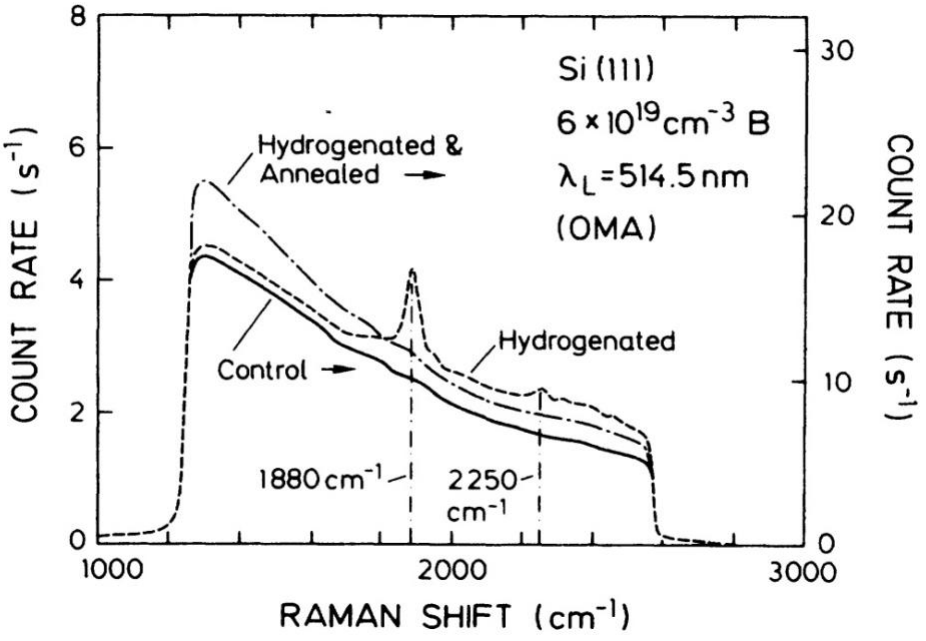

(b)

Figure 2.9: (a) Infrared absorption spectra from Fourier transform infrared spectroscopy for hydrogenated and deuterated boron-doped silicon, after [104]. (b) Raman spectra of a control, hydrogenated, and annealed boron-doped silicon sample. The solid line is the control sample, the dashed line is the hydrogenated sample, and the dotted-dashed line in the annealed sample, after [115].

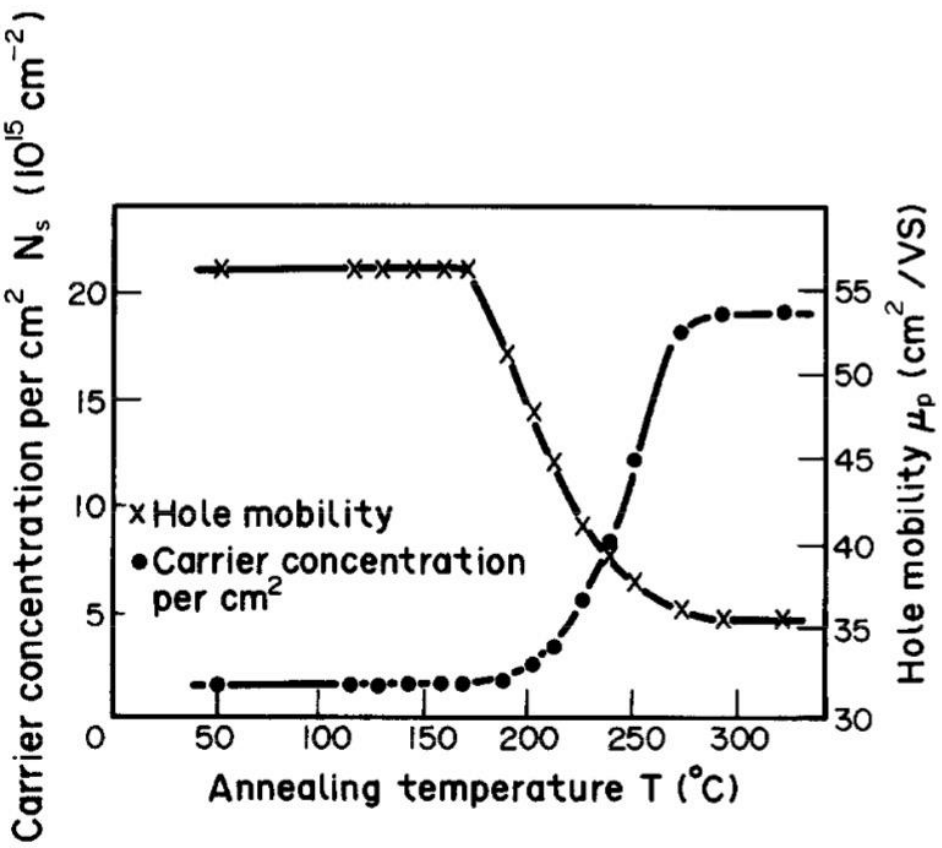

Figure 2.10: Isochronal annealing curves for carrier concentration and hole mobility in boron-doped silicon as a function of annealing temperature, after [94].

B-H pairs. The decrease in mobility is caused by ionized impurity scattering because the mean free time is less than neutral impurity scattering and therefore dominates [94].

The presence of a phosphorus-hydrogen complex shows up as an increase in infrared absorbance from FTIR measurements at 809, 1555, and 1647 cm^{-1} with the greatest absorbance occurring at 809 cm^{-1}. The passivation of donors was confirmed by spreading resistance measurements that showed 80% of donors were passivated up to a depth of 0.2 μm. There was an increase in Hall mobility that suggested that a complex formation of H bonding to Si rather than compensation was the cause of donor neutralization [110].

Physical Hydrogen Defects

When silicon is hydrogenated by exposure to H plasma or H-implantation, H ions cluster together and form planar defect clusters called platelets and microcracks that are oriented in parallel to the substrate surface with their depth depending on implantation energy [95, 116]. Transmission electron microscopy (TEM) micrographs show both *n*- and *p*-type Si exposed to monatomic H or deuterium gas discharge form platelets and microcracks within 0.1 μm of the surface of a wafer oriented along the {1 1 1} plane. SIMS measurements verify the depth profiles of the hydrogen and deuterium concentrations and Raman spectroscopy confirms the presence of Si-H bonds after hydrogenation [95]. When 42-keV H ions are implanted to 3×10^{16} cm^{-2} into (100) silicon, the platelets form parallel to the surface at a depth ~400 nm, as shown by cross-sectional TEM in Figure 2.7 [116]. Annealing leads to even larger defects in the form of nanocracks and microcracks causing catastrophic failure of the wafer in the H-implanted region, as seen in Figure 2.11 [116, 117]. These experiments demonstrate how H defects in Si can be highly localized and close to the surface of a wafer.

Effects of Hydrogen on Elasticity

Hydrogen implantation affects the shear modulus of silicon. Shear modulus was measured in Si with an implanted fluence of 6×10^{16} cm^{-2} H^+ ions using biaxial stresses and out-of-plane strains and compared to the depth profile of implanted H-concentration. Results show that the shear modulus decreases by a factor of 2 in the H-implanted Si and is highly dependent on the local concentration of H [117].

Nanoindentation techniques where force and displacement are measured as an indenter is pressed into the surface of a material are used to measure the effects of hydrogen implantation on hardness

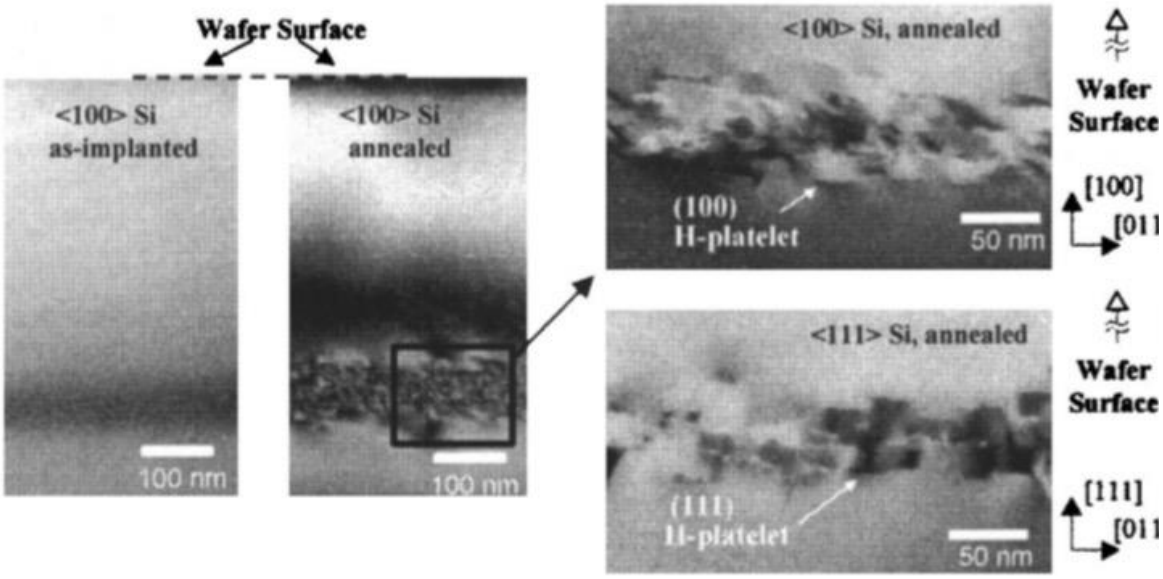

Figure 2.11: Cross-sectional TEM micrographs from implanted and annealed Si. Implanted H is shown at a depth of ~400 nm. Platelet formation is shown in parallel to the wafer surface in both (1 0 0) and (1 1 1) directions after annealing, after [116].

and elasticity [118, 119, 120]. Gu *et al.*, found that implanted H ions in (1 0 0) silicon formed platelets filled with H_2 in the (0 0 1) plane. Nanoindentation measurements indicated the elasticity had decreased due to the hydrogen [119]. Lightly boron-doped (1 0 0) silicon with implanted hydrogen concentrations up to 3.2×10^{21} cm^{-3} in the near-surface regions showed increased hardness and decreased elasticity with increasing H-implantation [120].

Hydrogenation has been shown to affect plasticity in silicon [121]. While elasticity represents non-permanent deformation, plasticity is the tendency for permanent deformation. Un-doped, lightly (10^{13} cm^{-3}), and heavily (10^{19} cm^{-3}) boron-doped silicon samples were hydrogenated for 30 minutes by being boiled in deionized water. Nanoindentation tests showed hydrogenation had no effect on the un-doped silicon due to a lack of dopant interactions. In the lightly-doped samples, plastic deformation was the greatest because H-diffusion is greater with less doping. In the highly-

doped samples, the H-diffusion is limited so that H accumulated closer to the surface causing some plastic deformation, but less than the lightly-doped samples. When the highly-doped samples were hydrogenated for 8 hours, the amount of plastic deformation greatly increased. This experiment shows that hydrogen leads to the softening of silicon [121].

Dose Rate and Dopant Type Response to Ionizing Radiation

The effects of total ionizing dose on semiconductors were first published in 1964 by Hughes and Giroux [122, 123]. A majority of the research effort in TID effects has focused on MOS and bipolar technologies with an emphasis on charge and trap generation in the oxide and at the interface between oxides and semiconductors [98]. Ionizing radiation from gamma rays and X-rays creates electron-hole pairs in Si and the native oxide due to Compton scattering or the photoelectric effect, respectively [98, 124]. When a voltage is applied across either material, transporting carriers can lead to surface charging of the native oxide [125, 126] as well as the release of hydrogen in the Si and native oxide [43, 86, 93, 98, 111, 127, 128]. The radiation effects most relevant to this work concern dose rates and the interactions of transporting hydrogen concentrations in silicon. The radiation effects at the SiO_2/Si interface may also play an important role in the mechanisms present in the cantilevers and resistors used in these experiments. Additionally, this section will briefly summarize some results concerning differences in X-ray response in n^+/p and p^+/n diodes.

Dose Rate Effects

A dose rate effect is different from a time-based effect in that the TID response of a circuit or device depends on the dose rate. In a time-dependent effect, a similar result is obtained after the same total dose where the measurement for the higher dose rate irradiation is taken after the same

amount of time that is required for the lower dose rate irradiation [129, 130]. Dose rate effects have been investigated in a variety of devices from CMOS capacitors and invertors to bipolar junction transistors (BJTs) [43, 88, 131, 132]. The mechanisms of enhanced low dose rate sensitivity (ELDRS) in BJTs invoke hydrogen reactions and transport as likely causes of the dose rate effect seen [43, 87, 89, 90, 91]. While a majority of this research has focused on the interaction of hydrogen with interface traps, there has been some focus on the effects of liberated hydrogen in bulk silicon relevant in the silicon cantilevers and resistors used here [43].

The mechanism for ELDRS is often related to space charge effects due to slowly transporting holes [91, 128, 133]. At higher dose rates, e.g., greater than 10-100 rad(Si)/s, the space charge is great enough that it slows the transport of holes and protons to the Si/SiO_2 interface [129, 134]. Electrons can recombine with holes via annihilation or compensation before H^+ can be released by the holes and form interface traps [135]. At lower dose rates, the space charge is less, allowing for easier transport of protons and holes leading to a greater amount of oxide charge [129, 134]. The release of H^+ by holes can occur with higher probability before electron-hole recombination. The cross section for electron capture by H^+ is smaller by orders of magnitude compared to a slowly transporting or metastabily trapped hole. The increased release of protons at lower dose rates will increase interface trap formation and enhance gain degradation in BJTs [135]. Further mechanisms related to ELDRS have been proposed by Hjalmarson *et al.*, based on bimolecular processes where there is competition between hydrogen dimerization and the formation interface traps [43, 87].

Simulations using the Florida Object Oriented Device Simulator (FLOODS) confirm that the concentration of H_2 affects the number of interface traps formed during irradiation. At low H_2 concentrations, proton generation will depend on vacancies. As H_2 content increases, protons will be generated by H_2 cracking and increase interface trapping creating higher concentrations of

protons. At low dose rates, proton concentration will be lower and radiation response will be dominated by interface-trap passivation [130, 136].

A smaller portion of research has focused on hydrogen interactions in bulk silicon due to ionizing irradiation. Dopant deactivation has been shown to play a role in the ELDRS mechanism [131]. In *p*-type silicon, ionizing radiation can deactivate boron acceptor atoms via acceptor passivation [83, 104], reaction (2.23), or acceptor compensation, reaction (2.24). Capacitance-voltage measurements of boron-doped *p*-type MOS capacitors show a decrease in capacitance when irradiated with ^{60}Co γ-rays, indicating a decrease in doping with a maximum amount of deactivation occurring when the silicon surface is depleted. In accumulation, H^+ ions and holes are not available for the deactivation process. In inversion, the deactivation process moves into the bulk due to the lack of H^+ ions and holes in the depletion region [131, 137].

Dopant Type Effects

The effects of X-rays have been studied as a function of doping type in silicon diodes. Caussanel *et al.*, studied the differences in radiation response of abrupt p^+/n and n^+/p diodes using carrier lifetime measurements. There was less effect on carrier lifetime and I-V curves in the p^+/n type diodes than the n^+/p diodes. The results are attributed to more trapping occurring in the oxide above the p^+ silicon and more bulk trapping in the n^+ silicon [138].

CHAPTER 3

EXPERIMENTAL SETUP AND RESULTS

Experimental Details

The cantilevers and resistors used in these experiments have a beam width of 8 μm with three doping profiles, as shown in Table 3.1. For an 8-μm cantilever, the theoretical resonance frequency from (1.6) is ~25.4 kHz. However, due to the fabrication process, the measured resonance frequency is typically within ± 4% of 20.1 kHz.

In addition to those doping profiles, experiments comparing hydrogen content were performed with a set of 5×10^{18} cm^{-3} boron-doped cantilevers and resistors that were hydrogenated in a steam bath for 1 h before irradiation. The devices were hydrogenated while being suspended face-up, 6 inches over boiling water. Immersing silicon in boiling water hydrogenates the silicon while not damaging the crystal lattice like ion implantation. Hydrogenation passivates some of the boron dopant atoms, reducing carrier concentration [139, 140, 141]. Previous work reported Hydrogen injection and neutralization have decreasing efficiency with increasing resistivity (i.e. lower doping). While the authors were unable to propose a definitive mechanism, they suggested the injection process may be increasingly inefficient at higher resistivities because of "a Fermi level, charge state-controlled reaction involving surface state species that are the source of the hydrogen defect (possibly OH complexes)" [139]. The effect of hydrogenation can be seen as deep as 5 μm from the silicon surface. The volume density of hydrogen introduced to silicon from immersion in boiling water is typically higher than the overall doping of a sample [139]. Complex models accounting for diffusion of each H species and other possible traps are in agreement with

experimental results [142]. A steam bath has a similar temperature to immersing a device in boiling water, but most likely introduces less hydrogen.

For the purposes of this dissertation, the 5×10^{18} cm^{-3} boron-doped devices will be referred to the "higher-doped *p*-type" devices, the hydrogenated 5×10^{18} cm^{-3} boron-doped devices will be referred to as "hydrogenated" devices, the 4×10^{17} cm^{-3} boron-doped devices will be referred to as "lower-doped *p*-type" devices, and the 4×10^{17} cm^{-3} phosphorus-doped devices will be referred to as "lower-doped *n*-type" or "*n*-type" devices. The cantilevers and resistors in this work were irradiated at three dose rates, 30.3, 10.9, and 5.4 krad(SiO_2)/min, which will be referred to as high, middle, and low dose rates, respectively.

Table 3.1: Dopant Type and Concentration

Dopant (Type)	Dopant Concentration (cm^{-3})	Resistivity (Ω-cm)
Boron (*p*)	5×10^{18}	0.0145
Boron (*p*)	4×10^{17}	0.0772
Phosphorus (*n*)	4×10^{17}	0.0394

Figure 3.1 is a schematic diagram of the setup used to electrically detect the resonance frequency of the cantilevers. A Tektronix AFG3252 function generator is used to apply an AC driving signal to the gate electrode and create an electric field across the end of the cantilever beam. A Keithley 2410 source-meter is used to apply a DC voltage across the drain and source electrodes of the beam anchor of the cantilever and measure current. As the cantilever oscillates, the current changes in the beam anchor, creating a voltage drop in the series resistor (*R* in Figure 3.3). This voltage drop is the input to an EG&G 5210 Lock-In Amplifier and is compared to the AC signal driving the cantilever. The lock-in amplifier compares the reference signal to the output of the base of the cantilever by multiplying the two frequencies and integrating over 300 μs intervals to create a DC

voltage that represents the difference between the two signals while ignoring any other contribution to the cantilever signal [31, 139]. An Agilent 34401A multimeter is used to measure the DC voltage output of the lock-in amplifier. The measurement conditions for each of the three dopant type and concentration combinations used are listed in Table 3.2. The DC voltage across the base is increased for devices with lower doping to compensate for higher resistivity. The AC voltage on the *n*-type cantilevers is lower to avoid driving the cantilever into an asymmetric resonance mode. The DC voltage is higher on the *n*-type devices to accommodate for the smaller amount of displacement in the base beam. Series resistance values were intended to match the base beam resistance. The resistors were measured using a Keithley 2410 in 4-wire measurement mode and resistivity is calculated based on the dimensions of the cantilever base.

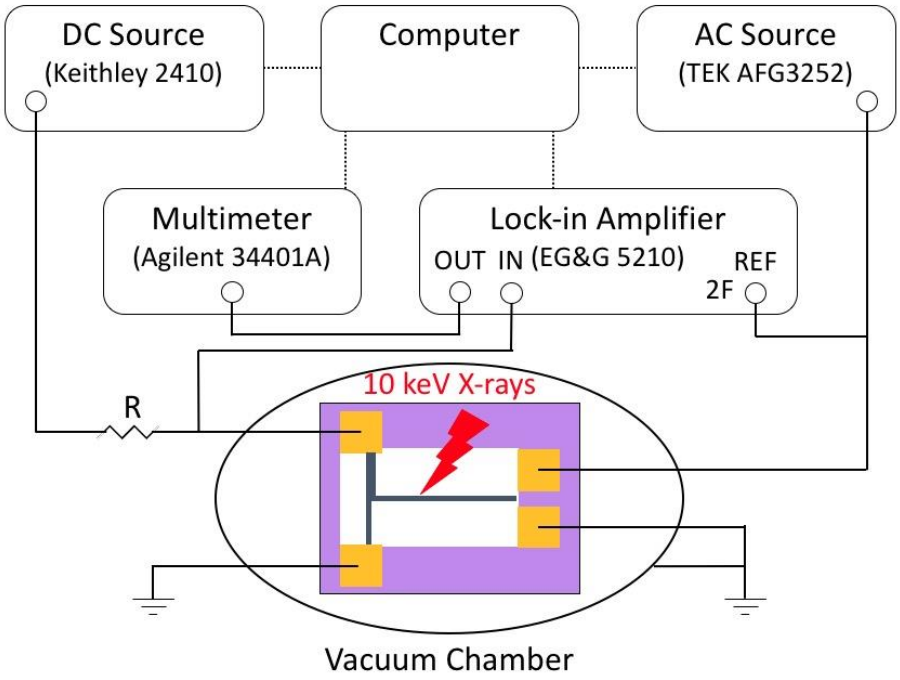

Figure 3.1: Electrical measurement setup for the piezoresistive micromachined MEMS cantilever.

All cantilevers and resistors were irradiated using a 10-keV X-ray source in a vacuum chamber with a 25.4-μm thick beryllium window that reduces X-ray intensity by ~0.3% [23]. Beryllium is used due to its low atomic number and low density, which gives a low absorption coefficient for X-rays [144]. Devices were operating dynamically before, during, and after irradiation. Each

Table 3.2: Device Measurement Conditions

Dopant (Type)	V_{dc} (V)	V_{ac} (V_{pp})	Base Current (mA)	Series Resistance (Ω)
Boron (*p*)	0.05	4.0	0.083	265
Boron (*p*)	2.0	4.0	0.18	10000
Phosphorus (*n*)	9.5	1.0	0.5	1000

device was swept over a 4 Hz range containing its resonance peak. Experiments were performed at a temperature of ~295 K and pressure of ~$1x10^{-4}$ mbar. Each cantilever was in vacuum for a minimum of 12 h before irradiation to allow the cantilevers to outgas and ensure pressure stability. Figure 3.2 shows (a) the stability of the resonance frequency of a representative cantilever before irradiation, and (b) a sample of the resonance peak frequency shifting lower during a 5.4 krad(SiO_2)/min test.

Resistors were measured using 1 mA current bias using the corresponding voltage to calculate the resistance. The devices were biased during irradiation with a measurement taken every 10 seconds. All devices were monitored for post-irradiation behavior at room temperature for 20 h or until the resonance frequency or resistivity had recovered or exceeded its pre-irradiation value.

For each doping profile, including the hydrogenated devices, at least two 8-μm cantilevers were irradiated to 1 Mrad(SiO_2) total dose at both 5.4 and 30.3 krad(SiO_2)/min. Two higher-doped *p*-type devices were irradiated at 10.8 krad(SiO_2)/min to 1 Mrad(SiO_2). One higher-doped *p*-type device each was irradiated to 200 krad(SiO_2) at 5.4 and 10.8 krad(SiO_2)/min to explore the dose

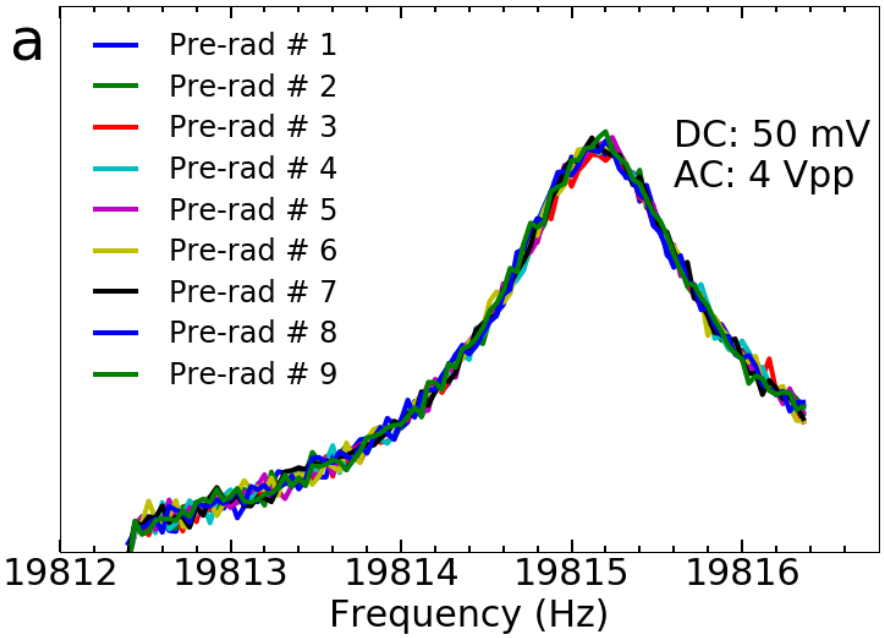

(a)

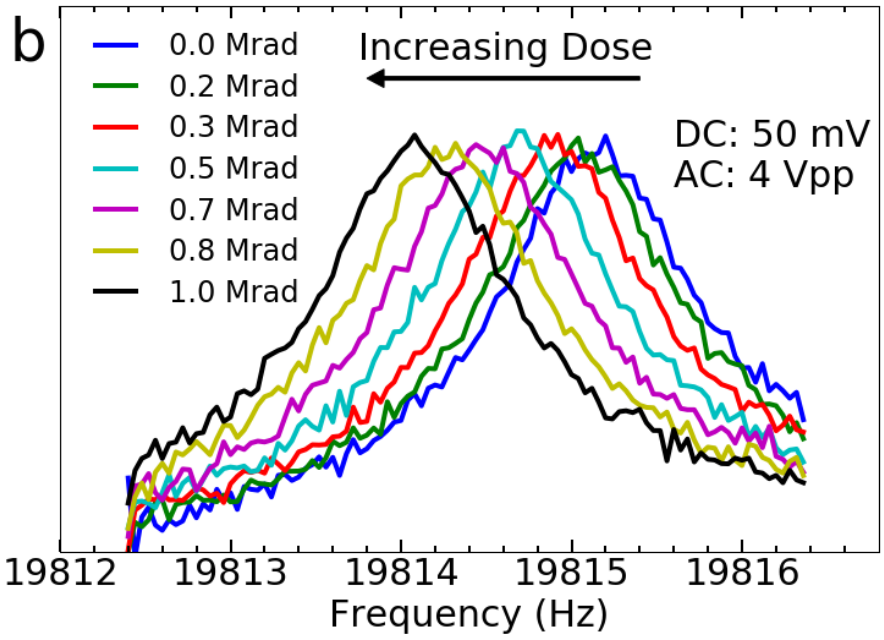

(b)

Figure 3.2: Frequency response of the cantilever near the resonance peak (a) for 9 repeated sweeps before irradiation, showing the device stability, and (b) as a function of increasing dose.

rate effect and evaluate if annealing rates are constant [88]. In some cases, only one resistor was irradiated as the intent of the resistivity measurements is to supplement the understanding of the effect of ionizing radiation on Young's modulus and resonance frequency.

Experimental Results

Resonance Frequency Results

Each resonance sweep is fit with a combination of linear and Lorentzian function to determine the resonance frequency. In general, this fit slightly underestimates the resonance frequency. However, the underestimation is consistent across all devices, filters out noise that may be present at the resonance frequency, and provides a clearer result than selecting the highest point at a 0.04 Hz resolution. An example frequency sweep of a device is shown in Figure 3.3.

Figures 3.4 and 3.5 show the fractional change in resonance frequency and resistivity as a function of dose for devices irradiated at 30.3, 10.9, and 5.4 krad(SiO_2)/min. Error bars represent one standard deviation of the resonance frequency or resistivity tested at a given total dose. Tables 3.3 and 3.4 shows a summary of results after exposure to 1 Mrad(SiO_2) total dose for both resonance frequency and resistivity. At least 2 devices were tested for each set of conditions, except for the following: one 4×10^{17} cm^{-3} *n*- and *p*-type resistor and one hydrogenated resistor at each dose rate and one resonator each at 10.9 and 5.4 krad(SiO_2)/min up to 200 krad(SiO_2) total dose have been irradiated.

The resonance frequency decreases after irradiation to 1 Mrad(SiO_2). Cantilevers irradiated at a dose rate of 30.3 krad(SiO_2)/min all show similar negative shifts in resonance frequency after exposure up to 1 Mrad(SiO_2) total dose, as shown in Figure 3.4. Their response appears to be linear with dose. Cantilevers irradiated at a dose rate of 5.4 krad(SiO_2)/min show two distinct shifts in

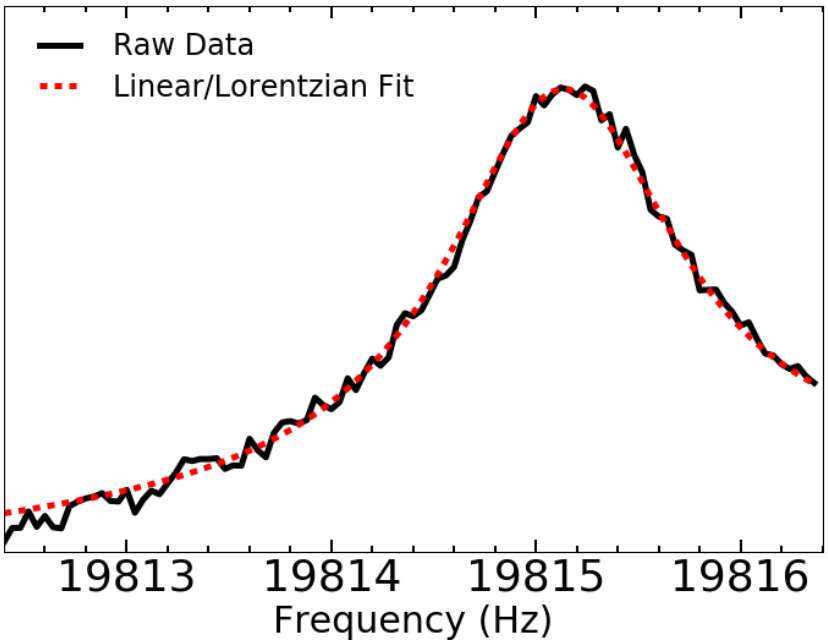

Figure 3.3: An example resonance frequency sweep (solid black line) and linear and Lorentzian fit (dashed red line).

Table 3.3: Resonance Frequency Shifts After 1 Mrad(SiO_2) Total Dose

Dose Rate (krad(SiO_2)/min)	Doping (cm^{-3})	Change After Irradiation (ppm)	Maximum Change (ppm)	Difference
30.3	5×10^{18}	-12	-20	8
10.9	5×10^{18}	-15	-32	17
5.4	5×10^{18}	-33	-44	11
10.9	5×10^{18} (200)	-2.2	-10	7.8
5.4	5×10^{18} (200)	-5	-27	22
30.3	5×10^{18} (H)	-10	-20	10
5.4	5×10^{18} (H)	-55	-67	12
30.3	4×10^{17} (NC)	-12	-30	18
5.4	4×10^{17} (NC)	-60	-72.5	12.5
30.3	4×10^{17} (N)	-10	-25	15
5.4	4×10^{17} (N)	-53	-64	11

(200) = 200 krad(SiO_2) total dose, (H) = Hydrogenated, (NC) = No cavity, (N) = *n*-type

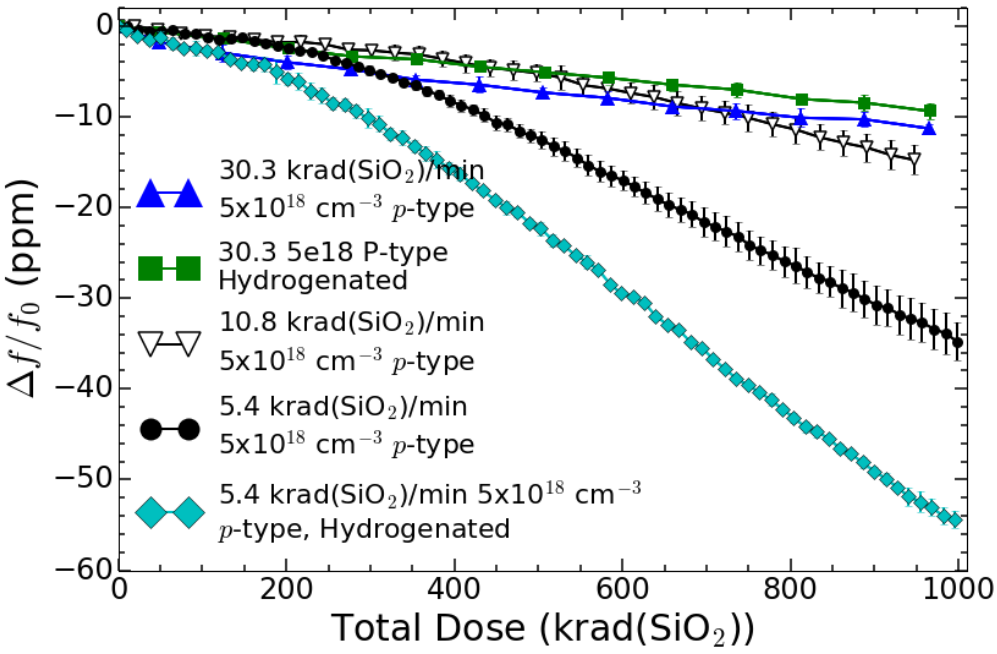

(a)

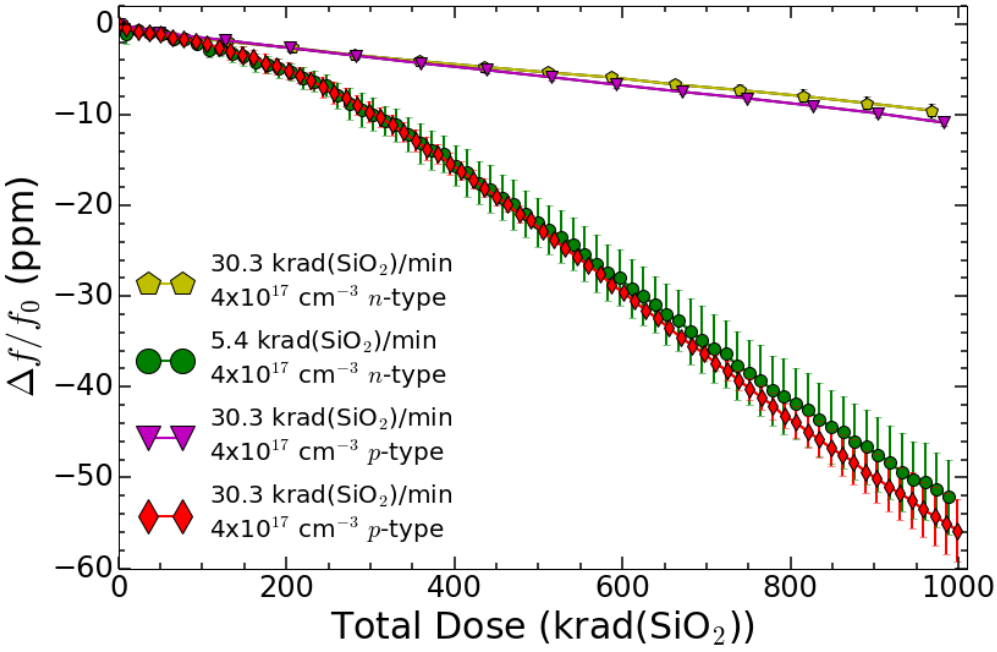

(b)

Figure 3.4: Resonance peak as a function of total dose for (a) 5×10^{18} cm^{-3} *p*-type devices irradiated at 5.4, 10.9, and 30.3 krad(SiO2)/min and for 5×10^{18} cm^{-3} *p*-type hydrogenated devices irradiated at 5.4 and 30.3 krad(SiO2)/min and (b) for 4×10^{17} cm^{-3} *n*- and *p*-type devices irradiated at 5.4 and 30.3 krad(SiO2)/min. Error bars are one standard deviation.

resonance frequency after exposure up to 1 Mrad(SiO_2) total dose, as shown in Figure 3.4. Higher-doped *p*-type devices show -33 ppm shift in resonance frequency while the hydrogenated devices and lower-doped *n*- and *p*-type devices show a shift of ~-56 ppm. The resonance frequency shifts of the lower-doped and hydrogenated devices are ~1.7x greater than the higher-doped *p*-type devices. Devices irradiated at 5.4 krad(SiO_2)/min all exhibit a slower rate of change that accelerates from 0 to ~400 krad(SiO_2) before becoming linear from ~400 krad(SiO_2) to 1 Mrad(SiO_2). The 4×10^{17} cm^{-3} *p*-type cantilever without a cavity has a slower change in resonance frequency at lower total dose, but after 500 krad(SiO_2) has a greater rate of change than the hydrogenated and *n*-type cantilevers. Higher-doped *p*-type cantilevers irradiated at 10.9 krad(SiO_2)/min to 1 Mrad(SiO_2) total dose showed a resonance frequency shift of -15 ppm, shown in Figure 4.2(a). These results are similar in shape to the 5.4 krad(SiO_2)/min dose rate results between 0 and 400 krad(SiO_2).

The resonance frequency shift of the device irradiated at the middle dose rate was ~1.5x greater than that of the device irradiated at high dose rate after 1 Mrad(SiO_2). However, at lower total doses, the resonance frequency decreased less at the middle dose rate for these devices than the devices irradiated at the high dose rate. The higher-doped *p*-type cantilevers irradiated at the low dose rate showed a negative resonance frequency shift ~3x greater than the high dose rate devices. The hydrogenated and lower-doped cantilevers irradiated at the low dose rate showed a resonance frequency shift ~5x greater than the high dose rate devices.

Figure 3.5 shows the shifts in resonance frequency as a function of dose rate for (a) higher-doped *p*-type and (b) hydrogenated devices. The shifts in resonance frequency as a function of dose rate for the lower doped *n*- and *p*-type cantilevers are so similar to the hydrogenated cantilevers they can be represented by the same plot.

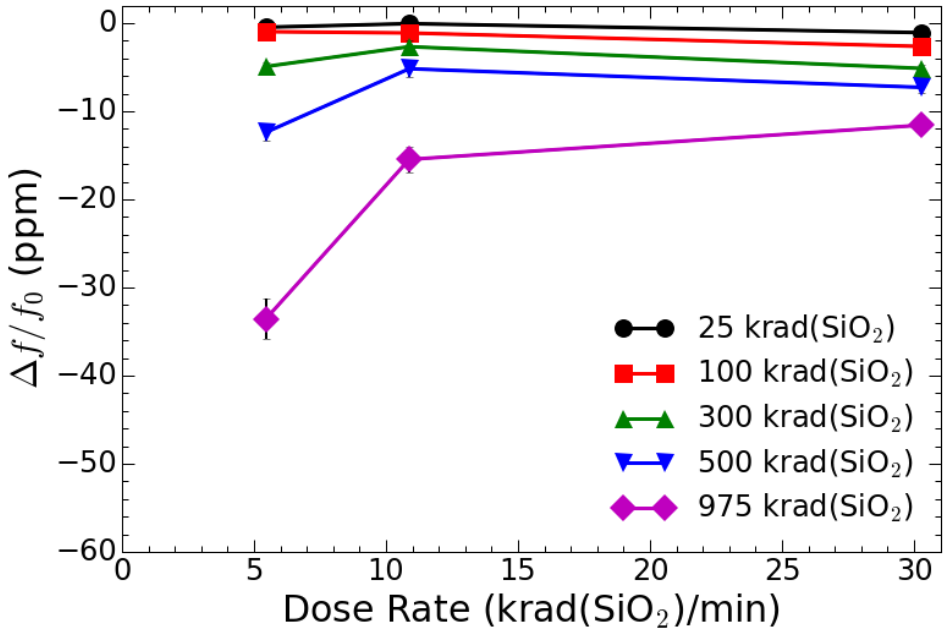

(a)

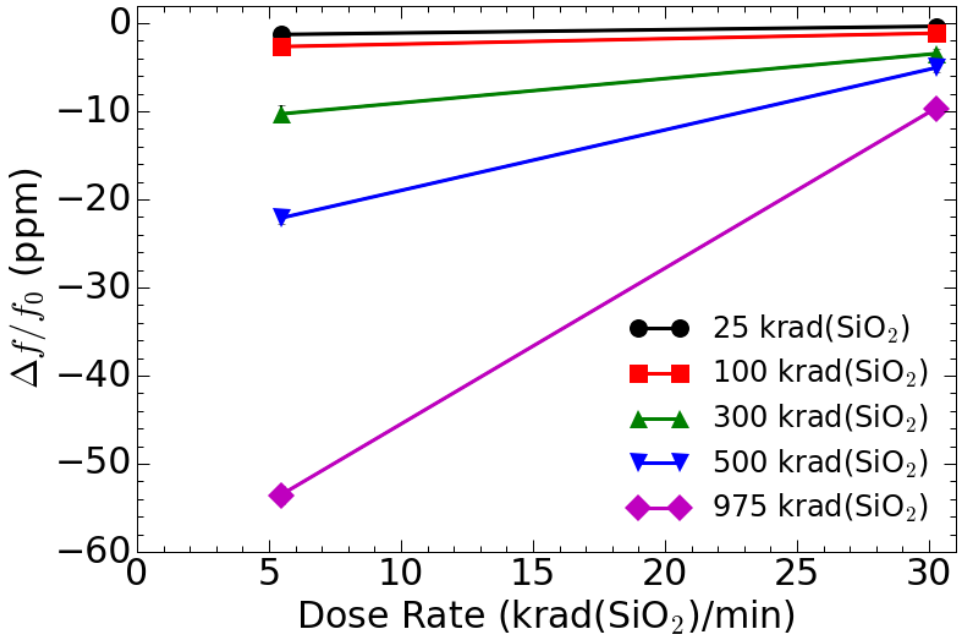

(b)

Figure 3.5: Resonance peak as a function of dose rate (a) for devices irradiated at 5.4, 10.9, and 30.3 krad(SiO_2)/min, and (b) for hydrogenated devices irradiated at 5.4 and 30.3 krad(SiO_2)/min. Error bars are one standard deviation. Lines are aids to the eye.

Resistivity Results

The resistivity in each sample increased after irradiation to 1 Mrad(SiO_2), as shown in Figure 3.6 and Table 3.4. Notably, the magnitude of change in the 5×10^{18} cm^{-3} *p*-type resistivity was greater than the hydrogenated resistivity at both the high and low dose rate, which is opposite of the effect seen for resonance frequency. The 4×10^{17} cm^{-3} resistivities for both dopant types show much greater increases in resistivity than either of the higher-doped devices, with the *n*-type resistivity increasing an order of magnitude more than the 5×10^{18} cm^{-3} *p*-type resistivity after 1 Mrad(SiO_2) at the high dose rate. The 4×10^{17} cm^{-3} *p*-type resistivity showed a ~6.6x increase over the 5×10^{18} cm^{-3} *p*-type resistivity at the high dose rate and a ~4.7x increase at the low dose rate.

The shapes of the *p*-type resistivity changes are similar to the resonance frequency shifts at both dose rates. Resistivity shifts at the high dose rate appear linear with total dose, while the low dose rate shifts show a slower rate of change from 0 to ~400 krad(SiO_2) before the rate of change becomes linear to 1 Mrad(SiO_2). The *n*-type resistors, however, show a great initial shift at lower total doses before becoming linear.

In all cases, the resonance frequency continued to decrease and resistivity continued to increase after irradiation before recovering to or beyond their initial values. Figs. 3.7 and 3.8 show a comparison as a function of time for resonance frequency and resistivity results. Regardless of dopant type, dopant concentration or hydrogen content, each device recovered to or beyond its pre-irradiation resonance frequency value approximately 10 hours after the beginning of irradiation. The resistors irradiated at the low dose rate recover to their pre-irradiation values after 10 h, as well. Notably, the resistivity for resistors irradiated at the high dose rate do not appear to fully recover.

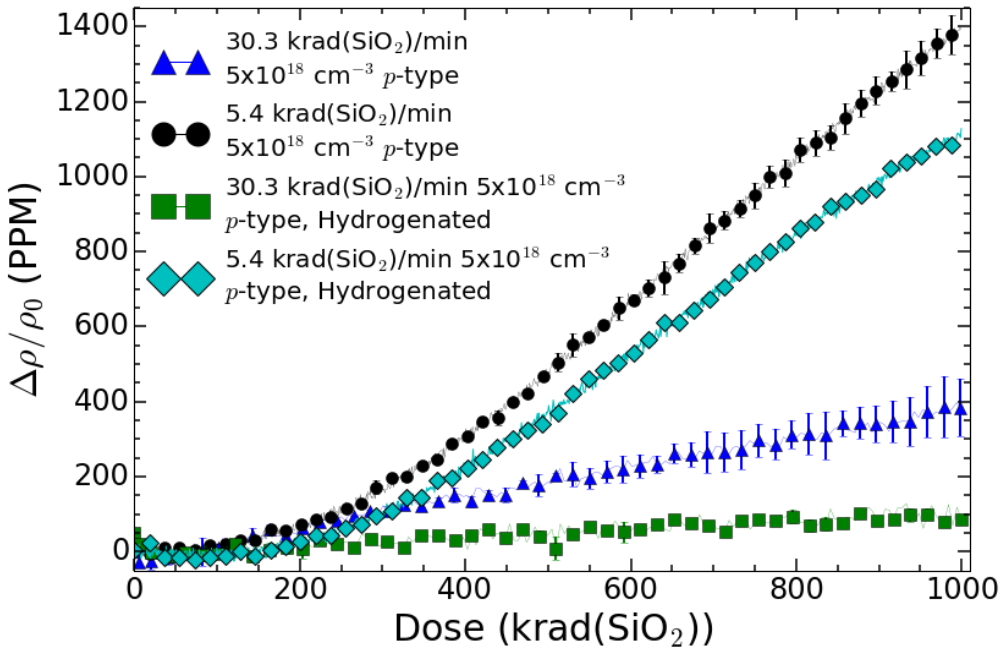

(a)

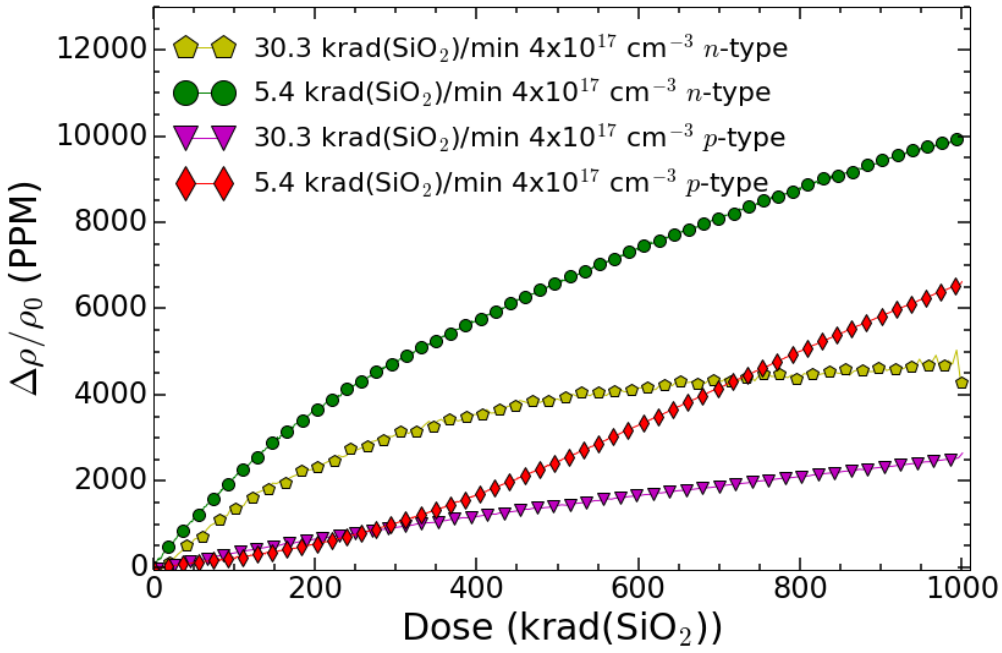

(b)

Figure 3.6: Change in resonance frequency as a function of dose for (a) non-hydrogenated and hydrogenated 5×10^{18} cm^{-3} *p*-type and (b) 4×10^{17} cm^{-3} *n*- and *p*-type devices irradiated at 5.4 and 30.3 krad(SiO_2)/min.

The corresponding minimum resonance frequency and maximum resistivity occurs around the same time for all devices, suggesting that the two effects are related to one another. The minimum resonance frequency values are listed in Table 3.3 and the maximum resistivity values are listed in Table 3.4. Additionally, the differences between end of irradiation values and the minimum resonance frequency and maximum resistivity values are listed in each table.

The post-irradiation trends continue for ~2 hours and ~1.5 hours after the end of irradiation before reversing towards pre-irradiation values for devices irradiated at 30.3 and 5.4 krad(SiO_2)/min, respectively. For cantilevers irradiated at 10.9 krad(SiO_2)/min, the resonance frequency continues to decline for 1.75 hours, before recovering.

Total Dose Comparison

A comparison of 5×10^{18} cm^{-3} *p*-type cantilevers irradiated to 200 krad(SiO_2) and 1 Mrad(SiO_2) total dose at 10.9 and 5.4 krad(SiO_2)/min is shown in Figure 3.9. The cantilever irradiated at 10.9 krad(SiO_2)/min to 200 krad(SiO_2) had a resonance frequency shift of ~ -2 ppm and continued to decrease for ~2 hours after irradiation before super recovering. The cantilever irradiated at 5.4 krad(SiO_2)/min to 200 krad(SiO_2) had a resonance frequency shift of ~-5ppm and continued to decrease for ~2.5 hours after irradiation before recovering.

At 10.9 krad(SiO_2)/min, resonance frequency shift for the cantilever irradiated to 200 krad(SiO_2) was 87% less than the resonance frequency shift for devices irradiated to 1 Mrad(SiO_2) and the post-irradiation shift for the 200 krad(SiO_2) was 63% less than for 1 Mrad(SiO_2). At 5.4 krad(SiO_2)/min, resonance frequency shift for the cantilever irradiated to 200 krad(SiO_2) was 85% less than the resonance frequency shift for devices irradiated to 1 Mrad(SiO_2) and the post-irradiation shift for the 200 krad(SiO_2) was 39% less than for 1 Mrad(SiO_2).

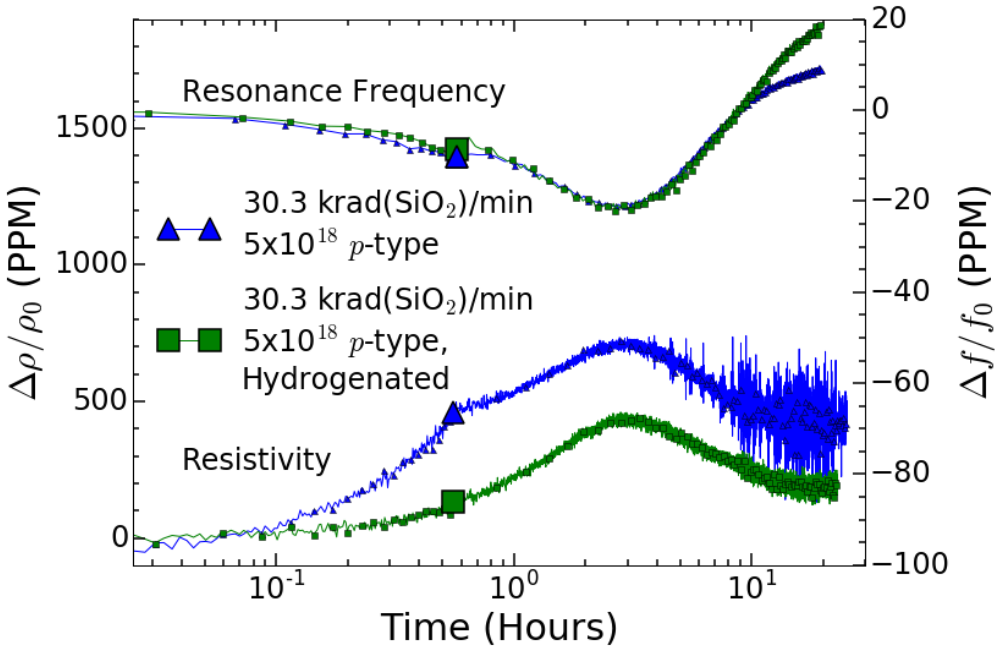

(a)

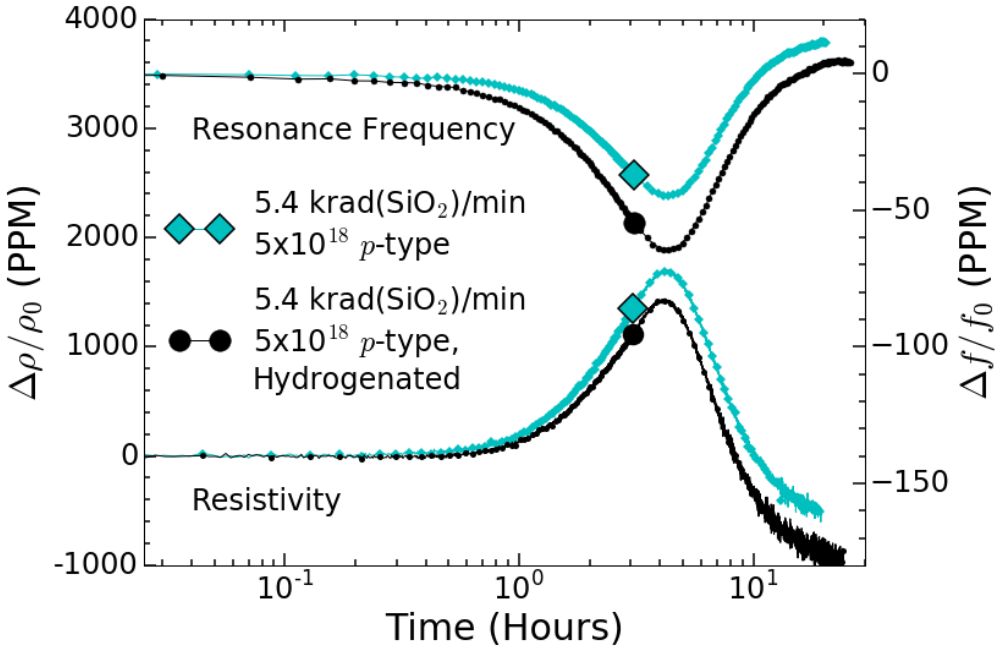

(b)

Figure 3.7: Change in resonance frequency (top) and resistivity (bottom) as a function of time for representative hydrogenated and non-hydrogenated 5×10^{18} cm^{-3} *p*-type cantilevers and resistors irradiated at (a) 30.3 and (b) 5.4 krad(SiO_2)/min. The large markers indicate the time when irradiation ends and annealing begins.

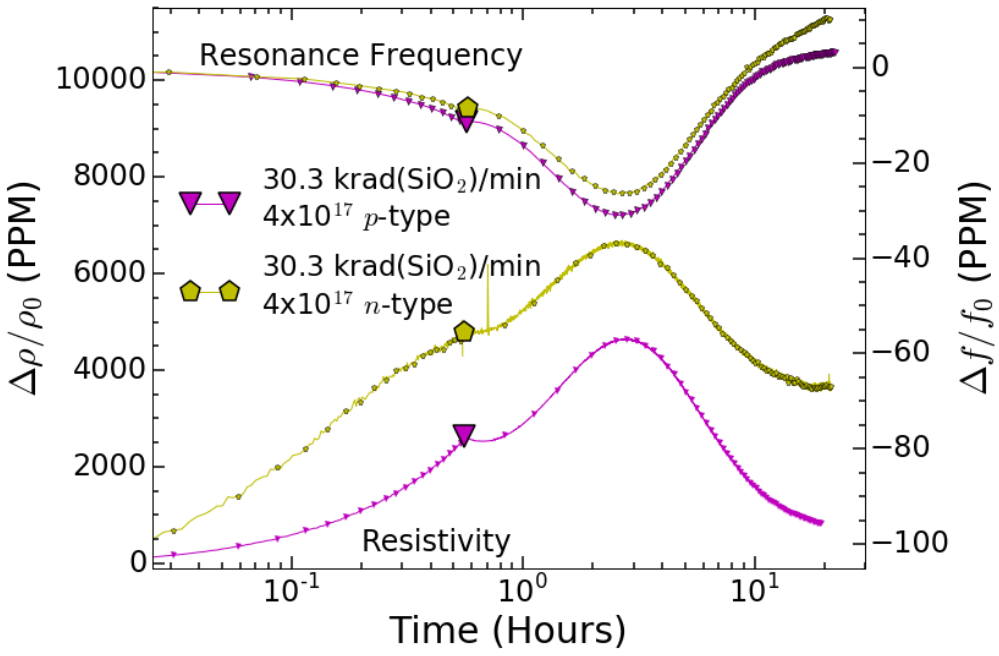

(a)

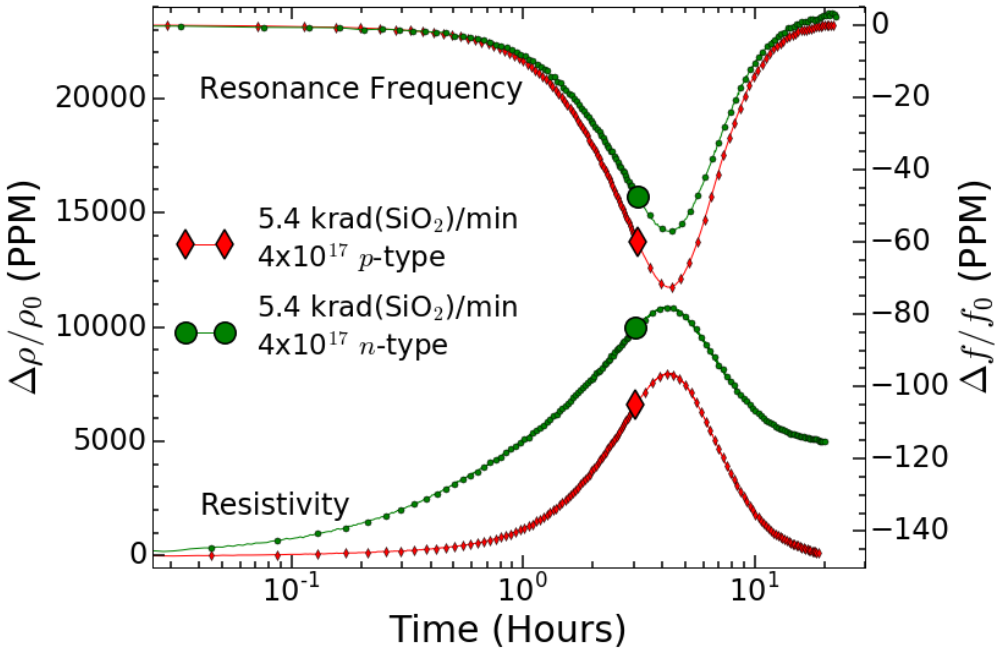

(b)

Figure 3.8: Change in resonance frequency (top) and resistivity (bottom) as a function of time for representative *n*- and *p*-type 4×10^{17} cm^{-3} cantilevers and resistors irradiated at (a) 30.3 and (b) 5.4 krad(SiO_2)/min. The large markers indicate the time when irradiation ends and annealing begins.

Table 3.4: Resistivity Shifts After 1 Mrad(SiO_2) Total Dose

Dose Rate (krad(SiO_2)/min)	Doping (cm^{-3})	Change After Irradiation (ppm)	Maximum Change (ppm)	Difference
30.3	5×10^{18}	400	600	200
5.4	5×10^{18}	1400	1750	350
30.3	5×10^{18} (H)	50	400	350
5.4	5×10^{18} (H)	1100	1400	300
30.3	4×10^{17}	2645	4650	2005
5.4	4×10^{17}	6620	7967	1347
30.3	4×10^{17} (N)	4293	6682	2389
5.4	4×10^{17} (N)	10000	12000	2000

(H) = Hydrogenated, (N) = *n*-type

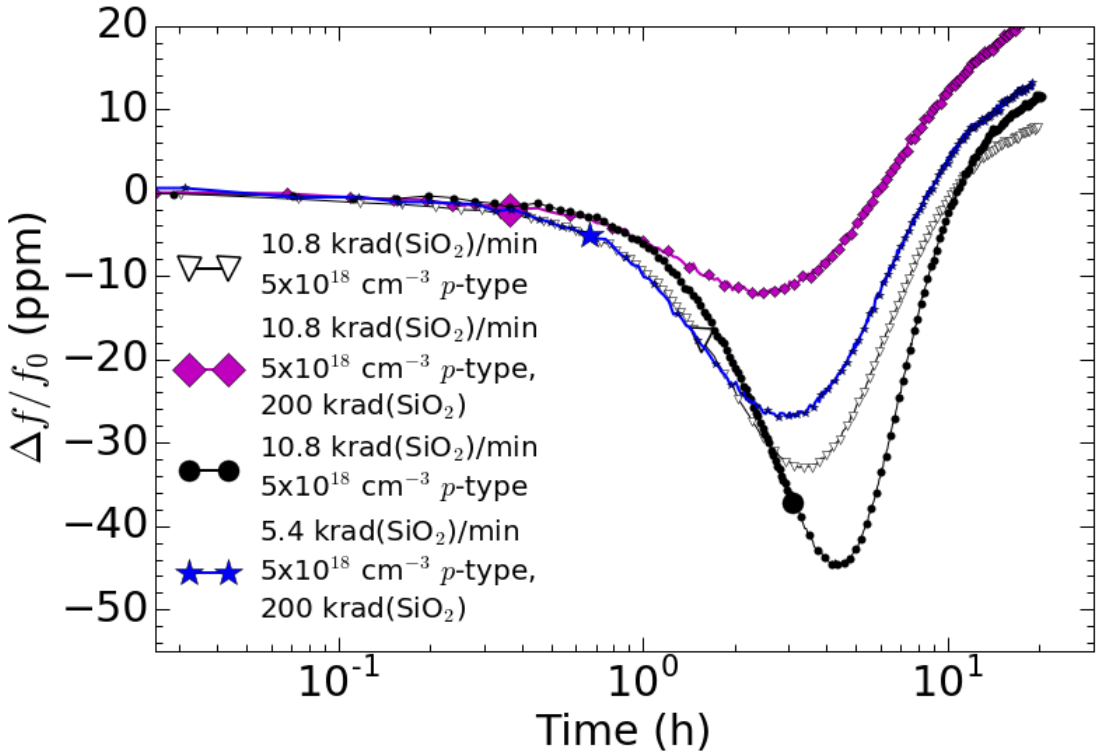

Figure 3.9: Change in resonance frequency as a function of time for representative *p*-type 5×10^{18} cm^{-3} cantilevers irradiated at 10.9 and 5.4 krad(SiO_2)/min to 200 and 1000 krad(SiO_2). The large markers indicate the time when irradiation ends and annealing begins.

CHAPTER 4

DISCUSSION

In general, when a cantilever is irradiated by X-rays, the resonance frequency decreases. Resonance frequency shifts due to irradiation are related to how Young's modulus depends on carrier concentration, how hydrogen in silicon interacts with silicon, boron or phosphorus, and other hydrogen atoms [23], and time-dependent surface charging of the native oxide. Young's modulus depends on the Fermi level, where an increase in carriers causes a decrease in Young's modulus. As Young's modulus decreases, the silicon softens. This suggests that exposure to X-rays causes an increase in carrier concentration in order for Young's modulus to decrease.

The resistivity across the cantilever base increases when exposed to X-rays, most likely due to an increase in ionized and neutral impurity scattering from decreasing mobility due to excess carriers and hydrogen released from boron. The magnitude of these results is dependent on hydrogen content, dose rate, dopant concentration, and dopant type.

Hydrogen Effects Due to X-rays

When silicon is exposed to 10-keV X-rays, electron-hole pairs are created through the photoelectric effect [124] and interact with both silicon, dopant atoms, and hydrogen defects. Dopant-hydrogen complexes are dissociated causing an increase in carrier concentration. The liberated hydrogen also originates from Si-H and other hydrogen complexes [78, 83, 96, 98, 104]. The Fermi level affects whether hydrogen is formed with a positive, neutral, or negative charge state in silicon [78, 79, 80, 81, 96, 97]. Since Young's modulus is defined from the differences between Fermi energies between strained and unstrained silicon, the additional carriers cause

Young's modulus to decrease. This, in turn, causes the resonance frequency to decrease. Due to the resistivity increases seen due to irradiation, it is also likely that the interactions of both charged and neutral hydrogen with the holes cause a decrease in the carrier mobility due to ionized and neutral impurity scattering [45]. Furthermore, it is possible the reduced mobility causes a decrease in *C'*, affecting Young's modulus [72, 77].

Given that electron-hole pair formation requires an average of 3.6 eV, it is reasonable to assume that the required energies between 0.2-2.6 eV for the various hydrogen reactions presented above will be readily available [78, 79, 80, 111, 112]. In all sets of *p*-type samples used in these experiments, boron-hydrogen complexes are dissociated to create ionized boron and either H^+ (2.17) or H^0 and a hole (2.18) [80]. Additionally, these released atoms and carriers can further interact with other atoms and carriers in the silicon lattice to liberate more hydrogen, dissociate more B-H complexes, and liberate more holes [78]. Similarly, in the *n*-type samples, the phosphorus-hydrogen complex can be dissociated as shown in reaction (2.19) [96]. All of these reactions are capable of adding carriers from ionized dopant atoms to the silicon and affecting the Fermi level causing resonance frequency to drop.

The liberation of mobile and charged hydrogen into the cantilevers will affect the elasticity of the silicon. Silicon hydrogenated or implanted with hydrogen in previous experiments have shown decreases in elasticity [95, 116, 117, 119, 120, 121, 141]. While the effects of H-implantation on elasticity in Si are highly localized to the depth the hydrogen is implanted, hydrogenation effects are seen at greater depths within silicon samples [45, 121]. The hydrogenation of cantilevers via steam bath causes Young's modulus to decrease and be reflected in a drop in the resonance frequency of a cantilever beam [121]. Because of the 10-keV X-rays penetrating through the entire 15-μm depth of the devices [145], the cantilevers and resistors in these experiments should have

fairly uniform profiles of liberated hydrogen and dopant atoms during irradiation. The liberated hydrogen, in turn can interact with dopant atoms to cause an increase in carrier concentration, with other hydrogen atoms to dimerize, and with carriers to increase scattering and reduce mobility.

Dose-Rate Effects

The differences in carriers needed to cause the measured changes in resonance frequency highlight the existence of a dose rate effect present in these devices. A comparison of anneal rates following the method presented by Winokur *et al.* [88] confirms that anneal rates are similar across the three dose rates and two total doses. In this case, the shape of the anneal curves is not ideal because the resonance frequencies continue to decline after irradiation instead of immediately recovering. The devices do, however, recover at a similar time, indicating that anneal rates should be similar. The calculated numbers for these calculations are only useful to check for self-consistency.

In order to do these calculations, the recovery is assumed to have occurred at ~12 hours after the start of irradiation, or the point at which the 1 Mrad(SiO_2) anneal curves in Figure 4.1 cross. The calculated slopes are listed in Table 4.1 for representative devices irradiated at the three dose rates and two total doses. Additionally, the ratio of anneal slopes between the different total doses is presented. Figure 4.1 shows a comparison of resonance frequency response for the representative devices irradiated at the three dose rates as a function of time. The overlaid dashed red lines are fits between the resonance frequency after irradiation and resonance frequency at the designated recovery time. When the anneal slope is normalized to the corresponding post-radiation resonance frequency shift, the anneal rate is given. Ideally, the anneal rate should be the same for all three

dose rates. Table 4.1 shows that the anneal rates between all three devices irradiated to 1 Mrad(SiO_2) is ~-0.12 with a standard deviation of 0.01.

A comparison of the devices irradiated to 200 and 1000 krad(SiO_2) at the middle and low dose rates highlights the pitfalls of making these calculations for these devices. The recovery or super recovery of resonance frequencies is inconsistent from device to device. For example, the anneal

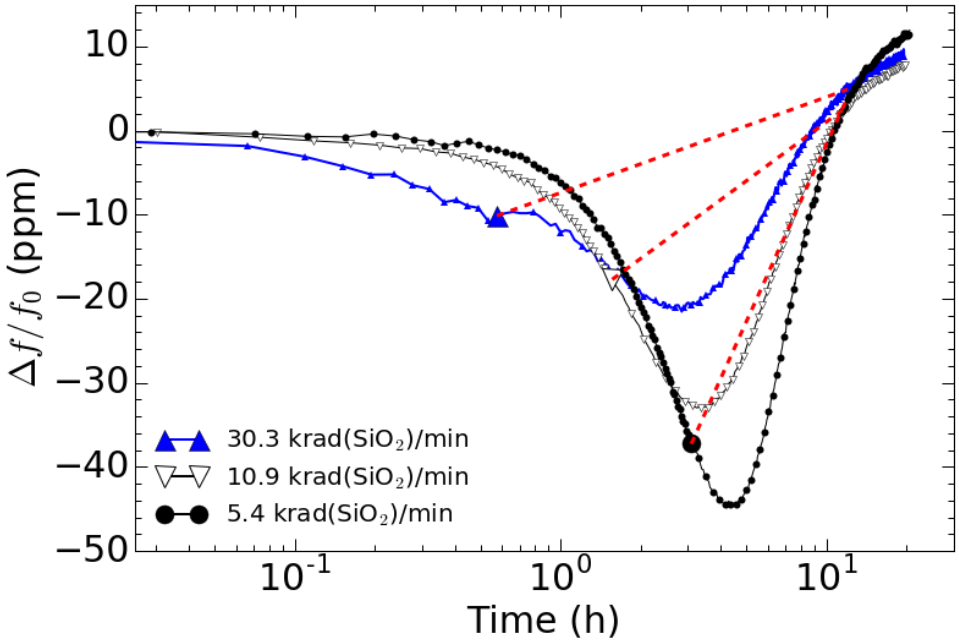

Figure 4.1: Change in resonance frequency as a function of time for representative *p*-type 5 × 10^{18} cm^{-3} cantilevers irradiated at 30.3, 10.9, and 5.4 krad(SiO_2)/min to 1000 krad(SiO_2). The large markers indicate the time when irradiation ends and annealing begins.

Table 4.1: Anneal Rates and Slopes

Dose Rate (krad(SiO_2)/min)	200 krad(SiO_2) slope (ppm/h)	1 Mrad(SiO_2) slope (ppm/h)	Anneal Rate	Ratio
30.3	--	1.31	-0.13	--
10.9	--	1.97	-0.11	
10.9	1.47	--	-0.73	1.34
5.4	--	4.63	-0.12	
5.4	1.16	--	-0.15	4.0

rate for the device irradiated to 200 krad(SiO_2) at 10.9 krad(SiO_2)/min is ~5x greater due to the larger super recovery it shows (shown in Figure 3.9). The device irradiated to 200 krad(SiO_2) at 5.4 krad(SiO_2)/min shows results similar to the 1 Mrad(SiO_2) devices. The same uncertainty applies when comparing ratio of slopes for the 200 and 1000 krad(SiO_2) devices. In an ideal scenario, annealing slopes are proportional to the total dose received. The ratio for the 10.9 krad(SiO_2)/min devices is 1.33, which is far off and again likely due to the lower dosed sample super recovering. The ratio of the 5.4 krad(SiO_2)/min devices is 4.0, which is closer to the ratio of total doses received, which is 5.

In general, it can be assumed that at the high dose rate, the liberation of hydrogen and other species is higher than at the low dose rate. When the transporting hydrogen concentration is relatively high, as is the case for high dose-rate irradiations in Figs. 3.4 – 3.9, transporting hydrogen atoms in the Si (expected to be dominant, owing to the relatively large volume) and/or surface oxide (expected to be secondary, owing to the relatively small volume) can dimerize to form H_2 with higher probability than when the transporting hydrogen concentration is lower for the low dose-rate irradiations [43]. The smaller fraction of hydrogen in atomic form at the high dose rate reduces the amount available to potentially depassivate dopant atoms. Hydrogenated devices show similar resonance frequency shifts to untreated devices at higher rates (Figure 3.4) because the extra hydrogen simply forms more H_2 that does not react with dopants. At the low dose-rate, on the other hand, more hydrogen is available to depassivate dopants, leading to higher carrier concentrations and larger resonance frequency shifts. At the high dose rate, the larger production of hydrogen will lead to a higher generation of both ionized and neutral hydrogen than at the low dose rate. The mobility will decrease due to the scattering from these species causing the resistivity to rise faster at the high dose rate than the low dose rate.

The resonance frequency shift at the high dose rate compares favorably with the shifts seen when cantilevers with 5×10^{18} cm^{-3} boron doping were irradiated with 2-MeV protons at a flux of 10^{10} ions/cm^2. This gives a dose rate of ~ 600 krad(SiO_2)/min. After exposure to 1×10^{12} cm^{-2} protons, the cantilevers were exposed to a total dose of ~ 1 krad(SiO_2) and showed a resonance frequency decrease of ~ -10 ppm, similar to the shift of -12 ppm seen at the high dose rate for devices with the same doping [30]. This suggests the upper bound of the radiation effect is close to 30.3 krad(SiO_2)/min. The small difference in response may be due to displacement damage from the protons counteracting the effects of TID.

While the native oxide should be relatively thin (2 – 10 nm), it is also possible that X-rays are creating charge in the native oxide [125]. The buildup of surface charges on the surface of the native oxide is also potentially dose-rate sensitive due to space charge effects that can enhance the neutralization of trapped charge at the high dose rate [91, 126, 133, 135]. Additionally, the transporting carriers can lead to surface charging of the native oxide [125, 126] as well as the release of hydrogen in the Si and native oxide [43, 86, 93, 98, 111, 127, 128].

The presence of charge in the oxide means that it would be possible to have a small depletion region at the surface of the device. Recall that under depletion, MOS capacitors exhibited B-H passivation when there was 0 V bias across the SiO_2/Si interface [137]. In the case of the high dose rate, this depletion region would be smaller, allowing for a greater volume of hydrogen-dopant dissociation to occur in the bulk of the device. At the lower dose rate, the charge in the oxide will be greater, allowing for a deeper depletion region, slower carrier transport, and more dopant deactivation or neutralization near the surface. This leads to a smaller volume of hydrogen that can be released in the bulk of the device, leading to slower changes.

A depletion region at the surface can also explain an increase in resistivity. A previous study of the effects of γ-rays on MEMS accelerometers attributed a rise in resistivity to a depletion region at the surface that reduces current flow through the piezoresistor. The piezoresistor was 25 × 4.2 × 0.6 μm and the oxide was estimated to be 50 nm. Devices where irradiated at a dose rate of 2.3 to 2.6 krad(Si)/min up to 750 krad(Si). As the total dose increased, the depletion region increased, limiting the current that could flow through the resistor. This was reflected by an increase in output voltage when the sensor was stressed [34]. It is plausible that a mechanism similar to this could be partially responsible for the resistivity increases seen in this work. However, the relative thinness of the native oxide compared to the larger bulk of the device suggest this should have much less effect for these devices. The aforementioned experiment did not test for dose rate effects, but it is reasonable to expect that this effect would be dose-rate sensitive given the nature of the ELDRS mechanism.

Changes in Carrier Concentrations

Carrier concentrations influence the value of the three elastic constants in silicon. Keyes' deformation potential theory allows the number of carriers required to cause the changes seen resonance frequency to be calculated. The continuing resonance frequency response over the course of hours indicates that the main cause of the carrier concentration increase is most likely from ionized impurities. This aligns well with time scales from ELDRS research that are attributed to continuing hydrogen transport and interactions [43]. Electron and hole lifetimes are in the range of milliseconds or less. It is unlikely that electrons or holes are the main cause of the carrier concentration increase [49].

While all three elastic constants most likely change as device is exposed to X-rays, for mathematical simplicity, the assumption is made that c_{11} and c_{12} remain constant and all changes are reflected in c_{44}. This allows equation (1.5) to be rearranged:

$$c_{44} = \frac{Y_{110} - (c_{11}+2c_{12})(c_{11}-c_{12})}{2c_{11}Y_{110} - 4(c_{11}+2c_{12})(c_{11}-c_{12})} \tag{4.1}$$

where Y_{110} is calculated from a resonance frequency by rearranging Equation (1.6):

$$Y_{110} = {f_n}^2 \frac{4\pi L^4}{\beta_n^4} \frac{\rho h b}{I}. \tag{4.2}$$

Equations (2.8) and (2.9) for *n*- and *p*-type samples, respectively, are rearranged:

$$n = \left(\frac{3\Delta c_{44} h^2}{4\left(\frac{4\pi}{3}\right)^{2/3} \mathrm{m}_n^* \Xi^2} \right)^3 \tag{4.3}$$

$$p = \left(\frac{5\Delta c_{44} h^2}{\left(\frac{8\pi}{3}\right)^{2/3} \mathrm{m}_p^* \Xi^2} \right)^3 \tag{4.4}$$

to calculate the change in carrier concentration.

The changes in carrier concentration for a representative device of each doping type are shown for the high and low dose rates in Figure 4.2. Depending on the deformation potential used in Equations (4.3) and (4.4), there can be a ~2 order of magnitude change between the calculated carrier concentrations. As long as the same deformation potential is used for each calculation, a comparison can be made between results for each device. The values in Figure 4.2 are calculated using a deformation potential of 8.6 eV, which is an average of the values found in literature. For these calculations, empirical values of 165.6 GPa, 63.9 GPa, and 79.56 GPa for c_{11}, c_{12}, and c_{44}, respectively, were used for un-doped silicon [19, 26, 67, 68].

First, an initial value of c_{44} is calculated by adding the empirical value of c_{44} to Δc_{44} using the initial doping using Equation (2.11). Then the value of Young's modulus is calculated using

Equation (1.5). Using the initial measured resonance frequency, the width of the cantilever beam is estimated to account for width lost in the fabrication process. A second value of Young's modulus is calculated from a second resonance frequency (irradiated or post-rad) from Equation (4.2) using the estimated beam width. A second value for c_{44} is calculated from (4.1) and then compared to the empirical value of c_{44} to find Δc_{44}. Finally, the value of Δc_{44} for the second resonance frequency is used to estimate the number of liberated carriers.

Figure 4.2 shows the results of these calculations for in situ and post-irradiation for representative devices. Figure 4.2(a) shows the change in carrier concentrations in the 5×10^{18} cm^{-3} *p*-type and hydrogenated *p*-type devices. While the devices are being irradiated, the rate of change in carrier concentration at the high dose rate is higher than the rate of change in carrier concentration at the low dose rate. The increase in carrier concentration at the low dose rate is slower at first, but continues to build beyond the devices irradiated at the high dose rate.

Figure 4.2(b) shows the change in carrier concentration in the 4×10^{17} cm^{-3} *n*- and *p*-type cantilevers. The rate of change in carrier concentration appears higher at the high dose rate. With the same initial dopant concentrations, there is ~1 order of magnitude more increase in carrier concentration in the lower-doped *p*-type devices than the *n*-type devices. Depending on the deformation potential used, the changes in carrier concentration will vary between 4×10^{17} cm^{-3} with a deformation potential of 11.8 eV to 3×10^{19} cm^{-3} with a deformation potential of 2.1 eV for a 5×10^{18} cm^{-3} hydrogenated devices.

In general, for each set of devices irradiated at the high and low dose rate, the changes in carrier concentration show similar shapes to the changes in resonance frequency. The hydrogenated and lower-doped *p*-type cantilevers show similar changes in carrier concentration and similar shifts in resonance frequency. However, the changes in carrier concentration for the *n*-type devices are ~1

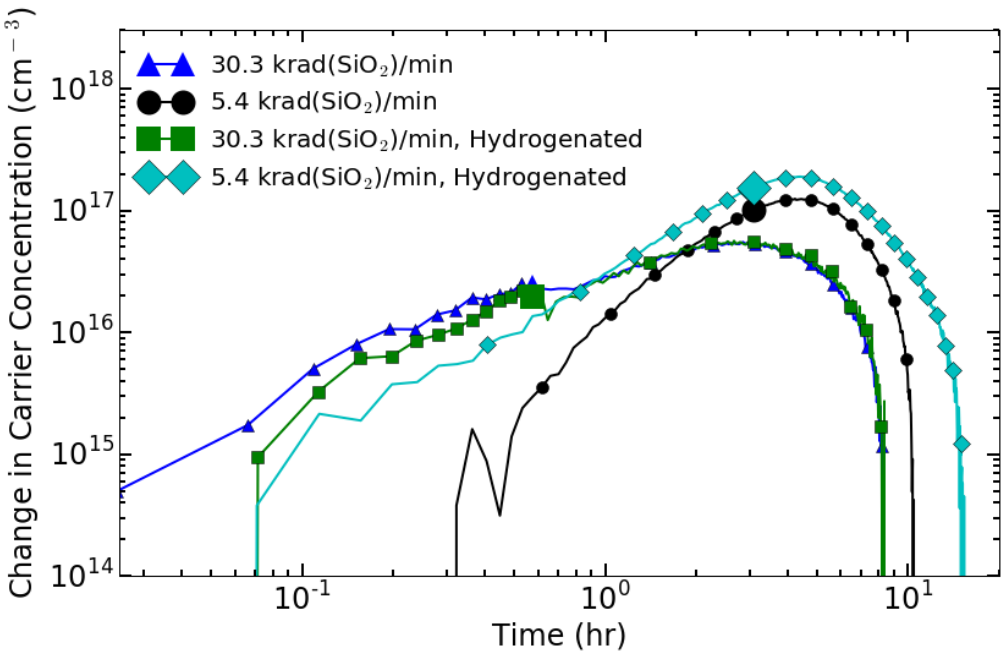

(a)

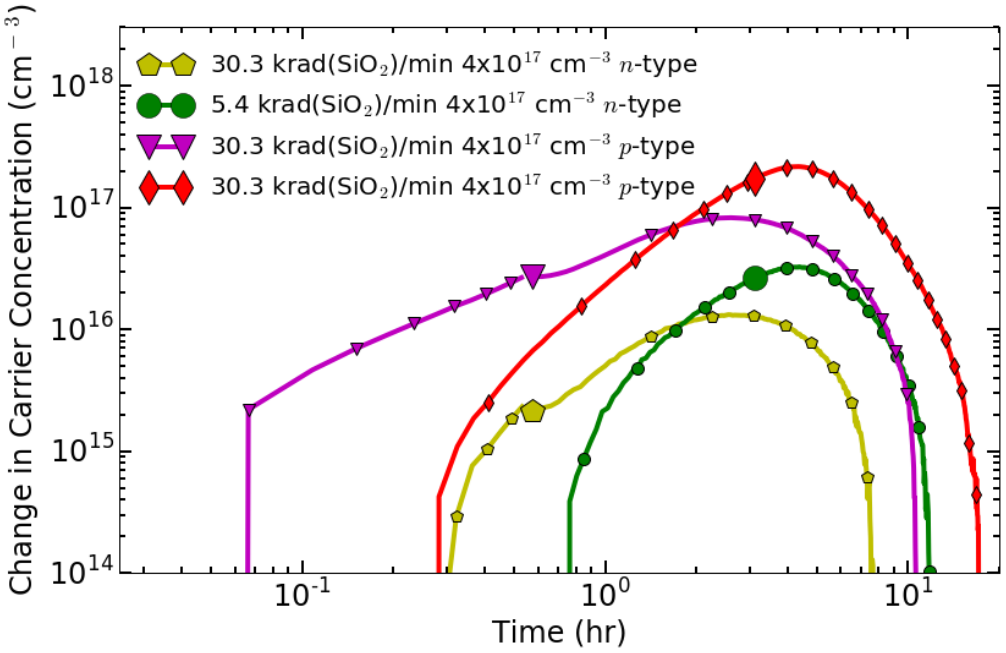

(b)

Figure 4.2: Changes in carrier concentration as a function of dose for (a) non-hydrogenated and hydrogenated 5×10^{18} cm^{-3} *p*-type and (b) 4×10^{17} cm^{-3} *n*- and *p*-type devices irradiated at 5.4 and 30.3 krad(SiO_2)/min calculated from equations 4.3 and 4.4. The changes are most likely differences in ionized impurity concentrations.

order of magnitude lower than the hydrogenated and lower-doped *p*-type devices, yet show the same resonance frequency shifts at both dose rates.

Changes in Resistivity and Mobility and Resistivity Dose Rate Effects

While the resonance frequency decreases due to irradiation, the resistivity of the sample increases as a function of irradiation. The reversal of both resonance frequency and resistivity at the same time in post-irradiation measurements, as shown in Figures 3.5 and 3.6, emphasizes the key point that these mechanisms are closely related. While the resistivity rises during irradiation, the magnitude of these rises varies greatly compared to the changes in resonance frequency. The increase in resistivity can be explained by an increase in impurity scattering in the silicon. In measurements of mobility in hydrogenated silicon, increases in resistivity are typically attributed to ionized impurity scattering [45, 94, 109]. While this accounts for ionized impurities, neutral atomic and molecular hydrogen in the silicon are also present acting as neutral impurities.

In the 5×10^{18} cm^{-3} *p*-type devices, at the high dose rate, a greater amount of hydrogen is released as a function of time. This leads to more hydrogen-hydrogen interactions creating H_2 and more neutral impurities resulting in a greater influence of neutral impurity scattering. At the lower dose rate, the transporting hydrogen content is lower, allowing for more interactions with dopants like boron-hydrogen dissociation. This leads to more H^+ and holes and a greater influence from ionized impurity trapping. Over time, the number of ionized carriers builds up and affects the resistivity and resonance frequency more than at the higher dose rate. This mechanism holds true for all devices, though the magnitude of the effect varies, as will be explained below.

In the hydrogenated samples, dopants have previously been passivated, leading to a smaller change in resistivity, but a greater change in Fermi level. The extra passivated dopants allow for

more B-H dissociation and more H^+ to be released. There will also be more dimerization to form H_2. However, the number of carriers excited when the hydrogenated samples are exposed to X-rays may become high enough to counteract the effects of ionized and neutral impurity scattering causing the resistivity rise to be minimal.

For the lower doped 4×10^{17} cm^{-3} *n*- and *p*-type samples, the reason for the greater rise in resistivity is because there are fewer initial carriers. The plot of the mobility as a function of total impurity concentration (Figure 2.1) shows there is a greater decrease in mobility with a small increment of impurities for a 4×10^{17} cm^{-3} *p*-type resistor than a 5×10^{18} cm^{-3} *p*-type resistor. There is an even larger decrease in mobility for an *n*-type resistor with 4×10^{17} cm^{-3} impurities, explaining why the *n*-type resistivity had the greatest increase of all samples tested. These changes are similar to previous results found in diodes where the *n*-type material shows degradation in current as a function of irradiation [138].

Post-Irradiation Behavior

The ongoing transport of hydrogen within the Si may also explain the continuing decline in resonance frequency immediately and continuing increase in resistivity after irradiation. During the first phase of this process, the depassivation of dopant-H complexes and other hydrogen mechanisms in the system evidently dominate the response, increasing the carrier density further. Depending on the dose rate, after 2 to 2.5 hours, the resonance frequency and resistivities begin to recover to their pre-irradiation values. As the concentration of charged hydrogen dissipates, dopant-H complexes are re-passivated, the Fermi level returns to its original level, and the devices return to their equilibrium condition. This causes the resonance frequency to rise back to its initial level, the mobility of carriers in Si to increase, and the resistivity to decline.

When the devices return to pre-irradiation values, the surface charge has been neutralized and passivation reactions have restored the concentrations of active dopants and passivated dopant-H complexes to values closer to pre-irradiation. The variations in post-irradiation values in Figures 3.5 and 3.6 suggest the return to near-equilibrium is approximate, which is not surprising, since the final densities of H and dopant-H complexes likely differ from initial values. The resistivities of the resistors irradiated at the high dose rate may not fully recover due to the large amounts of H_2 created. This may leave behind an increased contribution to the mobility from neutral impurity scattering.

Figure 4.3 compares the evolution of the resonance frequency with time for a representative 5×10^{18} cm^{-3} device (not exposed to hydrogen) as it is pumped down in the vacuum chamber over 40 h. The red line shows the un-irradiated pump-down curve. The dotted blue line shows the same device in a second run, now irradiated at 5.4 krad(SiO_2)/min. The first marker indicates where radiation begins and the second marker indicates where radiation ends. This figure emphasizes that the primary effect of irradiation is to decrease the resonance frequency significantly from the level to which it otherwise would have increased as a result of continued outgassing in the low-pressure environment. The degree to which the resonance frequency decreases from this level is strongly influenced by the dose and dose rate of the irradiation, as well as (for lower-rate irradiation) whether the device has been hydrogenated.

The length of time for resonance frequencies and resistivities take for recover after irradiation is notable in that it further confirms the changes are due to exposure to 10-keV X-rays. If the effect were due to temperature, the device would recover much more quickly. A conclusion from Hjalmarson, *et al.* is that critical dose rates for the types of competing effects discussed may have delayed reactions lasting as long as 10^6 s [43, 90, 128]. These numbers compare favorably to the

results presented in this work, given that continuing shifts in resonance frequency and resistivity last ~10^5 s after irradiation.

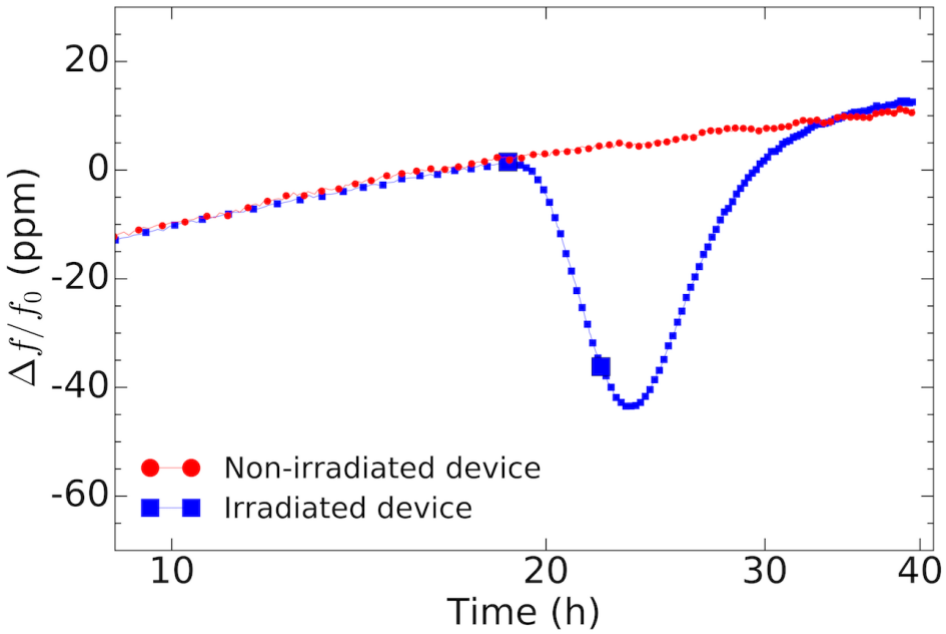

Figure 4.3: Measured resonance peak as a function of time in vacuum for a representative, control device that was unirradiated for 40 h and again for the same device irradiated at 5.4 krad(SiO_2)/min, showing that the primary effect of irradiation is to decrease the resonance frequency significantly from the level to which it otherwise would have increased as a result of the continuing pump-down process. The first large marker indicates where radiation begins and the second large marker indicated where radiation ends. The system pressure changes by less than 2×10^{-5} mbar during the ~30 h interval shown, so the continuing decrease in resonance frequency is most likely due to outgassing.

CHAPTER 5

CONCLUSIONS

As MEMS continue to be considered for applications in space environments, it is important to understand how they respond to radiation. In this research, T-shape, asymmetric, piezoresistive micromachined cantilevers and resistors are irradiated with 10-keV X-rays at 30.3, 10.9, and 5.4 krad(SiO_2)/min. As the cantilevers are exposed to 1 Mrad(SiO_2), mechanisms involving hydrogen interactions with dopant-silicon complexes and surface charge trapping cause resonance frequency and shear elastic constants to decrease. The elastic constants are influenced by the total carrier concentration of the sample with increasing carrier concentrations decreasing elasticity. The resistivity across the base of the resonating cantilevers was measured as a function of total dose to clarify the mechanisms causing resonance frequency decrease. Resistivity increases with total dose due to increases in scattering causing a decrease in carrier mobility. Both resonance frequency and resistivity continue to shift after irradiation is complete before recovering to pre-irradiation values. The reversal of both resonance frequency and resistivity at the same time emphasizes that the mechanisms causing these effects are closely related. The resonance frequency for all dose rates and total dose recover to pre-irradiation values at similar times indicating a true dose-rate effect.

The resonance frequency of the cantilevers at 1 Mrad(SiO_2) total dose decreased more at lower dose rates than at higher dose rates. At the higher dose rate, all resonance frequency decreases were similar. At the lower dose rate, the magnitude of resonance frequency shifts depend on carrier concentration and hydrogen content where an order of magnitude less doping has a similar response as increased hydrogen content. The dose-rate dependence of the resonance frequency

shifts is due to space charge effects that alter both the amount of surface charging and the available concentrations of transporting hydrogen. The relative concentrations of hydrogen, unpassivated dopants, and passivated dopant-H complexes play key roles in these processes.

The resistivity at 1 Mrad(SiO_2) total dose increases more at lower dose rates than at higher dose rates. The increase in resistivity depends on dopant concentration, dopant type, and hydrogen content. Resistivity increases are greatest for the *n*-type resistors, which have lower doping. The *p*-type resistors with lower doping show less increases in resistivity than the *n*-type resistors, but more increases in resistivity than the *p*-type resistors with higher doping. The hydrogenated resistors, with higher doping, show less resistivity increases than non-hydrogenated resistors with the same doping. The increases in resistivity are caused by increased ionized and neutral impurity scattering causing a decrease in mobility. As dopant-H complexes are dissociated to form ionized H, ionized impurity scattering is increased. Increases in neutral atomic H and molecular H_2 cause an increase in neutral impurity scattering. At higher dose rates, neutral impurity scattering is more influential due to a high transporting H concentration creating more H_2. Lower dose rates allow more dopant-H dissociation leading to a greater influence on the mobility from ionized impurity scattering.

The resulting sensitivities of the resonance frequency shifts to dose rate and to hydrogen content are important factors to consider in device characterization and qualification testing for use of these devices in space radiation environments. The effects of low dose rate on the shear elastic constants of silicon show that low-dose-rate testing must be considered for all types of MEMS devices. This research clearly shows that resonance frequency will decrease more at lower dose rates. Exposure of MEMS logic to neutrons has already shown threshold voltages will shift when exposed to radiation [11]. While attractive for their promise of zero leakage current, it is possible

that volatile memory devices would see negative threshold voltage shifts and eventually failure as devices are exposed to high total doses and elasticity decreases. Non-volatile memory shows the most potential in space radiation environments as they are static in nature and do not rely on elasticity to switch on and off [3].

The devices used in this research are relatively large compared to modern CMOS technology. As MEMS are designed for space applications, they will inevitably become smaller so that they are more easily integrated with current technology. However, thinner devices have decreasing elasticity, especially below 100 nm thickness [19, 41]. These devices are probably more susceptible to TID effects as the electronic effects should have greater impact on the elasticity. Since there are both surface and bulk effects that are occurring in MEMS, it is likely that changing surface to volume ratios will play a role, as well.

The effects of ionizing radiation on elasticity may be directionally dependent. MEMS designers are already aware of directional dependencies for practical applications related to crystal orientations [58]. However, more research needs to be done to characterize the radiation response of devices that have different crystal orientations. When this is done, it may be possible to optimize the best practical designs with a minimal radiation response in certain orientations. Additionally, as more materials are considered and researched for traditional semiconductor devices, research of alternative material systems for MEMS will become more common. Each material system has different mechanical properties and will have different radiation responses.

For silicon MEMS, future work will be required to quantify these effects in ways involving lower dose rate irradiation and quantitative modeling and simulation, similar to those developed for ELDRS [130, 136] after many years of research [92, 123, 135]. Until such understanding is

developed, detailed testing of these types of MEMS devices will need to consider dose rate and hydrogen effects in device characterization and qualification.

REFERENCES

[1] J. T. M. van Beek and R. Puers, "A review of MEMS oscillators for frequency reference and timing applications," *J. Micromechanics Microengineering,* vol. 22, no. 1, p. 13001, 2012.

[2] H. R. Shea, "Effects of radiation on MEMS," *Proc. of SPIE,* pp. 79280E-79280E-13, 2011.

[3] T. He, F. Zhang, S. Bhunia and P. X. L. Feng, "Silicon carbide (SiC) nanelectromechanical antifuse for ultralow-power one-time-programmable (OTP) FPGA interconnects," *IEEE J. Electron Devices Soc.,* vol. 3, no. 4, pp. 323-335, 2015.

[4] H. Lee, A. Partridge and F. Assaderaghi, "Low jitter and temperature stable MEMS oscillators," *2012 IEEE Interational Frequency Control Symposium Proceedings,* pp. 1-5, 2012.

[5] K. M. Walsh, H. T. Henderson and G. N. D. Brabander, "A fully-packaged silicon micromachined piezoresistive accelerometer," *Proc. of IEEE Southeastcon '92,* vol. 2, pp. 753-756, 1992.

[6] P. S. Waggoner and H. G. Craighead, "Micro- and nanomechanical sensors for environmental, chemical, and biological detection," *Lab. Chip,* vol. 7, no. 10, pp. 1238-1255, Sep. 2007.

[7] H. Takahasi, N. M. Dung, K. Matsumoto and I. Shimoyama, "Differential pressure sensor using a piezoresistive cantilever," *J. Micromechanics Microengineering,* vol. 22, no. 5, p. 55015, 2012.

[8] G. Binnig, C. F. Quate and C. Gerber, "Atomic force microscope," *Phys. Rev. Lett.,* vol. 56, no. 9, pp. 930-933, 1986.

[9] G. M. Rebeiz and J. B. Muldavin, "RF MEMS switches and switch circuits," *IEEE Microwave Mag.,* vol. 2, no. 4, pp. 59-71, 2001.

[10] J. Millman and A. Grabel, Microelectronics, New York: McGraw-Hill, 1998.

[11] F. K. Chowdhury, D. Saab and M. Tabib-Azar, "Single-device “XOR” and “AND” gates for high speed, very low power LSI mechanical processors," *Sensors and Actuators A: Physical,* vol. 188, pp. 481-488, 2012.

[12] B. W. Soon, E. J. Ng, Y. Qian, N. Singh, M. J. Tsai and C. Lee, "A bi-stable nanoelectromechanical non-volatile memory based on van der Waals force," *Apl. Phys. Lett.,* vol. 103, p. 053122, 2013.

[13] P. D. Shuvra, S. McNamara, J.-T. Lin, B. W. Alphenaar, K. M. Walsh and J. L. Davidson, "Axial asymmetry for improved sensitivity in MEMS piezoresistors," *J. Micromechanics Microengineering,* vol. 26, no. 9, p. 95014, 2016.

[14] A. A. Barlian, W.-T. Park, J. R. Mallon, A. J. Rastegar and B. L. Pruitt, "Review: semiconductor piezoresistance for microsystems," *Proc. IEEE Inst. Electr. Electron. Eng.,* vol. 97, no. 3, pp. 513-552, 2009.

[15] Y. Kanda, "Piezoresistance effect of silicon," *Sens. Actuators Phys.,* vol. 28, no. 2, pp. 83-91, 1991.

[16] R. W. Keyes, "Electronic effects in the elastic properties of semiconductors," *Solid State Phys.,* vol. 20, pp. 37-90, 1968.

[17] W. C. Young and R. Budynas, Roark's formulas for stress and strain, New York; London: McGraw-Hill, 2002.

[18] C. S. Smith, "Piezoresistance effect in germanium and silicon," *Phys. Rev.,* vol. 94, no. 1, pp. 42-49, 1954.

[19] M. A. Hopcroft, W. D. Nix and T. W. Kenny, "What's the Young's modulus of silicon?," *J. Microelectromechanical Syst.,* vol. 19, no. 2, pp. 229-238, 2010.

[20] L. J. Walpole, "The shear elastic moduli of a cubic crystal," *J. Phys. D: Appl. Phys.,* vol. 19, no. 3, pp. 457-462, 1985.

[21] W. Thomson, "XXI. Elements of a mathematical theory of elasticity," *Phil. Trans. R. Soc. Lond.,* vol. 146, pp. 481-498, 1856.

[22] J. F. Nye, Physical properties of crystals, Oxford: Clarendon Press, 1957.

[23] H. Gong, W. Liao, E. X. Zhang, A. L. Sternberg, M. W. McCurdy, J. L. Davidson, R. A. Reed, D. M. Fleetwood, R. D. Schrimpf, P. D. Shuvra, S. McNamara, K. M. Walsh, B. W. Alphenaar and M. L. Alles, "Total-ionizing-dose effects in piezoresistive micromachined cantilevers," *IEEE Trans. Nucl. Sci.,* vol. 64, no. 1, pp. 263-268, 2017.

[24] N. Ono, K. Kitamura, K. Nakajima and Y. Shimanuki, "Measurement of Young's modulus of silicon single crystal at high temperature and its dependency on boron concentration using the flexural vibration method," *Jpn. J. Appl. Phys.,* vol. 39, no. 2R, p. 368, 2000.

[25] J. Richter, J. Pederson, M. Brandbyge, E. V. Thomsen and O. Hansen, "Piezoresistance in p-type silicon revisited," *J. Appl. Phys.,* vol. 104, no. 2, p. 023715, 2008.

[26] P. Csavinszky and N. G. Einspruch, "Effect of doping on the elastic constants of silicon," *Phys. Rev.,* vol. 132, no. 6, pp. 2434-2440, 1963.

[27] L. Meirovitch, Elements of vibration analysis, 2nd Ed., New York: McGraw-Hill, 1986, p. 212.

[28] C. N. Arutt, M. L. Alles, W. Liao, H. Gong, J. L. Davidson, R. D. Schrimpf, R. A. Reed, R. A. Weller, K. Bolotin, R. Nicholl, T. T. Pham, A. Zettl, D. Qingyang, J. Hu, M. Li, B. W. Alphenaar, J.-T. Lin, P. Deb Shurva, S. McNamara, K. M. Walsh, P. X.-L. Feng, L. Hutin, T. Ernst, B. D. Homeijer, R. G. Polcawich, R. M. Proie, J. L. Jones, E. R. Glaser, C. D. Cress and N. Bassiri-Gharb, "The study of radiation effects in emerging micro and nano electro mechanical systems (M and NEMs)," Semicond. Sci. Technol., vol. 32, no. 1, p. 13005, 2017.

[29] D. G. Marinaro, P. McMahon and A. Wilson, "Proton radiation effects on MEMS silicon strain gauges," *IEEE Trans. Nucl. Sci.,* vol. 55, no. 3, pp. 1714-1718, 2008.

[30] H. Gong, W. Liao, E. X. Zhang, A. L. Sternberg, M. W. McCurdy, J. L. Davidson, R. A. Reed, D. M. Fleetwood, R. D. Schrimpf, P. D. Shuvra, J.-T. Lin, S. McNamara, K. M. Walsh, B. W. Alphenaar and M. L. Alles, "Proton-induced displacement damage and total-ionizing-dose effects on silicon-based MEMS resonators," *IEEE Trans. Nucl. Sci.,* vol. 65, no. 1, pp. 34-38, 2018.

[31] J. Gomes and H. R. Shea, "Displacement damage effects in silicon MEMS at high proton doses," *Proc. SPIE 7928,* p. 79280G, 2011.

[32] H. R. Shea, "Radiation sensitivity of microelectromechanical system devices," *J. Micro/Nanolithography, MEMS, and MOEMS,* vol. 8, no. 3, p. 031303, 2009.

[33] C. I. Lee, A. H. Johnston, W. C. Tang, C. E. Barnes and J. Lyke, "Total dose effects on microelectromechanical systems (MEMS): accelerometers," *IEEE Trans. Nucl. Sci.,* vol. 43, no. 6, pp. 3127-3132, 1996.

[34] K. E. Holbert, J. A. Nessel, S. S. McCready, A. S. Heger and T. H. Harlow, "Response of piezoresistive MEMS accelerometers and pressure transducers to high gamma dose," *IEEE Trans. Nucl. Sci.,* vol. 50, no. 6, pp. 1852-1859, 2003.

[35] O. Coumar, P. Poirot, R. Gaillard, E. Miller, N. Buard and L. Marchand, "Total dose effects and SEE screening on MEMS COTS accelerometers," *IEEE REDW,* pp. 125-129, 2004.

[36] L. P. Schanwald, J. R. Schwank, J. J. Sniegowski, D. S. Walsh, N. F. Smith, K. A. Peterson, M. R. Shaneyfelt, P. S. Winokur, J. H. Smith and B. L. Doyle, "Radiation effects on surface micromachined comb drives and microengines," *IEEE Trans. Nucl. Sci.,* vol. 45, no. 6, pp. 2789-2798, 1998.

[37] S. S. McClure, L. D. Edmonds, R. Mihailovich, A. H. Johnston, P. Alonzo, J. DeNatale, J. Lehman and C. Yui, "Radiation effects in micro-electromechanical systems (MEMS): RF relays," *IEEE Trans. Nucl. Sci.,* vol. 49, no. 6, pp. 3197-3202, 2002.

[38] S. S. McCready, T. H. Harlow, A. S. Heger and K. E. Holbert, "Piezoresistive micromechanical transducer operation in a pulsed neutron and gamma ray environment," *IEEE Rad. Effects Data Workshop, Phoenix, AZ,* p. 181–186, 2002.

[39] V. Belwanshi, S. Philip and A. Topkar, "Experimental study of gamma radiation induced degradation of a piezoresistive pressure sensor," *Microsyst. Technol.*, pp. 1-7, 2018.

[40] H. Sadeghian, C. K. Yang, J. F. L. Goosen, E. v. d. Drift, A. Bossche, P. J. French and F. v. Keulen, "Characterizing size-dependent effective elastic modulus of silicon nanocantilevers using electrostatic pull-in instability," *Appl. Phys. Lett.*, vol. 94, no. 22, p. 221903, 2009.

[41] T. Namazu, Y. Isono and T. Tanaka, "Evaluation of size effect on mechanical properties of single crystal silicon by nanoscale bending test using AFM," *J. Microelectromechanical Sys.*, vol. 9, no. 4, pp. 450-459, 2000.

[42] C. N. Arutt, W. Liao, H. Gong, P. D. Shuvra, J.-T. Lin, M. L. Alles, B. W. Alphenaar, J. L. Davidson, K. M. Walsh, S. McNamara, E. X. Zhang, A. L. Sternberg, D. M. Fleetwood, R. A. Reed and R. D. Schrimpf, "Dose-rate effects on the total-ionizing-dose response of piezoresistive micromachined cantilevers," *IEEE Trans. Nucl. Sci.*, vol. 65, no. 1, pp. 58-63, 2018.

[43] H. P. Hjalmarson, S. C. Witczak, M. R. Shaneyfelt, J. R. Schwank, A. H. Edwards, C. E. Hembree and T. R. Mattsson, "Mechanisms for radiation dose-rate sensitivity of bipolar transistors," *IEEE Trans. Nucl. Sci.*, vol. 50, no. 6, pp. 1901-1909, 2003.

[44] R. W. Keyes, "The effects of elastic deformation on the electrical conductivity of semiconductors," *Solid State Phys*, vol. 11, pp. 149-221, 1960.

[45] N. M. Johnson, C. Herring and D. J. Chadi, "Interstitial hydrogen and neutralization of shallow-donor impurities in single-crystal silicon," *Phys. Rev. Lett.*, vol. 56, no. 7, pp. 769-772, 1986.

[46] R. S. Muller, T. I. Kamins and M. Chan, Device electronics for integrated circuits, 3rd Ed., New York: Wiley, 2003.

[47] S. M. Sze and K. K. Ng, Physics of semiconductor devices, 3rd Ed., Hoboken, NJ: John Wiley & Sons, Inc, 2007.

[48] P. P. Debye and E. M. Conwell, "Electrical properties of n-type germanium," *Phys. Rev.*, vol. 93, no. 4, pp. 693-706, 1954.

[49] R. F. Pierret, Advanced semiconductor fundamentals, Upper Saddle River: Prentice Hall, 2003.

[50] N. D. Arora, J. R. Hauser and D. J. Roulston, "Electron and hole mobilities in silicon as a function of concentration and temperature," *IEEE Trans. Electron Devices*, vol. 29, no. 2, pp. 292-295, 1982.

[51] J. Bardeen and W. Shockley, "Deformation potentials and mobilities in non-polar crystals," *Phys. Rev.*, vol. 80, no. 1, pp. 72-80, 1950.

[52] C. Erginsoy, "Neutral Impurity Scattering in Semiconductors," *Phys. Rev.,* vol. 79, no. 6, pp. 1013-1014, 1950.

[53] N. Sclar, "Neutral Impurity Scattering in Semiconductors," *Phys. Rev.,* vol. 104, no. 6, pp. 1559-1561, 1956.

[54] P. Norton, T. Braggins and H. Levinstein, "Impurity and lattice scattering parameters as determined from hall and mobility analysis in n-type silicon," *Phys. Rev. B,* vol. 8, no. 12, pp. 5632-5653, 1973.

[55] S. S. Li and W. R. Thurber, "The dopant density and temperature dependence of electron mobility and resistivity in n-type silicon," *Solid-State Electron.,* vol. 20, no. 7, pp. 609-616, 1977.

[56] S. S. Li, "The dopant density and temperature dependence of hole mobility and resistivity in boron doped silicon," *Solid-State Electron.,* vol. 21, no. 9, pp. 1109-1117, 1978.

[57] C. Herring and E. Vogt, "Transport and deformation-potential theory for many-valley semiconductors with anisotropic scattering," *Phys. Rev.,* vol. 101, no. 3, pp. 513-552, 1956.

[58] Y. Kanda, "A graphical representation of the piezoresistance coefficients in silicon," *IEEE Trans. Electron Devices,* vol. 29, no. 1, pp. 64-70, 1982.

[59] M. Chu, Y. Sun, U. Aghoram and S. E. Thompson, "Strain: A solution for higher carrier mobility in nanoscale MOSFETs," *Annual Review of Materials Research,* vol. 39, no. 1, pp. 203-229, 2009.

[60] C. Herring, "Transport properties of a many-valley semiconductor," *Bell Syst. Tech. J.,* vol. 34, no. 2, pp. 237-290, 1955.

[61] R. W. Keyes, "Explaining strain: the positive and negative effects of elastic strain in n-silicon," *IEEE Circuits Devices Mag.,* vol. 18, no. 5, pp. 36-39, 2002.

[62] Y. Sun, S. E. Thompson and T. Nishida, "Physics of strain effects in semiconductors and metal-oxide-semiconductor field-effect transistors," *J. Appl. Phys.,* vol. 101, no. 10, p. 104503, 2007.

[63] J. C. Hensel and G. Feher, "Cyclotron resonance experiments in uniaxially stressed silicon: valence band inverse mass parameters and deformation potentials," *Phys. Rev.,* vol. 129, no. 3, pp. 1041-1062, 1963.

[64] H. Hasegawa, "Theory of cyclotron resonance in strained silicon crystals," *Phys. Rev.,* vol. 129, no. 3, pp. 1029-1040, 1963.

[65] R. W. Keyes, "The electronic contribution to the elastic properties of germanium," *IBM J. Res. Dev.,* vol. 5, no. 4, pp. 266-278, 1961.

[66] L. J. Sham, "A Calculation of Deformation Potentials in Silicon," *Proc. Phys. Soc.,* vol. 81, no. 5, p. 934, 1963.

[67] M. V. Fischetti and S. E. Laux, "Band structure, deformation potentials, and carrier mobility in strained Si, Ge, and SiGe alloys," *J. Appl. Phys.*, vol. 80, no. 4, pp. 2234-2252, 1996.

[68] J. Witzens, "Ab initio calculation of the deformation potential and photoelastic coefficients of silicon with a non-uniform finite-difference solver based on the local density approximation," *Comput. Phys. Commun.*, vol. 185, no. 8, pp. 2221-2231, 2014.

[69] W. Thomson, "XIX. On the electro-dynamic qualities of metals:-Effects of magnetization on the electric conductivity of nickel and of iron," *Proc. R. Soc. Lond.*, vol. 8, pp. 546-550, 1857.

[70] J. J. Hall, "Electronic effects in the elastic constants of *n*-type silicon," *Phys. Rev.*, vol. 161, no. 3, pp. 756-761, 1967.

[71] N. G. Einspruch and P. Csavinszky, "Electronic effect in the elastic constant C' of silicon," *Appl. Phys. Lett.*, vol. 2, no. 1, pp. 1-3, 1963.

[72] W. P. Mason and T. B. Bateman, "Ultrasonic attenuation and velocity changes in doped n-type germanium and p-type silicon and their use in determining an intrinsic electron and hole scattering time," *Phys. Rev. Lett.*, vol. 10, no. 5, pp. 151-154, 1963.

[73] C. K. Kim, M. Cardona and S. Rodriguez, "Effect of free carriers on the elastic constants of p-type silicon and germanium," *Phys. Rev. B*, vol. 13, no. 12, pp. 5429-5441, 1976.

[74] C. K. Kim, "Electronic effect on the elastic constant c_{44} of n-type silicon," *J. Appl. Phys.*, vol. 52, no. 5, pp. 3693-3695, 1981.

[75] P. Csavinszky, "Effect of holes on the elastic constant C′ of degenerate *p*-type Si," *J. Appl. Phys.*, vol. 36, no. 12, pp. 3723-3727, 1965.

[76] N. S. Averkiev, Y. V. Ilisavskiy and V. M. Sternin, "The free charge carrier effects on elastic properties of silicon," *Solid State Commun.*, vol. 52, no. 1, pp. 17-21, 1984.

[77] T. A. Fjeldly, F. Cerdeira and M. Cardona, "Effects of free carriers on zone-center vibrational modes in heavily doped p-type Si. I. acoustical modes," *Phys. Rev. B*, vol. 8, no. 10, pp. 4723-4733, 1973.

[78] N. M. Johnson, C. Doland, F. Ponce, J. Walker and G. Anderson, "Hydrogen in crystalline semiconductors: A review of experimental results," *Phys. B Condens. Matter*, vol. 170, no. 1, pp. 3-20, 1991.

[79] C. G. Van de Walle, P. J. H. Denteneer, Y. Bar-Yam and S. T. Pantelides, "Theory of hydrogen diffusion and reactions in crystalline silicon," *Phys. Rev. B*, vol. 39, no. 15, pp. 10791-10808, 1989.

[80] P. J. H. Denteneer, C. G. V. d. Walle and S. T. Pantelides, "Microscopic structure of the hydrogen-boron complex in crystalline silicon," *Phys. Rev. B*, vol. 39, no. 15, pp. 10809-10824, 1989.

[81] P. J. H. Denteneer, C. G. V. d. Walle and S. T. Pantelides, "Microscopic structure of the hydrogen-phosphorus complex in crystalline silicon," *Phys. Rev. B,* vol. 41, no. 6, pp. 3885-3888, 1990.

[82] S. J. Pearton, J. W. Corbett and J. T. Borenstein, "Hydrogen diffusion in crystalline semiconductors," *Phys. B Condens. Matter,* vol. 170, no. 1, pp. 85-97, 1991.

[83] J. I. Pankove, D. E. Carlson, J. E. Berkeyheiser and R. O. Wance, "Neutralization of shallow acceptor levels in silicon by atomic hydrogen," *Phys. Rev. Lett.,* vol. 51, no. 24, pp. 2224-2225, 1983.

[84] M. Stavola, S. J. Pearton, J. Lopata and W. C. Dautremont-Smith, "Vibrational spectroscopy of acceptor-hydrogen complexes in silicon: Evidence for low-frequency excitations," *Phys. Rev. B,* vol. 37, no. 14, pp. 8313-8318, 1988.

[85] L. Korpás, J. W. Corbett and S. K. Estreicher, "Multiple trapping of hydrogen at boron and phosphorus in silicon," *Phys. Rev. B,* vol. 46, no. 19, pp. 12365-12370, 1992.

[86] M. Capizzi and A. Mittiga, "Hydrogen in crystalline silicon: A deep donor?," *Appl. Phys. Lett.,* vol. 50, no. 14, pp. 918-920, 1987.

[87] H. P. Hjalmarson, R. L. Pease and R. A. B. Devine, "Calculations of radiation dose-rate sensitivity of bipolar transistors," *IEEE Trans. Nucl. Sci.,* vol. 55, no. 6, pp. 3009-3015, 2008.

[88] P. S. Winokur, K. G. Kerris and L. Harper, "Predicting CMOS inverter response in nuclear and space environments," *IEEE Trans. Nucl. Sci.,* vol. 30, no. 6, pp. 4326-4332, 1983.

[89] D. M. Fleetwood, P. S. Winokur and J. R. Schwank, "Using laboratory X-ray and cobalt-60 irradiations to predict CMOS device response in strategic and space environments," *IEEE Trans. Nucl. Sci.,* vol. 35, no. 6, pp. 1497-1505, 1988.

[90] M. R. Shaneyfelt, J. R. Schwank, S. C. Witczak, D. M. Fleetwood, R. L. Pease, P. S. Winokur, L. C. Riewe and G. L. Hash, "Thermal-stress effects and enhanced low dose rate sensitivity in linear bipolar ICs," *IEEE Trans. Nucl. Sci.,* vol. 47, no. 6, pp. 2539-2545, 2000.

[91] S. C. Witczak, R. C. Lacoe, D. C. Mayer, D. M. Fleetwood, R. D. Schrimpf and K. F. Galloway, "Space charge limited degradation of bipolar oxides at low electric fields," *IEEE Trans. Nucl. Sci.,* vol. 45, no. 6, pp. 2339-2351, 1998.

[92] R. L. Pease, R. D. Schrimpf and D. M. Fleetwood, "ELDRS in bipolar linear circuits: a review," *IEEE Trans. Nucl. Sci.,* vol. 56, no. 4, pp. 1894-1908, 2009.

[93] S. T. Pantelides, "Effect of hydrogen on shallow dopants in crystalline silicon," *Appl. Phys. Lett.,* vol. 50, no. 15, pp. 995-997, 1987.

[94] D. Yong-Chang, Z. Yu-Feng, Q. Guo-Gang and W. Shi-Fu, "Localized vibrational mode infrared absorption of BH pair in silicon," *Solid State Commun.,* vol. 55, no. 6, pp. 501-503, 1985.

[95] N. M. Johnson, F. A. Ponce, R. A. Street and R. J. Nemanich, "Defects in single-crystal silicon induced by hydrogenation," *Phys. Rev. B,* vol. 35, no. 8, pp. 4166-4169, 1987.

[96] J. Zhu, N. M. Johnson and C. Herring, "Negative-charge state of hydrogen in silicon," *Phys. Rev. B,* vol. 41, no. 17, pp. 12354-12357, 1990.

[97] C. Herring, N. M. Johnson and C. G. V. d. Walle, "Energy levels of interstitial hydrogen in silicon," *Phys. Rev. B,* vol. 64, no. 12, p. 125209, 2001.

[98] L. Tsetseris, R. D. Schrimpf, D. M. Fleetwood, R. L. Pease and S. T. Pantelides, "Common origin for enhanced low-dose-rate sensitivity and bias temperature instability under negative bias," *IEEE Trans. Nucl. Sci,* vol. 52, no. 6, pp. 2265-2271, 2005.

[99] N. M. Johnson and C. Herring, "Hydrogen immobilization in silicon p-n junctions," *Phys. Rev. B,* vol. 38, no. 2, pp. 1581-1584, 1988.

[100] S. J. Pearton, J. W. Corbett and T. S. Shi, "Hydrogen in crystalline semiconductors," *Appl. Phys. A,* vol. 43, no. 3, pp. 153-195, 1987.

[101] A. J. Tavendale, D. Alexiev and A. A. Williams, "Field drift of the hydrogen-related; acceptor-neutralizing defect in diodes from hydrogenated silicon," *Appl. Phys. Lett.,* vol. 47, no. 3, pp. 316-318, 1985.

[102] C. Sah, J. Y. Sun and J. J. Tzou, "Deactivation of the boron acceptor in silicon by hydrogen," *Appl. Phys. Lett.,* vol. 43, no. 2, pp. 204-206, 1983.

[103] J. I. Pankove, R. O. Wance and J. E. Berkeyheiser, "Neutralization of acceptors in silicon by atomic hydrogen," *Appl. Phys. Lett.,* vol. 45, no. 10, pp. 1100-1102, 1984.

[104] N. M. Johnson, "Mechanism for hydrogen compensation of shallow-acceptor impurities in single-crystal silicon," *Phys. Rev. B,* vol. 31, no. 8, pp. 5525-5528, 1985.

[105] N. V. Shlopak, Y. A. Bumai and A. G. Ulyashin, "Hydrogen passivation of γ-induced radiation defects in n-type Si epilayers," *Phys. Status Solidi A,* vol. 137, no. 1, pp. 165-171, 1993.

[106] N. V. Shlopak, A. G. Ulyashin and Y. A. Bumai, "Hydrogen effects on the electrical properties of electron-irradiated n-type Si epilayers," *Nucl. Instrum. Methods Phys. Res. Sect. B Beam Interact. Mater. At.,* vol. 86, no. 3, pp. 298-302, 1994.

[107] Q. Guogang and H. Zonglu, "The convergent effect of the annealing temperatures of electron irradiated defects in FZ silicon grown in hydrogen," *Solid State Commun.,* vol. 53, no. 11, pp. 975-978, 1985.

[108] T. Zundel and J. Weber, "Dissociation energies of shallow-acceptor-hydrogen pairs in silicon," *Phys. Rev. B,* vol. 39, no. 18, pp. 13549-13552, 1989.

[109] N. M. Johnson, C. Herring and D. J. Chadi, "Johnson, Herring, and Chadi reply," *Phys. Rev. Lett.,* vol. 59, no. 18, p. 2116, 1987.

[110] K. Bergman, M. Stavola, S. J. Pearton and J. Lopata, "Donor-hydrogen complexes in passivated silicon," *Phys. Rev. B,* vol. 37, no. 5, pp. 2770-2773, 1989.

[111] L. Tsetseris, X. J. Zhou, D. M. Fleetwood, R. D. Schrimpf and S. T. Pantelides, "Physical mechanisms of negative-bias temperature instability," *Appl. Phys. Lett.,* vol. 86, no. 14, p. 142103, 2005.

[112] J. H. Stathis, "Dissociation kinetics of hydrogen-passivated (100) Si/SiO_2 interface defects," *J. Appl. Phys.,* vol. 77, no. 12, pp. 6205-6207, 1995.

[113] J. T. Borenstein, J. W. Corbett and S. J. Pearton, "Kinetic model for hydrogen reactions in boron-doped silicon," *J. Appl. Phys.,* vol. 73, no. 6, pp. 2751-2754, 1993.

[114] J. I. Pankove, P. J. Zanzucchi, C. W. Magee and G. Lucovsky, "Hydrogen localization near boron in silicon," *Appl. Phys. Lett.,* vol. 46, no. 4, pp. 421-423, 1985.

[115] M. Stutzmann, "Hydrogen passivation of boron acceptors in silicon: Raman studies," *Phys. Rev. B,* vol. 35, no. 11, pp. 5921-5924, 1987.

[116] M. Nastasi, T. Höchbauer, J.-K. Lee, A. Misra, J. P. Hirth, M. Ridgway and T. Lafford, "Nucleation and growth of platelets in hydrogen-ion-implanted silicon," *Appl. Phys. Lett.,* vol. 86, no. 15, p. 154102, 2005.

[117] S. Reboh, F. Rieutord, L. Vignoud, F. Mazen, N. Cherkashin, M. Zussy, D. Landru and C. Deguet, "Effect of H-implantation in the local elastic properties of silicon crystals," *Appl. Phys. Lett.,* vol. 103, no. 18, p. 181911, 2013.

[118] C. A. Schuh, "Nanoindentation studies of materials," *Materials Today,* vol. 9, no. 5, pp. 32-40, 2006.

[119] D. Gu, H. Baumgart, K. K. Bourdelle, G. K. Celler and A. A. Elmustafa, "Nanomechanical response of the Si lattice to hydrogen implantation and annealing for layer splitting," *Jpn. J. Appl. Phys.,* vol. 48, no. 1, p. 101202, 2009.

[120] E. V. Jelenković, S. To, L. V. Goncharova and S. F. Wong, "Nanoindentation of silicon implanted with hydrogen: effect of implantation dose on silicon's mechanical properties and nanoindentation-induced phase transformation," *Mater. Res. Express,* vol. 4, no. 7, p. 075013, 2017.

[121] H. Izumi, R. Mukaiyama, N. Shishido and S. Kamiya, "Effect of hydrogen on the mechanical properties of silicon crystal surface," *ASME. International Electronic Packaging Technical Conference and Exhibition,* p. V001T06A008, 2013.

[122] H. L. Hughes and R. R. Giroux, "Space radiation affects MOS FET's," *Electronics,* vol. 37, pp. 58-60, 1964.

[123] D. M. Fleetwood, "Total ionizing dose effects in MOS and low-dose-rate-sensitive linear-bipolar devices," *IEEE Trans. Nucl. Sci.,* vol. 60, no. 3, pp. 1706-1730, 2013.

[124] R. D. Evans, The Atomic Nucleus, New York: McGraw-Hill, 1955.

[125] J.-T. Lin, P. D. Shuvra, W. Liao, S. McNamara, K. M. Walsh, C. N. Arutt, H. Gong, J. L. Davidson, M. L. Alles and B. W. Alphenaar, "Surface carrier concentration effect on elastic modulus of piezoelectric MEMS silicon cantilevers," *2017 19th International Conference on Solid-State Sensors, Actuators and Microsystems (TRANSDUCERS),* pp. 1175-1178, 2017.

[126] Z. Marka, S. K. Singh, W. Wang, S. C. Lee, J. Kavich, B. Glebov, S. N. Rashkeev, A. P. Karmarkar, R. C. Albridge, S. T. Pantelides, R. D. Schrimpf, D. M. Fleetwood and N. H. Tolk, "Characterization of X-ray radiation damage in Si/SiO_2 structures using second-harmonic generation," *IEEE Trans. Nucl. Sci.,* vol. 47, no. 6, pp. 2256-2261, 2000.

[127] D. M. Fleetwood, "Effects of hydrogen transport and reactions on microelectronics radiation response and reliability," *Microelectron. Reliab.,* vol. 42, no. 4-5, pp. 523-541, 2002.

[128] D. M. Fleetwood, M. J. Johnson, T. L. Meisenheimer, P. S. Winokur, W. L. Warren and S. C. Witczak, "1/*f* noise, hydrogen transport, and latent interface-trap buildup in irradiated MOS devices," *IEEE Trans. Nulc. Sci.,* vol. 44, no. 6, pp. 1810-1817, 1997.

[129] R. D. Schrimpf, "Recent advances in understanding total-dose effects in bipolar transistors," *IEEE Trans. Nucl. Sci,* vol. 43, no. 3, pp. 787-796, 1996.

[130] N. L. Rowsey, M. E. Law, R. D. Schrimpf, D. M. Fleetwood, B. R. Tuttle and S. T. Pantelides, "Mechanisms separating time-dependent and true dose-rate effects in irradiated bipolar oxides," *IEEE Trans. Nucl. Sci.,* vol. 59, no. 6, pp. 3069-3076, 2012.

[131] S. C. Witczak, P. S. Winokur, R. C. Lacoe and D. C. Mayer, "Charge separation technique for metal-oxide-silicon capacitors in the presence of hydrogen deactivated dopants," *J. Appl. Phys.,* vol. 87, no. 11, pp. 8206-8208, 2000.

[132] E. W. Enlow, R. L. Pease, W. Combs, R. D. Schrimpf and R. N. Nowlin, "Response of advanced bipolar processes to ionizing radiation," *IEEE Trans. Nucl. Sci.,* vol. 38, no. 6, pp. 1342-1351, 1991.

[133] D. M. Fleetwood, S. L. Kosier, R. N. Nowlin, R. D. Schrimpf, R. A. Reber, M. DeLaus, P. S. Winokur, A. Wei, W. E. Combs and R. L. Pease, "Physical mechanisms contributing to enhanced bipolar gain degradation at low dose rates," *IEEE Trans. Nucl. Sci.,* vol. 41, no. 6, pp. 1871-1883, 1994.

[134] R. L. Pease, P. C. Adell, B. G. Rax, X. J. Chen, H. J. Barnaby, K. E. Holbert and H. P. Hjalmarson, "The effects of hydrogen on the enhanced low dose rate sensitivity (ELDRS) of bipolar linear circuits," *IEEE Trans. Nucl. Sci.,* vol. 55, no. 6, pp. 3169-3173, 2008.

[135] D. M. Fleetwood, R. D. Schrimpf, S. T. Pantelides, R. L. Pease and G. W. Dunham, "Electron capture, hydrogen release, and enhanced gain degradation in linear bipolar devices," *IEEE Trans. Nucl. Sci.,* vol. 55, no. 6, pp. 2986-2991, 2008.

[136] D. R. Hughart, R. D. Schrimpf, D. M. Fleetwood, N. L. Rowsey, M. E. Law, B. R. Tuttle and S. T. Pantelides, "The effects of proton-defect interactions on radiation-induced interface-trap formation and annealing," *IEEE Trans. Nucl. Sci,* vol. 59, no. 6, pp. 3087-3092, 2012.

[137] S. C. Witczak, R. C. Lacoe, M. R. Shaneyfelt, D. C. Mayer, J. R. Schwank and P. S. Winokur, "Implications of radiation-induced dopant deactivation for npn bipolar junction transistors," *IEEE Trans. Nucl. Sci.,* vol. 47, no. 6, pp. 2281-2288, 2000.

[138] M. Caussanel, A. Canals, S. K. Dixit, M. J. Beck, A. D. Touboul, R. D. Schrimpf, D. M. Fleetwood and S. T. Pantelides, "Doping-type dependence of damage in silicon diodes exposed to X-ray, proton, and He+ irradiations," *IEEE Trans. Nucl. Sci.,* vol. 54, no. 6, pp. 1925-1930, 2007.

[139] A. J. Tavendale, A. A. Williams and S. J. Pearton, "Hydrogen injection and neutralization of boron acceptors in silicon boiled in water," *Applied Physics Letters,* vol. 48, no. 9, pp. 590-592, 1986.

[140] Y. Tokuda, T. Murase, T. Namizaki, T. Hasegawa and H. Shiraki, "Hydrogen introduction into p+ silicon by boiling in water and its application to deep-level transient spectroscopy measurements," *Materials Science and Engineering: B,* Vols. 91-91, pp. 152-155, 2002.

[141] M. Ogawa, S. Kamiya, H. Izumi and Y. Tokuda, "Effect of hydrogen at room temperature on electronic and mechanical properties of dislocations in silicon," *Materials Letters,* vol. 120, pp. 236-238, 2014.

[142] D. Mathiot, "Modeling of hydrogen diffusion in n- and p-type silicon," *Phys. Rev. B,* vol. 40, no. 8, pp. 5867-5870, 1989.

[143] H. P. Lang, F. M. Battiston, M. K. Baller, R. Berger, J.-P. Ramseyer, P. Fornaro, E. Meyer, H.-J. Güntherodt, C. Andreoli, J. Brugger, M. Despont, P. Vettiger, J.-H. Fabian, T. Mezzacasa, L. Scandella, C. Gerber and J. K. Gimzewski, "An electronic nose based on a micromechanical cantilever array," in *Micro Total Analysis Systems '98*, Springer, Dordrecht, 1998.

[144] T. H. Rogers, "High-intensity radiation from beryllium-window X-ray tubes," *Radiology,* vol. 48, no. 6, pp. 594-603, 1947.

[145] B. L. Henke, E. M. Gullikson and J. C. Davis, "X-ray interactions: photoabsorption; scattering, transmission, and reflection at E = 50-30,000 eV, Z = 1-92," *At. Data Nucl. Data Tables*, vol. 54, no. 2, pp. 181-342, 1993.